

**Development and assessment of drug-eluting and
anisotropic silk fibroin scaffolds for applications in
peripheral nerve regeneration**

A thesis
submitted
by
Alexander R. Nectow

In partial fulfillment of the requirements
for the degree of

Master of Science
In
Biomedical Engineering

TUFTS UNIVERSITY
May 2011
© 2011, Alexander R. Nectow
Advisor: David Kaplan

Copyright Notice

Abstract

Currently, there is no satisfactory treatment for peripheral nerve injury. Despite the plethora of research conducted in this field, there is still no clinically available nerve guidance conduit, which has surpassed the efficacy of the field's gold standard, the autologous nerve graft. The autologous nerve graft, however, is plagued with a variety of clinical complications, such as donor site morbidity, limited availability, nerve site mismatch, and the formation of neuromas. Thus, the development of a nerve guidance conduit (NGC), which could match the effectiveness of the autologous nerve graft, would be beneficial to the field of peripheral nerve surgery. Design strategies have recently included the development of biopolymers and synthetic polymers as primary scaffolds with tailored mechanical and physical properties, luminal "fillers" such as laminin and fibronectin as secondary internal scaffolds, surface micropatterning, and controlled release of neurotrophic factors. Peripheral nerve regeneration is a complex process. Recent research has suggested that a combination of the above strategies will yield successful treatments for peripheral nerve injury.

To encourage directional neurite outgrowth *in vitro*, anisotropic silk fibroin films of varying dimensions were created and screened for optimized alignment, using the P19 cell line. After determining the optimal micropattern dimensions, the silk fibroin films were then seeded with neuronally differentiated PC-12 cells and assessed for cellular alignment in an automated process.

Cellular alignment is traditionally assessed using manually drawn vectors connecting the neurite's end to the source on the soma. We wanted to develop an automated process, which would assess the orientation of the neuron soma, which has eccentricity in the direction of neurite outgrowth. In order to objectively assess PC-12 cellular alignment on the silk films, the Gauss-Newton algorithm was used to solve a nonlinear least squares problem, which approximates the neuron's soma and the proximal portions of the neurites as an ellipse. We found that this algorithm could accurately assess cellular alignment in the earlier stages of differentiation for the PC-12 cell line.

After developing anisotropic films for nerve regeneration applications, we were interested in controlled drug release for optimized peripheral nerve response. *In vitro* bioassays investigated the efficacy of different release profiles of glial cell line-derived neurotrophic factor (GDNF). We found that this neurotrophic factor can have long-term, controlled release profiles and that the neurotrophic factors retain their bioactivity throughout this process.

The goal of peripheral nerve repair is to promote the robust regenerative response of the proximal nerve cable, so that it may eventually grow through its distal end, and recover functionality through synapsing with its original output. Nerve regeneration is a complex process that requires the presence of numerous factors, signaling cues, and design parameters to be successful. The above developments are a step forward in the development of a comprehensive nerve guidance conduit, which could provide an alternative solution to the autologous nerve graft.

Acknowledgments

I would like to thank all of the people who have helped me with the research and thesis writing process. The following work would not have been possible without the help of so many different people.

First, I'd like to thank Professors David Kaplan and Misha Kilmer for their energy, enthusiasm, and patience with my work. I came to the Kaplan lab as a young, immature 18-year-old student, and through this experience, I was molded into a researcher. I cannot thank David enough for his lengthy, early morning discussions with me on my crazy ideas, as well as helping me stay grounded and focused on the science at hand. Additionally, I have to thank Misha for exposing me to applied mathematics, and spending countless hours with me explaining concepts in numerical analysis and linear algebra. Her encouragement, along with that of Professor Christoph Borgers, has inspired me to continue working at the interface of biology and applied mathematics for my PhD.

I have also been able to work with some incredible colleagues during my time at Tufts. To name a few, my work would not have been possible without the help of Mike Lovett, Eleanor Pritchard, and Nik Kojic. Their collaborations, mentorship, and friendship have been invaluable to me during my training. I would also like to thank Balaji Karthick and Jason Bressner for their imaging help, Brian Lawrence, Eun Seok Gil, and Biman Mandal for their generous help with silk biomaterials, and my undergraduate student Justin Pick for his laboratory assistance. I would also like to thank the rest of the Kaplan Lab group for their input at group meetings and informal conversations, as well as Milva Ricci, who patiently placed all of my last minute orders and was always around for great conversation and encouragement. I would like to offer special thanks to my roommate of 4 years, Jonathan Miller, for enduring my craziness and entertaining late night conversations on the struggles and philosophy of science. I would also like to thank my extended family and friends for their kindness, patience, and encouragement throughout this work.

Finally, and most importantly, I would like to thank my Mom, Dad, brother, Grammy, and Gramps for their endless love, encouragement, and support. Without them, this work would not have been possible.

Table of Contents

Development and assessment of drug-eluting and anisotropic silk fibroin scaffolds for applications in peripheral nerve regeneration	i
Copyright Notice	ii
Abstract	iii
Acknowledgments	iv
Table of Contents	v
List of Tables	viii
List of Figures	viii
Introduction	1
Background	1
Peripheral Nervous System	1
Peripheral Nerve Injury and Regeneration	1
Clinical Treatments	3
Developing Conduits	4
Autologous Tissues	5
Biopolymers	5
Synthetic Polymers	6
Growth and Guidance Cues	7
Neurotrophic Factors	7
Protein Cues	9
Anisotropy	9
Surface Chemistry/Morphology	10
Cues from Developmental Biology-Growth Cone Chemotaxis	10
Silk Biomaterials	11
Neuronal Cell Models	12
Iterative Algorithms	12
Unconstrained Optimization	13
Nonlinear Least-Squares	13
Elliptical Approximation of Cells and Cellular Structures	13
Gauss-Newton Method	14
Fourier Analysis	14
Discrete Fourier Transform	14
Normalized Cumulative Periodogram	15
Research Objectives	16
Materials and Methods	17
Cell Culture	17
P19 Cells	17
PC-12 Cells	17
Silk Biomaterials	18
Preparation of silk fibroin solution	18
Preparation of laminin-coated silk film arrays	18
Preparation of porous silk films	20
Quantification of Cellular Alignment	20
Manual quantification of P19 cell alignment and neurite outgrowth	20

Automated quantification of PC-12 cell alignment.....	21
Quantification of Cellular Metabolism and Proliferation.....	29
DNA quantification.....	29
Metabolic assay.....	29
Imaging.....	29
Flat and micropatterned silk films.....	29
P19 cell imaging.....	29
PC-12 cell imaging.....	30
Live calcium imaging.....	30
Controlled Drug Release.....	31
Microsphere and film fabrication.....	31
Growth factor release studies.....	32
Growth factor bioactivity assay.....	33
Statistics.....	33
Cellular adhesion studies.....	33
Normalized cumulative periodogram.....	33
Results.....	34
Neuronal Interactions with Silk Fibroin Films.....	34
Silk fibroin films for the alignment of P19 neurons.....	34
Adhesion and proliferation on laminin-functionalized silk films.....	35
Adhesion and proliferation after systemic delivery of NGF.....	36
Bradykinin-induced Ca ²⁺ fluxes in PC-12 neuronal cultures.....	37
Controlled Drug Release.....	39
Silk fibroin films for the controlled release of neurotrophic factors.....	39
Post-release GDNF bioactivity.....	40
Automated Assessment of Cellular Alignment.....	42
Cellular image processing.....	43
Scaffold image processing.....	45
Angle outputs.....	47
Normalized cumulative periodogram.....	48
Algorithm accuracy.....	50
Discussion.....	51
Future Directions.....	54
Optimizing Neurotrophic Factor Combinations for Nerve Repair.....	54
Automated Image Processing of Aligned Neurons.....	54
PC-12 Excitability on Patterned Silk Scaffolds.....	55
<i>In Vivo</i> Studies for Evaluating Silk Nerve Guidance Conduits.....	55
Conclusions.....	56
Appendix.....	57
Nerve Cell Alignment Algorithms.....	57
Manual Nerve Cell Alignment Code.....	57
Starting Image Guess.....	58
Gauss-Newton Algorithm.....	59
Cellular Alignment Algorithm with User Display.....	60
Scaffold Alignment Code.....	62
Automated Scaffold Alignment Code.....	63

Materials Processing.....	68
Preparation of porous silk nerve guides.....	68
Bibliography	69

List of Tables

Table 1. Clinically evaluated treatments for PNS injury.....	4
Table 2. Critically-sized defects in different species.....	6
Table 3. Some neurotrophic factors used in PNS regeneration.....	8
Table 4. Neural responses to different neurotrophic factors (Adapted from Schmidt and Leach, 2003).	9
Table 5. Dimensions of silk films from Figure 4.....	20

List of Figures

Figure 1. Peripheral nerve undergoing injury and regeneration. A) Axotomy occurs. B) Chromatolysis in the cell body and Wallerian degeneration in the distal segment are observed. C) Regenerating axon extends into the distal injury site. D) Growth cones migrates along bands of Büngner to target innervation site (Lee and Wolfe, 2000; Adapted from Seckel, 1990).	2
Figure 2. Scanning electron micrographs of some clinically approved conduits. A) NeuraGen (Type I Collagen). B) Neurolac (PLCL). C) Neurotube (PGA). (Schlosshauer <i>et al.</i> , 2006). Scale bar, 4 mm.	3
Figure 3. Scanning electron micrographs of silk fibroin tubes. A1) Methanol treated. A2) Air-dried. A3) Lyophilized. (Adapted from Lovett <i>et al.</i> , 2008).	12
Figure 4. Surface images (scanning electron micrographs) of 50 μm -thick flat and micropatterned silk fibroin films. A) Flat film. B) 600-17 film. C) 300-8 film. D) 300-17 film. Dimensions are patterns per millimeter-pitch angle. Scale bar, 2 μm	19
Figure 5. Manual assessment of nerve alignment. Schematic of a pseudobipolar P19 neuron aligned on a micropatterned silk film.	21
Figure 6. Image scaling process for neurons in MATLAB. A fluorescence image overlay containing an actin cytoskeleton stain and a nuclear counterstain was scaled according to fluorescence intensity.	22
Figure 7. Discretized image processing of neurons in MATLAB. Discretized subimage (left) from scaled neuron image (Fig. 5). An initial ellipse was selected around the neuron soma (right image, left inlay), which was used as the “ellipse starting guess.” Resultant ellipse (right image, right inlay) is the product of the Gauss-Newton iterations, which converged to a local minimum around the cellular structures.	23
Figure 8. Transmission and scaled images of micropatterned silk scaffolds (300-17 pattern) with aligned neurons. Transmission image intensities are converted to scaled values (see colorbar for quantified, relative image intensity values). Gratings (micropatterns) are spaced 3.33 μm peak-to-peak.	24
Figure 9. Discretized subimages, with manually determined vector, of micropatterned silk scaffolds (300-17) taken from transmission images from Figure 8.	25
Figure 10. The identity matrix and its discrete image output, a 512x512 pixel image with diagonal pixels (value 1) in red, and all other pixels (value 0) in blue. Inlay of image output shows enlarged pixels across the upper diagonal portion.	27
Figure 11. Computer-generated uniform random distribution (n=100). Histogram (10 bins) plotting frequency as a function of “angle” bins (left). Plot of uniform random	

distribution of “angles” (ordered lowest to highest), plotted as a function of index (right). Angle binning trends semi-linearly with the index in a uniformly distributed data set. ...	28
Figure 12. Fluo-4 dye molecular structure with and without acetoxymethyl ester group (AM, indicated as on of the R groups, bottom). Image taken from Gee <i>et al.</i> , 2000.	30
Figure 13. Silk fibroin films (light blue) bulk-loaded with GDNF (green).....	32
Figure 14. Silk fibroin films (light blue) embedded with GDNF microspheres (green). ...	32
Figure 15. Phase contrast micrographs of P19 neurons on flat and micropatterned silk films. Micrographs displaying cells on flat (a) and aligned 600-17 (b), 300-8 (c), and 300-17 (d) silk films. Scale Bar, 25 μm	34
Figure 16. P19 neuron alignment on micropatterned silk films. Histogram of neuron alignment on micropatterned films after 5 days in culture (n=6).	35
Figure 17. Nerve adhesion and proliferation profiles on laminin-adsorbed silk fibroin films. Nerve adhesion (a) and proliferation (b) assays (PicoGreen) were taken at 8 hours and 24 hours, respectively. Significance was found between all data points except for 5 μg and 10 μg laminin. * denotes significance at $p < 0.05$	36
Figure 18. Adhesion and proliferation profiles after systemic delivery of nerve growth factor (NGF) to silk and laminin-adsorbed surfaces. Adhesion (a) and proliferation (b) profiles after systemic NGF delivery, on a silk fibroin surface. At 24 hours (b), the statistical significance between 50 ng/mL and 100 ng/mL diminished. c) Adhesion (8 hours) and proliferation (24 hours) of P19 neurons on laminin-adsorbed silk films, after exposure to displayed concentrations of NGF. * denotes significance at $p < 0.05$	37
Figure 19. Live calcium imaging of PC-12 neurons on glass surfaces. Images reveal intracellular calcium fluxes before (a) and after (b) introduction of bradykinin to the culture. Arrows indicate cells that were selected for analysis of calcium spiking dynamics. Scale bar, 50 μm	38
Figure 20. Intracellular PC-12 calcium dynamics in response to the bradykinin receptor family agonist, bradykinin. Individual cells (left) reveal a heterogeneous (scaled) response of the PC-12 cells to bradykinin. Population response (right) shows a ~4.5 fold increase in intracellular calcium in response to bradykinin.....	39
Figure 21. Cumulative GDNF release profiles from different silk biomaterial modules over two weeks. a) Silk microspheres, alone, in solution. b) Microsphere-encapsulating silk films. c) Bulk-loaded silk films.	40
Figure 22. Bioactivity assay for PC-12 neurite outgrowth after neurotrophic factor delivery. a) Negative control (no neurotrophic factors). b) Positive control (50 ng/ml NGF). c) Experimental group, bulk-loaded glial cell line-derived neurotrophic factor (GDNF) eluting ~270 pg/day. Actin cytoskeletal stain (phalloidin) with nuclear counterstain (Hoechst 33342). Scale Bar, 50 μm	41
Figure 23. PC-12 neurite outgrowth quantified after neurotrophic factor delivery. $n \geq 200$ per treatment group.....	42
Figure 24. PC-12 neurons on micropatterned (a) and flat (b) silk films. Cells are stained with phalloidin (for actin cytoskeleton) and counterstained with Hoechst 33342 (for nucleus). Scale bar, 50 μm	43
Figure 25. Scaled images of PC-12 neurons on micropatterned silk films (from images in Figure 24a). Images were scaled from fluorescent micrographs and then discretized.	44
Figure 26. Scaled images of PC-12 neurons on flat silk films (from images in Figure 24b). Images were scaled from fluorescent micrographs and then discretized.	45

Figure 27. Scaffold image processing scheme. The original transmission image (top left) is converted into a binary, sorted image (1), analyzed for groove spacing (2), translated into a ~ 1 pixel-wide image (3), and fit with a linear least-squares regression to yield an angle output (4).....	46
Figure 28. PC-12 neuron alignment data on flat (a) and micropatterned (b) silk scaffolds. Histograms (top) display binning of cells in angles ranging from 0-90 degrees. Angle distributions (bottom) reveal trends in the data, which contain underlying probability distributions. Bottom data is further analyzed using the normalized cumulative periodogram (NCP).	48
Figure 29. Normalized cumulative periodogram (NCP) of neuron soma angle distributions on micropatterned silk films. Uniform distribution threshold is observed at NCP #22.....	49

Introduction

Background

Peripheral Nervous System

The functional unit of the nervous system is the neuron, a class of excitable cells capable of conducting electrical signals throughout the body. Neurons communicate with one another at the synapse via chemical messengers referred to as neurotransmitters. The synapse is the meeting site of an axon terminal (from the cell referred to as the presynaptic neuron) and the dendrites (processes from the postsynaptic neuron). After receiving chemical input, neurons initiate and propagate action potentials, carrying out their signals to the target input/output (Purves, 2007).

The nervous system is conventionally divided into two classes: the central nervous system (CNS), which is composed of the brain and spinal cord, and the peripheral nervous system (PNS), which consists of all other nerves including the cranial nerves. The peripheral nervous system is responsible for communication between the external environment and the CNS. Thus, the two major functions of the PNS are sensory perception through afferent neurons and motor output through efferent neurons.

To ensure conduction of rapid and reliable signals, the peripheral nervous system is myelinated. Myelin, which consists of lipids and proteins, serves as a dielectric (insulator) for the axons of peripheral nerves. Myelin allows for saltatory conduction, where action potentials jump between the Nodes of Ranvier (where the potentials are regenerated) (Stanfield, 2005). The cells responsible for myelination are a subtype of glial cells in the PNS referred to as Schwann cells. Schwann cells play an essential role in the regeneration of injured peripheral nerves, which will be discussed in the upcoming sections.

Peripheral Nerve Injury and Regeneration

Approximately 2.8% of trauma patients have some form peripheral nerve injury (Noble *et al.*, 1998). According to Seddon's scale, peripheral nerve injury is classified into three categories: a) neurapraxia, where there is some local myelin damage, b) axonotmesis, where there is some loss of axon continuity, and c) neurotmesis, where the nerve trunk is completely disrupted (severed) (Lee and Wolfe, 2000). The greatest focus of research is on neurotmesis, as it is the most severe, complicated form of peripheral nerve injury. After neurotmesis occurs, a series of complex events are initiated.

Immediately after injury, the cell undergoes a depolarizing event and traumatic degeneration occurs up to the next proximal Node of Ranvier (or further, depending on the extent of the injury). Within the next six hours, the proximal portion of the cell (containing the soma) undergoes chromatolysis where the Nissl bodies, rough endoplasmic reticulum, disperse and the nucleus migrates to the cell's periphery. This process initiates the cell's regenerative program, where instead of producing

neurotransmitters and signaling proteins, the cell begins to assemble structural proteins for axonal growth and repair (Burnett and Zager, 2004).

While the proximal segment of the nerve is undergoing its injury response program, the distal segment initiates a process called Wallerian degeneration within the next 24 to 36 hours. Wallerian degeneration is the process of distal axonal degeneration, leading to the breakdown of the blood-nerve barrier and the shedding of the Schwann cells' myelin sheath (Coleman and Freeman, 2010). At this point, the Schwann cells rapidly proliferate and begin to clear myelin and cellular debris by phagocytosing their own myelin and passing other myelin off to the macrophages, which have infiltrated the injury site through weakened a weakened endothelium (Vargas and Barres, 2007). After myelin clearance, the cells can begin to properly regenerate their axons through the distal injury site.

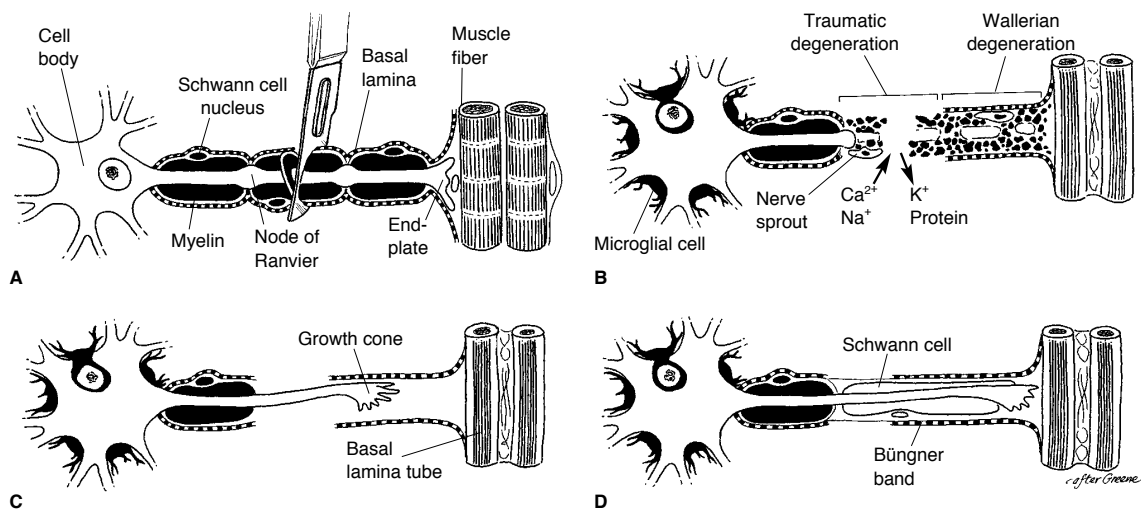


Figure 1. Peripheral nerve undergoing injury and regeneration. A) Axotomy occurs. B) Chromatolysis in the cell body and Wallerian degeneration in the distal segment are observed. C) Regenerating axon extends into the distal injury site. D) Growth cones migrates along bands of Büngner to target innervation site (Lee and Wolfe, 2000; Adapted from Seckel, 1990).

After clearance of myelin and axonal debris, a decellularized basal lamina remains, along which regenerating axons migrate and proliferating Schwann cells secrete growth/guidance cues and form bands of Büngner (Figure 1). At the same time, the neuron soma is rapidly synthesizing proteins necessary for regeneration, such as the growth-associated proteins (GAPs). GAP-43, an essential growth cone membrane component usually upregulated during development, is increased 20 to 100 times normal during the regenerative process (Seckel, 1990). Regenerating axons use growth cones to explore the injury environment and are guided along the basal lamina. Surviving neurons can then migrate to their proper target innervation site, proceeding at a growth rate of approximately 1 mm per day (Sunderland, 1947; Walsh and Midha, 2009).

Clinical Treatments

The current standard of care for nerve transection is the autologous nerve graft. However, autografts are associated with various complications including neuroma, donor site morbidity, nerve site mismatch, and limited amounts of donor tissue (Johnson and Soucacos, 2008). Recently, nerve guidance conduits (NGCs) have emerged as an effective alternative, though for gaps greater than 3-5 cm the nerve autograft is still much more effective. The first generation of artificial nerve conduits used in the clinic were non-resorbable silicone tubes, which were plagued by compression syndromes and often required secondary surgeries for removal (Lundborg *et al.*, 1982). Since then, there have been a variety of different biomaterials approved for clinical use, such as Type I collagen, polyglycolic acid (PGA), poly-DL-lactide-caprolactone, and polyvinyl alcohol (PVA). There currently are five FDA-approved nerve conduits (*Table 1*), four of which—Neurotube (PGA), Neurolac (poly-DL-lactide-caprolactone), NeuraGen (Type I collagen), and NeuroMatrixNeuroflex (Type I collagen) are bio-resorbable (with degradation rates on the order of 3 months to 4 years), and one that is non-resorbable—SaluBridge (PVA hydrogel) (Schlosshauer *et al.*, 2006).

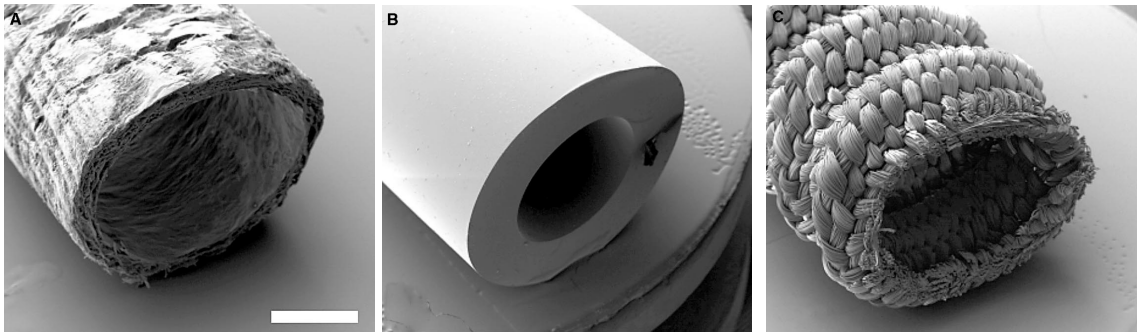


Figure 2. Scanning electron micrographs of some clinically approved conduits. A) NeuraGen (Type I Collagen). B) Neurolac (PLCL). C) Neurotube (PGA). (Schlosshauer *et al.*, 2006). Scale bar, 4 mm.

None of the above approved conduits (Figure 2) nor any currently in clinical use have incorporated adhesive extracellular matrix (ECM) protein or neurotrophic factors. Additionally, the degradation profiles of these conduits cannot be tailored to the regeneration rate of different peripheral nerves. Furthermore, swelling and biocompatibility issues have plagued the clinically available conduits. It appears that the most successful material implanted in humans, however, has been polyglycolic acid (PGA, the synthetic polymer used in Neurotube). A compilation of nine studies ranging from 1990 to 2005 has yielded positive results every time (75% of patients presented with ‘good’ or ‘very good’ recovery) (Schlosshauer *et al.*, 2006). Of the clinically available materials, PGA has the most rapid degradation rate (on the order of 3 months for Neurotube). The current generation of conduits provides mainly physical guidance cues via conduit morphology to help direct damaged nerve to its target sensory and motor outputs. The next generation of clinically used artificial conduits should be able to incorporate the use of neurotrophic factors, ECM proteins, surface micropatterning, and favorable physical and mechanical properties.

Table 1. Clinically evaluated treatments for PNS injury.

<u>Materials</u>	<u>Fabrication Methods</u>	<u>Nerve</u>	<u>Defect Size (in mm)</u>	<u>Outcomes</u>	<u>References</u>
Autologous Tissues					
Muscle	Vein filled with muscle grafts	Varied	5-60	85% of patients with 'good' recovery or better*	Battiston <i>et al.</i> , 2000; Battiston <i>et al.</i> , 2000
Nerve	Autologous graft	Varied	Varied	Gold Standard	Lee and Wolfe, 2000; Lundborg, 1999
Vein	Autologous graft	Nonessential Sensory	≤ 30	Good results; all patients considered surgery 'helpful'	Chiu and Strauch, 1990
	Autologous graft	Sensory	10-30	91% of patients with 'good' recovery or better*	Risitano <i>et al.</i> , 2002
Biomaterials					
Type I Collagen (NeuraGen)	Collagen Conduit	Digital	10-20	88% of patients with 'good' recovery or better*	Bushnell <i>et al.</i> , 2008
Synthetic Materials					
Poly(glycolic acid) (Neurotube)	PGA conduit	Digital	Up to > 8	> 74% of patients with 'good' recovery or better*	Weber <i>et al.</i> , 2000
	PGA conduit	Digital	≤ 40	> 89% of patients with 'good' recovery or better*	Battiston <i>et al.</i> , 2005
Poly-D,L-lactide-caprolactone (Neurolac)	PLCL conduit	Hand nerves	≤ 20	Sensory outcomes not significantly different from autograft	Bertleff <i>et al.</i> , 2005

Developing Conduits

A wide variety of biomaterials are being used to promote functional recovery of injured nerves. While autologous nerve grafts remain the gold standard, many material options are emerging. From biopolymers and synthetic polymers to blends, there are numerous options to capitalize on different properties of each material, such as mechanical strength, biocompatibility, degradation profile, and the ability to encapsulate different growth

factors and proteins. The following section offers a selection of those materials currently available and being used for *in vivo* studies, which have clinical potential.

Autologous Tissues

The autologous nerve graft remains the gold standard in the field of peripheral nerve surgery. This is mostly a product of its structural and biological composition, which is closely matched to the nerve being repaired (Jiang *et al.*, 2010). In the past due to lack of availability of autologous nervous tissue surgeons have relied on other tissues. A common biological matrix used has been the vein autograft, which has yielded mixed results (Battiston *et al.*, 2000; Kelleher *et al.*, 2001; Risitano *et al.*, 2002; Stahl and Goldberg, 1999). The autogenous vein grafts are equally as effective as NGCs for nerve defects ≤ 3 cm, when applied to nonessential sensory nerves; however, the use of the graft for defects >3 cm has yielded poor outcomes (Chiu and Strauch, 1990). Additionally, the vein constructs lack the physical robustness required for excellent clinical outcomes, as they are known to kink and collapse on themselves (Wolford and Stevao, 2003).

An alternative solution proposed to maintain the structural integrity of the vein graft and to provide a basement membrane for axonal outgrowth is to introduce a muscle graft-filler. Early studies have shown that both the presence and alignment of the muscle basal lamina have a significant impact on peripheral nerve repair (Glasby *et al.*, 1986; Ide, 1984). The muscle grafts most likely serve two positive roles in peripheral nerve repair: 1) the anisotropic distribution of muscle fibers, coaxially aligned with the regenerating nerve, allowing for proper target innervation, and 2) the basement membrane of the muscle tissue offers adhesive, extracellular matrix proteins for the regenerating axons. A recent clinical investigation evaluating the impact of muscle-filled vein grafts with respect to nerve defects on the order of 0.5-6 cm yielded positive results in 85% of cases (Battiston *et al.*, 2000); however, the majority of these positive results came from sensory nerves with defects of 2 cm or less. The treatments for mixed nerves (containing both efferent and afferent projections) yielded a lower proportion of “good” and “very good” outcomes (“very good” being the best possible outcome) as compared to the sensory nerve group. Other findings in the literature (Battiston *et al.*, 2000; Tang *et al.*, 1995) have also reported that the best outcomes with venous and muscle-vein grafts are in the cases of shorter sensory nerve defects with mixed nerves yielding mixed results.

Biopolymers

Biopolymers are an excellent source of biocompatible polymers, which often have tailored mechanical properties and degradation profiles engineered to be complementary to those of the regenerating nerve. Additionally, they come with the potential to encapsulate and present growth factors and extracellular matrix (ECM) proteins to the proximal nerve cable. Some biopolymers, such as keratin have recurring integrin-binding domains (the RGD motif), which have yielded positive results in a short mouse defect model (Sierpinski *et al.*, 2008). As previously mentioned, there are currently two FDA-approved biopolymer conduits (composed of Type I collagen), and, hopefully, many of the following materials will add to clinical options in the coming years.

Recent studies have assessed nerve conduit efficacy in different models, with gaps generally spanning 4 mm up to 30⁺ mm. In intermediate gaps (~10-13 mm), fibrin and silk have been used with some degree of success. In one study using silk the physical and functional recovery was close to that of nerve autografts (Yang *et al.*, 2007). The fibrin study did not assess electrophysiological properties of the regenerated nerve, but successful outcomes were reported based on histology when compared to the gold standard. With respect to critically sized defects (Table 2), on the order of 20 mm in rodent and rabbit species, and ~30 mm in larger animals such as dogs, biopolymer conduits have required internal fillers composed of either growth factor gradients or aligned mats/filaments. In one study laminin-1 and NGF-coupled gradients in agarose were used and led to significant axonal regeneration through a 20 mm gap in rats (Dodla and Bellamkonda, 2008). Other studies, using chitosan and collagen (with internal aligned filaments), were able to bridge 30 mm gaps in dogs, with functional recovery and at least partial physical repair and continuity of the nerve cable (Wang *et al.*, 2005; Okamoto *et al.*, 2010).

Table 2. Critically-sized defects in different species.

Animal	Nerve	Defect Size	Reference
Human	Digital	3 cm	Mackinnon and Dellon, 1990
Monkey	Ulnar	3 cm	Dellon and Mackinnon, 1988; Mackinnon <i>et al.</i> , 1985
Rabbit	Peroneal	3 cm	Strauch <i>et al.</i> , 1996
Rat	Sciatic	1 cm	Lundborg <i>et al.</i> , 1982

Synthetic Polymers

Synthetic polymers, though often less biocompatible relative to biopolymers, can offer opportunities for tailored degradation, and control of mechanical strength, porosity, and microstructure properties. Common chemical modifications of these polymers include the addition of adhesive proteins and growth factors. One strategy is the controlled release of neurotrophic factors by embedding microspheres into the conduit wall. A study using a poly(caprolactone) conduits embedded glial cell line-derived neurotrophic factor (GDNF)-eluting microspheres (made of a PLGA/PLLA blend) in the conduit wall showed an increase in tissue regeneration over 6 weeks in a 15 mm rat defect (Kokai *et al.*, 2010; Kokai *et al.*, 2010). Physical modifications in conduits have also proven to be effective. One study using polylactide conduits with microgrooves found superior regeneration in a 10 mm rat defect. To direct and enhance neurite outgrowth, another strategy has been to take advantage of electrically conducting polymers. Polypyrrole has been evaluated in numerous *in vitro* models, and it has been shown to enhance neurite outgrowth significantly in the presence of electrical stimulation (Schmidt *et al.*, 1997). This method also offers possibilities for chemical modification. A newer method has

been established, allowing the chemical linkage of positive and negative guidance cues to the polymer surface for neurite outgrowth cues with a high degree of resolution (neurite location) (Song *et al.*, 2006).

Despite the many advantages of using synthetic materials, some of these materials can also elicit inflammatory responses. To reduce inflammatory responses, one strategy has been to combine or “blend” synthetic materials with other more biocompatible materials. A recent study used a chitosan-PLA blend taking advantage of the natural biocompatibility of chitosan and the mechanical properties of PLA (Xie *et al.*, 2008). A polyurethane-collagen bilayer was also used to present a soft inner substrate and a harder shell, which maintained the conduit’s structural integrity during regeneration; this design also enabled the diffusion of nutrients, while limiting fibrous tissue infiltration based on internal and external pore distribution. Asymmetric porosity is an excellent strategy for maximizing nutrient diffusion and minimizing scar tissue infiltration. This technique is most easily accomplished with synthetic materials, as demonstrated in numerous studies using a PLGA/poloxamer blend, which yielded internal nano-size pores and external micro-size pores. This conduit outperformed silicone and plain PLGA (Oh *et al.*, 2008).

Biomaterials that have exhibited positive qualities include such biopolymers as chitosan, and collagen, and synthetic polymers poly(caprolactone), polyglycolic acid (PGA), and polylactides (in blends). Collagen, PGA, and a specific polylactide/poly(caprolactone) blend (PLCL) are already clinically available as nerve guidance conduits. Chitosan is biocompatible and has been extensively studied *in vivo*, with different synthetic polymer blends, successfully bridging critical defects (Ding *et al.*, 2010; Jiao *et al.*, 2009). There exist numerous strategies for selection of materials to generate a successful nerve conduit. Primary conduit requirements are biocompatibility, biodegradability, and porosity. It is also common to maximize mechanical properties and surface chemistries for cellular adhesion, tailored degradation and directionality in neurite outgrowth. The next section will discuss how these parameters are generally selected and assess the contribution of each modification to the comprehensive nerve conduit.

Growth and Guidance Cues

Nerve conduits have performed inconsistently in bridging murine defects greater than 10 mm (Bellamkonda, 2006). An emerging concept is that of luminal fillers, which serve as secondary scaffolds within the nerve conduits. These internal scaffolds hypothetically allow for increased neurite and Schwann cell outgrowth/proliferation based on the proteins and growth factors that are presented within the conduit. Additionally, it is often advantageous to present these proteins in an anisotropic fashion, as this has proven effective in promoting growth cone chemotaxis. Significant conduit “cues” are neurotrophic factors, protein cues, and anisotropy.

Neurotrophic Factors

Controlled release of neurotrophic factors is a desirable property of a conduit. Neurotrophic factors offer outgrowth and survival cues to the nerve cable that are often essential for full regeneration of critical defects. For each type of nerve (whether motor or

sensory or both) and desired outcome (outgrowth and/or survival), there is a subset of neurotrophic factors recommended. Most *in vivo* models are currently concerned with mixed nerves, containing efferent and afferent neurons, such as the sciatic nerve. For peripheral nerve regeneration, the principal neurotrophic factors used are nerve growth factor (NGF), glial cell-line derived neurotrophic factor (GDNF), brain-derived neurotrophic factor (BDNF), neurotrophin-3,4/5 (NT-3,4/5), and ciliary neurotrophic factor (CNTF). An overview of the neurotrophic factors used in nerve repair, with their respective outcomes, is provided in Tables 3 and 4.

Future considerations for neurotrophic factors will include investigations into controlled release and perhaps gradient delivery. Numerous mechanisms are currently in use for the delivery of neurotrophic factors such as matrices, microspheres, and hydrogels. Different release mechanisms and profiles may have different effects *in vivo*.

Table 3. Some neurotrophic factors used in PNS regeneration.

Neurotrophic Factors	Receptor, Response
NGF – Nerve Growth Factor	TrkA/p75 , Receptors expressed in sympathetic/peripheral sensory neurons (Schwann cells upregulate NGF and p75 in response to PNS injury); Involved in survival signaling and neurite outgrowth (Sofroniew <i>et al.</i> , 2001)
GDNF – Glial cell line-Derived Neurotrophic Factor	GFRα/Ret , Receptors expressed in sensory/motor neurons, GDNF primarily produced by Schwann cells in development; Plays an important role in sensory regeneration (Airaksinen and Saarma, 2002)
BDNF – Brain-Derived Neurotrophic Factor	TrkB , BDNF mRNA upregulated in distal nerve stump after sciatic nerve transection (Chen <i>et al.</i> , 2007); Positive modulation of peripheral nerve myelination (Chan <i>et al.</i> , 2001)
NT-3 – Neurotrophin-3	TrkC , NT-3 mRNA downregulated in distal nerve stump after sciatic nerve transection (Chen <i>et al.</i> , 2007); Negative modulation of peripheral nerve myelination (Chan <i>et al.</i> , 2001)
NT-4/5 – Neurotrophin-4/5	TrkB , Plays a role in survival of adult sensory neurons (Stucky <i>et al.</i> , 2002)
CNTF – Ciliary Neurotrophic Factor	CNTFR , Present in peripheral nerves and myelinating Schwann cells; Promotes survival of motor neurons (Terenghi, 1999)

Table 4. Neural responses to different neurotrophic factors (Adapted from Schmidt and Leach, 2003).

Neural Response	Neurotrophic Factors Used
Motor neuron survival	BDNF, NT-3, NT-4/5, CNTF, GDNF
Motor neuron outgrowth	BDNF, NT-3, NT-4/5, CNTF, GDNF
Sensory neuron survival	NGF, NT-4/5, GDNF
Sensory neuron outgrowth	NGF, BDNF, NT-3
Spinal cord regeneration	NGF, NT-3, CNTF, FGFs
Peripheral nerve regeneration	NGF, NT-3, NT-4/5, CNTF, GDNF, FGFs
Sensory nerve growth across PNS-CNS transition zone	NGF, NT-3, GDNF, FGFs

Protein Cues

To cross critically sized defects, there may be a need for secondary scaffolds within the nerve guidance conduit. While nerve gaps can be physiologically repaired over short distances, via band of Büngner formation (fibrin/LN-1 cables with Schwann cells), larger defects eliminate this possibility (Bellamkonda, 2006). A soft interior scaffold can provide the matrix for growth of Schwann cells and regenerating neurons and aid in more rapid band formation. Secondary scaffolds have yielded some positive *in vivo* results. The use of keratin-based hydrogels yielded axon diameters and densities greater than nerve autografts (Apel *et al.*, 2008). Similarly successful conduits used fibrin, with neovascularization and early-stage formation of fibroblast- and macrophage- rich tissues four weeks post-implantation in a murine model (Nakayama *et al.*, 2007).

Despite the above findings, other studies found that only tandem gradients of laminin-1 (LN-1) and nerve growth factor (NGF) were able to promote axonal regeneration of a critically sized defect (20 mm) in a rodent model. Isotropic distributions of these proteins were actually insufficient for regeneration (Dodla and Bellamkonda, 2008). These results are not surprising as to bridge these critically sized defects, the regenerating cable needs a chemotactic signal to promote: a) cell survival via the presence of the ECM protein/growth factor, and b) directionality via the ECM protein/growth factor gradient. Eloquent *in vitro* experiments have shown that gradients of growth factors such as NGF and adhesive proteins such as laminin (IKVAV peptide) are effective modulators of growth cone chemotaxis (Cao and Shoichet, 2001; Adams *et al.*, 2005). The lack of these features in conduits could hinder neurite outgrowth *in vivo*. Over shorter defects in humans (≤ 3 cm in humans), chemotaxis from the distal nerve segment is most likely sufficient for recovery and guidance of the regenerating proximal segment; however, over longer distances, the lack of growth and chemotactic signals hinders the regenerative capacity of the nerve.

Anisotropy

Scaffold anisotropy is a powerful strategy to control neuritogenesis and cellular alignment (Hoffman-Kim *et al.*, 2010). Indeed, *in vitro* cellular alignment is an excellent precursor to *in vivo* alignment and regeneration (Kim *et al.*, 2008). Consequently, many

groups have devised strategies to achieve optimal cellular alignment, with techniques based primarily on micro- and nano- patterning and electrospinning. Numerous *in vitro* studies have successfully shown that topographical cues significantly influence neurite outgrowth/alignment, synaptic connections and cellular differentiation (Cecchini *et al.*, 2007; Wang *et al.*, 2009), though fewer studies have used this strategy *in vivo*. However, these studies have found positive results. Recent *in vivo* studies bridging critically sized rat defects (≥ 14 mm) have found significant regeneration in treatment groups using highly aligned poly-acrylonitrile-*co*-methylacrylate (PAN-MA) thin-films. Aligned films, alone within a conduit were sufficient in bridging these critical defects (Clements *et al.*, 2009; Kim *et al.*, 2008). Scaffold anisotropy has been an effective technique in promoting nerve repair, and it will hopefully be implemented concurrently with other effective neurotrophic signals to generate successful, holistic conduits.

Surface Chemistry/Morphology

Earlier studies investigating neurite outgrowth and adhesion involved micropatterned laminin- and fibronectin- coated substrata and their effect on sensory neurons from chick dorsal root ganglia (Gundersen, 1987). Laminin is a protein commonly used for surface modification for nerve regeneration due to its positive influence on neurite outgrowth and growth cone chemotaxis (Adams *et al.*, 2005; Yu and Shoichet, 2005). The role of laminin in neural development is understood. Neurite outgrowth has also been augmented through the use of electrically conducting polymers. In one study, coupling electrical stimulation to the electrically conducting polymer oxidized polypyrrole, neurite outgrowth response was significant, yielding neurites on average almost double in length (Schmidt *et al.*, 1997). Another investigation improved nerve and glial cell attachment and differentiation on positively charged hydrogels, in addition to augmented neurite outgrowth (Dadsetan *et al.*, 2009). Alterations in surface chemistry are an effective strategy in promoting neurite adhesion and outgrowth.

In addition to chemical modifications, physical alterations, such as morphology, have been investigated for their role in cellular adhesion and survival. Effective strategies to promote neurite outgrowth based on micro- and nano- patterning (discussed below) have been reported; however, surface roughness can have deleterious effects on neural cells. A recent study investigating nano-rough surfaces showed high sensitivity and apoptotic/necrotic response of neuronally-differentiated SH-SY5Y cells to gold surfaces (Brunetti *et al.*, 2010). Upon exposure to the rough surfaces, a loss of neuronal polarity was observed. These results suggest that surface roughness and micro- and nano-topography need to be evaluated for their physiological impact prior to use in regenerative applications.

Cues from Developmental Biology-Growth Cone Chemotaxis

There are multiple methods to guide axons through complex environments. To initiate robust growth cone chemotaxis, permissive substrates (such as laminin) are commonly used (Dodd and Jessell, 1988). Additionally, guidance by contact inhibition is a prevalent mechanism of inhibiting neurite outgrowth, and thus regeneration. Human neuroma expresses semaphorin 3A, which reduces neurite extension *in vitro* (Tannemaat *et al.*, 2007). Future directions in peripheral nerve regeneration may include inhibiting such a

class of molecules, in a similar fashion as is done with chondroitin sulfate proteoglycans (CSPGs) (Lee *et al.*, 2010).

Silk Biomaterials

Silk fibroin is a well-characterized protein derived from the *Bombyx mori* silkworm, known for its low immunogenicity, controllable degradation, and favorable mechanical properties (Pritchard *et al.*, 2011; Yang *et al.*, 2007). Silk is therefore well fit to serve as a biopolymer for nerve guidance conduits. Indeed, silk has already been evaluated in numerous *in vivo* studies investigating nerve regeneration (Ghaznavi *et al.*, 2011; Yang *et al.*, 2007). Additionally, silk scaffolds can offer tailored release profiles of encapsulated growth factors and can be surface-functionalized with coatings of various extracellular matrix (ECM) proteins, such as laminin and fibronectin. Further, the ability to micropattern and manipulate the surface morphology and surface chemistry of silk biomaterials provides a versatile protein substrate for nerve guidance studies. Recent studies with release of nerve growth factor (NGF) from silk matrices (Uebersax *et al.*, 2007) and *in vitro* nerve guidance using silk nanofibers demonstrate the utility of this polymeric protein biomaterial system for nerve-related studies.

After peripheral nerve injury, the presence of growth factors and adhesion molecules is required in order for a successful regenerative response to occur. A current obstacle at the interface of tissue engineering and controlled drug release is the need to elute multiple growth factors from the same biomaterial scaffold, with different release kinetics (Saltzman and Olbricht, 2002). Such systems would be beneficial for the field of neural tissue engineering, which requires the delivery of neurotrophic factors to the wound site, for positive, functional sensory and motor neuron recovery. Silk biomaterials offer a breadth of systems for the controlled delivery of bioactive molecules (Numata and Kaplan, 2010). Specifically, silk fibroin has been shown to offer the advantageous property of controlled drug release of many different molecules relevant to nervous system function, including NGF (Uebersax *et al.*, 2007), adenosine (Pritchard *et al.*, 2010), and GDNF (Madduri *et al.*, 2010). Silk can also be chemically modified on specific residues with known chemistries, altering hydrophilicity, cellular adhesion, and drug release profiles (Murphy and Kaplan, 2009). One study was able to chemically couple the adhesion ligand RGD (arginine-glycine-aspartic acid) (Sofia *et al.*, 2001).

As mentioned above, silk fibroin nerve conduits are already being used for *in vivo* studies, and their manufacturing parameters are currently being altered to optimize factors such as nutrient diffusion, minimal scar tissue infiltration, mechanical properties, and degradation rate. Nutrient diffusion, scar tissue infiltration, and mechanical property parameters can be altered by varying the conduit's porosity, through different processing methods such as methanol treatment, air-drying, lyophilizing, and poly(ethylene oxide) (PEO) addition/leeching (Figure 3) (Lovett *et al.*, 2007; Lovett *et al.*, 2008). Mechanical properties can be manipulated using other techniques, such as protease inhibitors (Pritchard *et al.*, 2011).

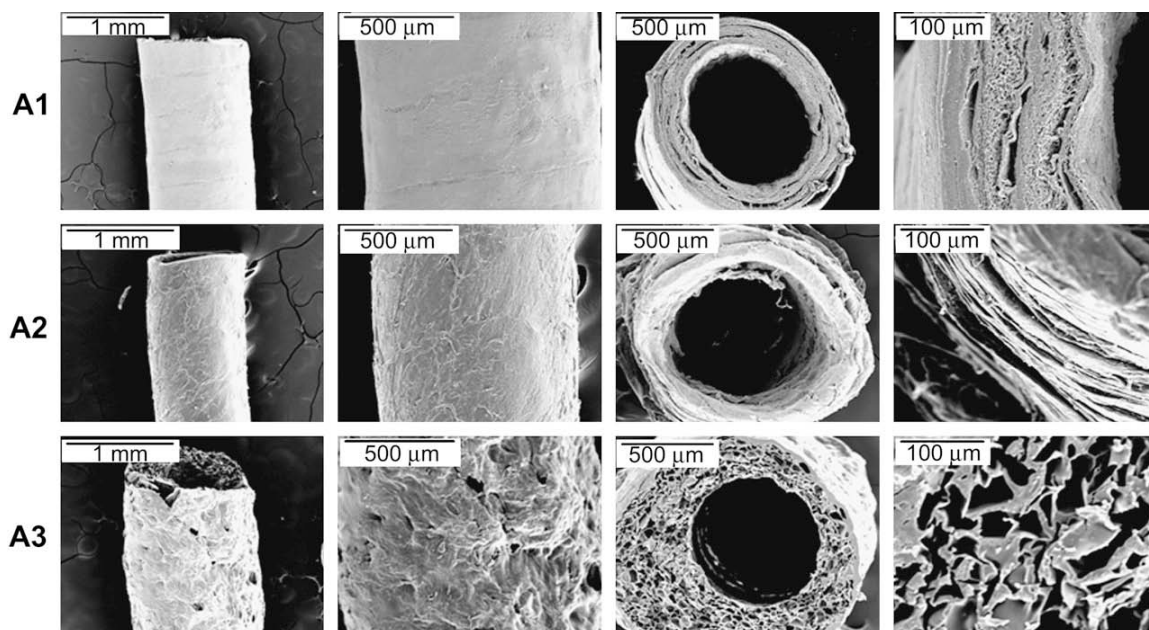


Figure 3. Scanning electron micrographs of silk fibroin tubes. A1) Methanol treated. A2) Air-dried. A3) Lyophilized. (Adapted from Lovett *et al.*, 2008).

Neuronal Cell Models

The current studies used the P19 and PC-12 cell lines. These cells, through simple protocols, can be differentiated into neuron-like cells. The PC-12 cell line was originally isolated from a rat pheochromocytoma and requires a simple NGF-dosing protocol to differentiate into neuron-like cells, expressing neurites and becoming electrically excitable (Greene and Tischler, 1976). The P19 cell line was originally isolated from a rat embryonal teratocarcinoma, and is differentiated into neuron-like cells expressing neurites using retinoic acid treatments (Jones-Villeneuve *et al.*, 1982). The P19 cell line was specifically chosen for studies investigating varying concentrations of NGF on cellular adhesion.

Iterative Algorithms

Image processing techniques in the field of neural tissue engineering are often limited to manual evaluation, by hand-drawn vectors designating neurite and cell body orientation. Thus, a more objective and automated method of data analysis is desirable. Iterative algorithms are concerned with approximating solutions for different classes of problems. The hope is that these algorithms, with sufficient numbers of iterations based on pre-determined termination criteria, will eventually converge on the approximate solutions.

Early in the maturing stages of differentiating neurons, the cell body and portions of the neurites can be approximated as an ellipse. To establish an automated algorithm, which converges an ellipse on the neuron (to approximately model the cell), techniques in unconstrained optimization are required, to solve the nonlinear least squares problem posed. The most appropriate technique to solve such a nonlinear least squares problem is

the Gauss-Newton algorithm. The Gauss-Newton method can efficiently and iteratively solve a nonlinear least squares problem by approximating it as a linear least squares problem. The hope is that the linear least squares solution converges to the same solution as the nonlinear problem.

Unconstrained Optimization

Unconstrained optimization is concerned with solving for the local minimum of a function $f(\mathbf{x})$, $\min_{\mathbf{x}} f(\mathbf{x})$. In order to find the minimizer, \mathbf{x}^* , we need to solve the problem (Frandsen *et al.*, 2004):

$$\mathbf{x}^* = \operatorname{argmin}_{\mathbf{x}} f(\mathbf{x})$$

Equation 1. Optimization problem.

where $f : \mathbb{R}^n \rightarrow \mathbb{R}$, and f is the cost function. We know that \mathbf{x}^* is a local minimizer for $f : \mathbb{R}^n \rightarrow \mathbb{R}$ if:

$$f(x^*) \leq f(x) \text{ for } \|x^* - x\| \leq \epsilon, \text{ for } \epsilon > 0$$

Equation 2. Definition of local minimizer.

Nonlinear Least-Squares

A specific case of unconstrained optimization is that of nonlinear least-squares, which concerns itself with solving problems of the following nature (Dennis and Schnabel, 1996):

Given $R : \mathbb{R}^n \rightarrow \mathbb{R}^m$, $m \geq n$,

Find $\mathbf{x}_* \in \mathbb{R}^n$ for which $\sum_{i=1}^m (r_i(x))^2$ is minimized, where $r_i(x)$ is the i^{th} component of the function R .

Elliptical Approximation of Cells and Cellular Structures

In order to assess cellular alignment and morphology in a semi-automated fashion, optimization algorithms are necessary. A common technique to accomplish this, in the specific case of cells (or sub-cellular structures) with polarized morphologies, has been that of elliptical approximation. This technique has been quite successful in analyzing the neurite outgrowth of dorsal root ganglia (DRG) explants (Haines and Goodhill, 2010) and the orientation of nuclei (Bray *et al.*, 2010). From the following equation, we can extrapolate numerous elliptical parameters to characterize the orientation and morphology of the structure being measured:

$$\frac{(x - x_c)^2}{a^2} + \frac{(y - y_c)^2}{b^2} = 1$$

Equation 3. Equation for an ellipse.

where (x_c, y_c) is the coordinate of the ellipse's centroid.

Using this technique, we can find the centroid, major and minor axes, eccentricity, and orientation. However, ellipse-fitting problems require solving a nonlinear least squares problem. A popular technique, adopted by the two groups above has used direct ellipse-specific fitting techniques (Fitzgibbon *et al.*, 1999). Other iterative techniques to solve this problem are available, such as the Gauss-Newton algorithm.

Gauss-Newton Method

The Gauss-Newton method solves a nonlinear least squares problem by approximating the second-order term (Hessian matrix), leaving a linear system to be solved for \mathbf{s}_k (Heath, 2002):

$$(\mathbf{J}^T(\mathbf{x}_k)\mathbf{J}(\mathbf{x}_k))\mathbf{s}_k = \mathbf{J}^T(\mathbf{x}_k)\mathbf{r}(\mathbf{x}_k)$$

Equation 4. Linear system for Gauss-Newton method.

This system can be reduced to the linear least squares problem $\mathbf{J}(\mathbf{x}_k)\mathbf{s}_k \approx \mathbf{r}(\mathbf{x}_k)$. After solving for \mathbf{s}_k , we can solve $\mathbf{x}_{k+1} = \mathbf{x}_k + \mathbf{s}_k$. The idea behind this algorithm is to take a nonlinear least squares problem, and replace it with a linear least squares problem that will converge to the same solution as the nonlinear problem. Thus, the algorithm is iterated through until the solution converges. When the Gauss-Newton algorithm cannot converge to the approximate solution, a more robust modification, which interpolates between the Gauss-Newton algorithm and the method of gradient descent, is referred to as the Levenberg-Marquardt algorithm. Though this algorithm is more robust, it is slower than the Gauss-Newton algorithm.

Fourier Analysis

Fourier analysis plays an important role in signal processing, allowing for the identification and understanding of specific signal components. When Fourier analysis is combined with different statistical tests, powerful observations can be made concerning the underlying probability distribution of the incoming signal. Thus, techniques in Fourier analysis can be useful to understand when a population of neurons aligns with an underlying anisotropic scaffold.

Discrete Fourier Transform

The discrete Fourier transform (DFT) can be expressed in terms of matrix multiplication. Given a one-dimensional signal $\mathbf{x} \in \mathbb{R}$, we have the discrete Fourier transform (Hansen *et al.*, 2006):

$$dft(\mathbf{x}) = F^H \mathbf{x}$$

Equation 5. Matrix multiplication form of the discrete Fourier transform.

The elements of the matrix F are given by $F_{jk} = N^{-1/2}e^{2\pi i(j-1)(k-1)/N}$, for $j, k = 1, \dots, N$ and $i = \sqrt{-1}$. In matrix form, F^H appears as:

$$F^H = 1/\sqrt{N} \begin{pmatrix} 1 & 1 & 1 & 1 & \dots & 1 \\ 1 & \omega & \omega^2 & \omega^3 & \dots & \omega^{N-1} \\ 1 & \omega^2 & \omega^4 & \omega^6 & \dots & \omega^{2(N-1)} \\ 1 & \omega^3 & \omega^6 & \omega^9 & \dots & \omega^{3(N-1)} \\ \vdots & \vdots & \vdots & \vdots & \ddots & \vdots \\ 1 & \omega^{N-1} & \omega^{2(N-1)} & \omega^{3(N-1)} & \dots & \omega^{(N-1)(N-1)} \end{pmatrix}$$

where $\omega = \exp(-2\pi i/N)$, which is a primitive Nth root of unity. When \mathbf{x} is real, $\text{dft}(\mathbf{x})$ has conjugate symmetry, so we can construct the matrix $\text{dft}(\mathbf{x})$ (without losing any information) such that,

$$\text{dft}(\mathbf{x})_{i+1} = \text{conj}(\text{dft}(\mathbf{x}_{n-i+1})), i = 1, \dots, q$$

Equation 6. Conjugate symmetry of DFT with real signal \mathbf{x} .

where $q = (N/2) + 1$.

Normalized Cumulative Periodogram

The power spectral density (PSD) of a signal helps identify its periodicities. For an n -length vector \mathbf{x} , its periodogram (power spectrum) is a q -length vector \mathbf{p} , with elements

$$\mathbf{p}_k = |\text{dft}(\mathbf{x})_k|^2$$

Equation 7. Elements of the periodogram.

for $k = 1, \dots, q$ (Hansen *et al.*, 2006). The normalized cumulative periodogram (NCP) is the $(q-1)$ -length vector $\mathbf{c}(\mathbf{x})$ with elements:

$$c(x)_k = \frac{\|p(2 : k + 1)\|_1}{\|p(2 : q)\|_1},$$

Equation 8. Elements of the normalized cumulative periodogram.

for $k = 1, \dots, q-1$. The normalized cumulative periodogram (NCP) is useful for determining when a signal strays away from the uniform distribution. This technique is important in understanding when a population of cells can no longer be considered “aligned.” Random signals (white noise) will trend semi-linearly along the periodogram. Statistical tests such as the Kolmogorov-Smirnov test can be used to set the limits within which the signal can vary (Hansen *et al.*, 2006).

Research Objectives

The aim of this research is to develop and analyze the efficacy of anisotropic silk fibroin films in aligning neurons *in vitro*. The ultimate goal of this research is the application of these silk films to *in vivo* use with nerve guidance conduits (NGCs), which will hopefully assist in regenerating transected peripheral nerve cables. The initial goal was to optimize neuronal adhesion on the silk films through surface modifications with laminin protein and RGD-peptide, and the systemic delivery of nerve growth factor (NGF). Once this was accomplished, the project focused on obtaining optimized cellular alignment on micropatterned silk films. Additional computational experiments were then performed to fully automate the process of objectively assessing cellular alignment *in vitro*.

This work may ultimately help to further understand the morphological changes that neurons undergo during cellular alignment. Additionally, the automation of assessing cellular alignment may serve as an *in vitro* ‘predictor’ assay for *in vivo* nerve regeneration.

Materials and Methods

Cell Culture

P19 Cells

Mouse embryonal teratocarcinoma P19 cells (ATCC, Manassas, VA) were cultured according to previously established protocols (Jones-Villeneuve *et al.*, 1982; Jones-Villeneuve *et al.*, 1983). Briefly, the P19 cells were cultured in α -Minimum Essential Medium (Invitrogen), supplemented with 0.1% penicillin-streptomycin (Invitrogen), 2.5% Fetal Bovine Serum (Invitrogen), and 7.5% bovine calf serum (Thermo Fisher Scientific). Cells were cultured at 37°C and 5% CO₂/95% air. Media was replenished every 3 days, and cells were passaged at 60-70% confluence using trypsin (0.25% with EDTA 4Na, Invitrogen). Cells were frozen using cryogenic medium (90% bovine calf serum, 10% DMSO).

The P19 cells were differentiated down a neuronal lineage over 5 days according to previously established protocols (Jones-Villeneuve *et al.*, 1982; Jones-Villeneuve *et al.*, 1983). Briefly, on day 1, $\sim 1 \times 10^6$ cells were manually dissociated with a flared-tip glass Pasteur pipette and plated onto low-adhesion bacteriological culture dishes, followed by exposure to 0.1 μ M retinoic acid (RA). Cells were grown in suspension and were collected for colonies on culture days 3 and 4. On days 3 and 4, the colonies were selected for by incubating the suspension cultures in centrifugation tubes, followed by collection of the colonies. After collecting the colonies, the cells were treated with trypsin to eliminate potential focal adhesion proteins, followed by repeated manual dissociation using a flared-tip Pasteur pipette. Then, retinoic acid (RA) was added to the cell cultures at a final concentration of 0.1 μ M. On day 4, the cells were plated onto their respective substrates, and on day 5 (one day post-plating) the cells were treated with 5 μ g/mL cytosine arabinoside (araC) to kill the remaining proliferative cell subpopulation, leaving a more homogeneous neuronal culture. P19 cells were used for studies investigating cellular adhesion and proliferation and alignment.

PC-12 Cells

An adhesive variant of the rat pheochromocytoma (PC-12) cell line was obtained (ATCC, Manassas, VA). The PC-12 cells were cultured in F-12K medium (ATCC), supplemented with 1% penicillin-streptomycin (Invitrogen), 2.5% fetal bovine serum (Invitrogen), and 15% horse serum (Invitrogen). Cells were cultured at 37°C and 5% CO₂/95% air. For optimized cellular adhesion in culture, Corning CellBIND T-75 flasks were used according to the manufacturer's protocol (Corning). Prior to plating, flasks were coated with a thin layer of growth medium, followed by a 30-minute incubation to increase cellular adhesion upon plating. Media was replenished every 2-3 days, and cells were passaged at 70-80% confluence using trypsin (0.25% with ethylenediaminetetraacetic acid (EDTA) 4Na) (Invitrogen) followed by gentle agitation to lift the remaining cells from the dishes. Cells were frozen down using cryogenic medium (complete PC-12 growth medium supplemented with 5% DMSO). To differentiate the PC-12 cells down a

neuronal lineage, the complete growth medium was supplemented with 50 ng/mL or 100 ng/mL natural mouse nerve growth factor (NGF 2.5S) and replenished every other day for the duration of the experiments (Invitrogen) (Greene and Tischler, 1976). The PC-12 cell line was used for studies investigating cellular alignment on micropatterned silk scaffolds.

Silk Biomaterials

Preparation of silk fibroin solution

An 8% (w/v) aqueous silk fibroin solution was prepared from the cocoons of the *B. mori* silkworm using our previous established protocols (Kim *et al.*, 2004; Li *et al.*, 2006). Briefly, cocoons were boiled for 30 minutes in a 0.02 M Na₂CO₃ solution to remove sericin, before being rinsed in a series of Milli-Q water washes. The silk was then dissolved in a 9.3 M LiBr solution over the course of 4 hours, and dialyzed against 1 L of Milli-Q over the course of 4 days to remove the remaining LiBr. For purity, the silk was centrifuged at 8,700 rpm for 20 minutes, at 5-10°C. To obtain a highly concentrated silk fibroin solution (~25-30% (w/v)), the 8% silk solution was concentrated against a 10% poly(ethylene glycol) (PEG) solution for 20-24 hours or a 15% PEG solution for ~14 hours. All silk solutions were kept at 4°C until their time of use.

Preparation of laminin-coated silk film arrays

Flat and micropatterned silk films for the alignment of the P19 cells were prepared according to our previously established protocols (Lawrence *et al.*, 2009). Briefly, PDMS-negative molds were obtained from positive diffraction gratings of varying dimensions: 600-17, 300-8, and 300-17 (Table 5, Edmund Optics, Barrington, NJ). An 8% silk solution was then cast onto each of these PDMS-negative molds and allowed to dry overnight. The films were then water-annealed for 7 hours to induce a transition from the amorphous aqueous phase to the silk β -form characterized by anti-parallel β -sheets (Jin and Kaplan, 2003). The films were sterilized with 3 alternating ethanol washes (20 minutes) and PBS washes, followed by 20 minutes of UV irradiation. All films were coated with natural mouse laminin by adsorption of a 25 μ g/mL laminin solution through incubation for 2 hours at 37°C, before being carefully rinsed 3 times with PBS. For the adhesion and proliferation studies, flat silk films were processed similarly to the patterned films, with the exception that they were prepared in 24-well plates. Briefly, the films were prepared by adding 200 μ L of a 6-8% (w/v) silk solution into 24-well plates. The plates were allowed to dry overnight, followed by water annealing and ethanol sterilization, as described above. Laminin-coated films were also processed as stated above.

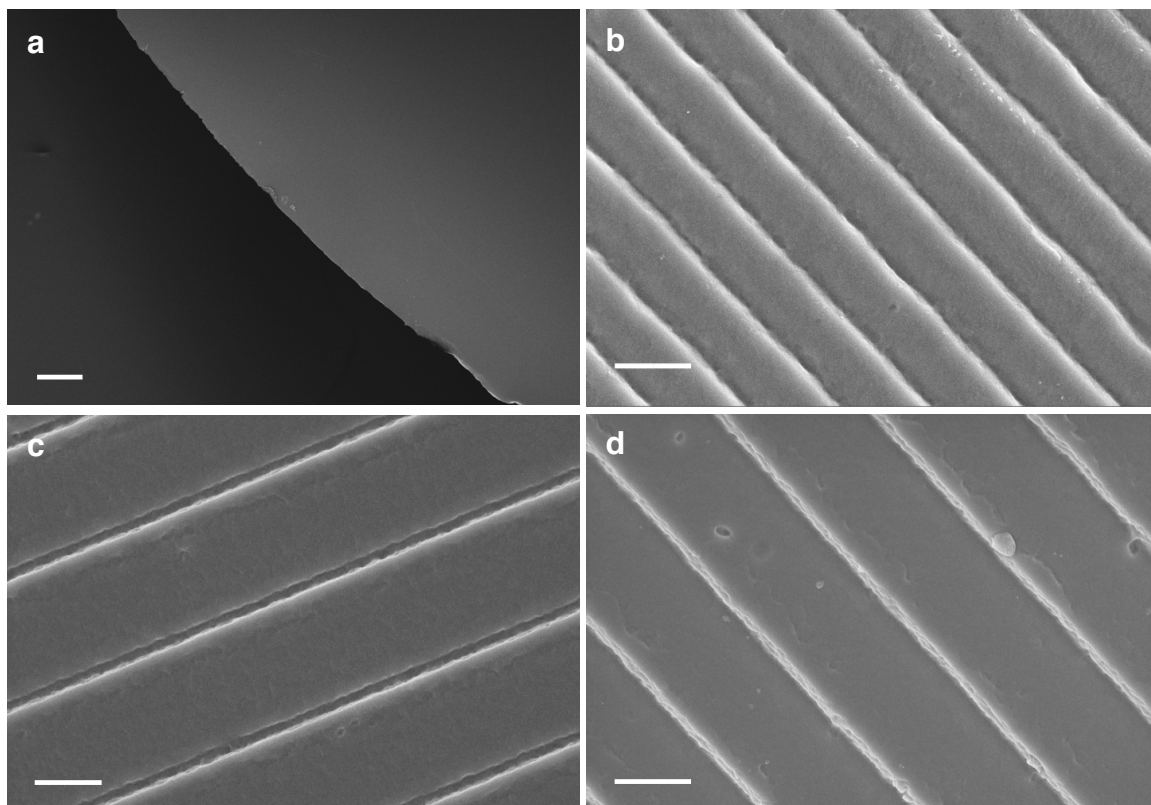


Figure 4. Surface images (scanning electron micrographs) of 50 μm -thick flat and micropatterned silk fibroin films. A) Flat film. B) 600-17 film. C) 300-8 film. D) 300-17 film. Dimensions are patterns per millimeter-pitch angle. Scale bar, 2 μm .

Dimension of the micropatterned silk films (Table 5) were collected from the manufacturer, and these measurements were confirmed through scanning electron microscopy (SEM) (Figure 4). Silk film thickness can be modified based on percent concentration of silk protein used in solution (Lawrence *et al.*, 2008).

Table 5. Dimensions of silk films from Figure 4.

	Pattern Spacing, Peak to Peak (μm)	Pitch Angle (Degrees)	Groove Depth (nm)	Film Thickness (μm)
Flat	N/A	N/A	N/A	~50
600-17	1.667	17	200	~50
300-8	3.333	8	200	~50
300-17	3.333	17	200	~50

Preparation of porous silk films

Flat and micropatterned porous silk films were prepared according to a previously established protocol (Lawrence *et al.*, 2008; Gil *et al.*, 2010). Briefly, 1% silk solutions with 0.035% (w/w) poly(ethylene oxide) (PEO, $M_w=900,00$; Sigma-Aldrich) were cast onto 25-mm x 25-mm square polydimethylsiloxane (PDMS) molds obtained from flat/diffraction gratings (500 nm depth, 300 grates per mm, 17° pitch) (Edmund Optics, Barrington, NJ), and allowed to dry overnight. The films were water annealed for 7 hours to induce a transition from the amorphous aqueous phase to the anti-parallel β -sheet or crystalline structure for stability in cell culture (Jin and Kaplan, 2003), before being placed into a water bath for 3 days to extract the PEO. All films were then coupled with integrin-binding ligand arginine-glycine-aspartic acid (RGD) following our previously established protocol (Sofia *et al.*, 2001) to promote increased cellular adhesion. Prior to cell plating, the films were sterilized with three alternating 30-minute ethanol and PBS washes, followed by 20 minutes of UV irradiation.

Quantification of Cellular Alignment

Manual quantification of P19 cell alignment and neurite outgrowth

A MATLAB program was developed to measure the pixel length of neurites and their angle off of the axis of alignment (code can be found in the Appendix section). For flat films, the axis was arbitrarily chosen to be the horizontal axis. This was done by generating an axis vector (**a**) and a neurite vector (**b**) (Fig. 5). Bold notation denotes a column vector. The angle of orientation (θ) was then obtained using the Law of cosines:

$$|\mathbf{a} \cdot \mathbf{b}| = |\mathbf{a}||\mathbf{b}|\cos(\theta)$$

Equation 9. Law of Cosines.

A trivial transformation of Equation 5 leads to the solution, θ :

$$\theta = \cos^{-1}\left(\frac{|\mathbf{a} \cdot \mathbf{b}|}{|\mathbf{a}||\mathbf{b}|}\right)$$

Equation 10. Law of Cosines transformed to solve for angle of alignment, θ .

The length of the neurites was calculated in pixels as $|\mathbf{b}|$ and then converted to μm using the image scale bar obtained from through using ImageJ software (NIH).

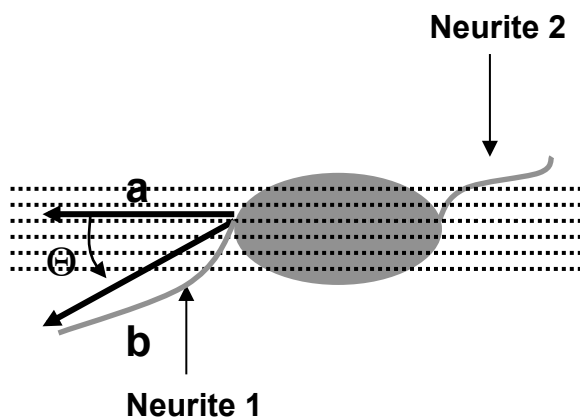


Figure 5. Manual assessment of nerve alignment. Schematic of a pseudobipolar P19 neuron aligned on a micropatterned silk film.

Automated quantification of PC-12 cell alignment

Image Thresholding

It was assumed that a typical, maturing (plated for ≤ 8 days) PC-12 neuron cell body resembles that of a narrow ellipse. Examples of typical cells on flat and micropatterned films are shown in the Results section, Figure 24. The images are close to being piecewise continuous; pixel values inside the cells are close to a single constant value, while pixel values outside the cells belong to the silk biomaterial scaffold, with a well defined gap between the two average values. In order to find a best fit ellipse to the cell body, each cell image was first converted into a piecewise constant image. A value of 1 was assigned to points estimated by the thresholding to be inside the cell, and a value of 0 was assigned to points outside the cell. Because some images contained pieces of other structures, a semi-automated process was used to isolate the cells prior to thresholding. This procedure had the added benefit of providing the starting guess parameters for the optimization algorithm.

GENERATION 1: The first generation algorithm required that the user use the mouse to indicate the center of the cell in question (with the image scaled), and to indicate two other points in the image to be used as the lengths of a major axis and minor axis of an ellipse that would be large enough to include the cell (Fig. 6). The algorithm then computed the mean value inside the region contained inside the ellipse starting guess. All pixel values greater than the mean were reassigned to have a value of 1, while all pixel values less than the mean (or outside the starting guess) were assigned a value of 0 (Fig. 6). Figure 7 illustrates an image after the thresholding process (the user-defined starting ellipse is shown in another shade for context.)

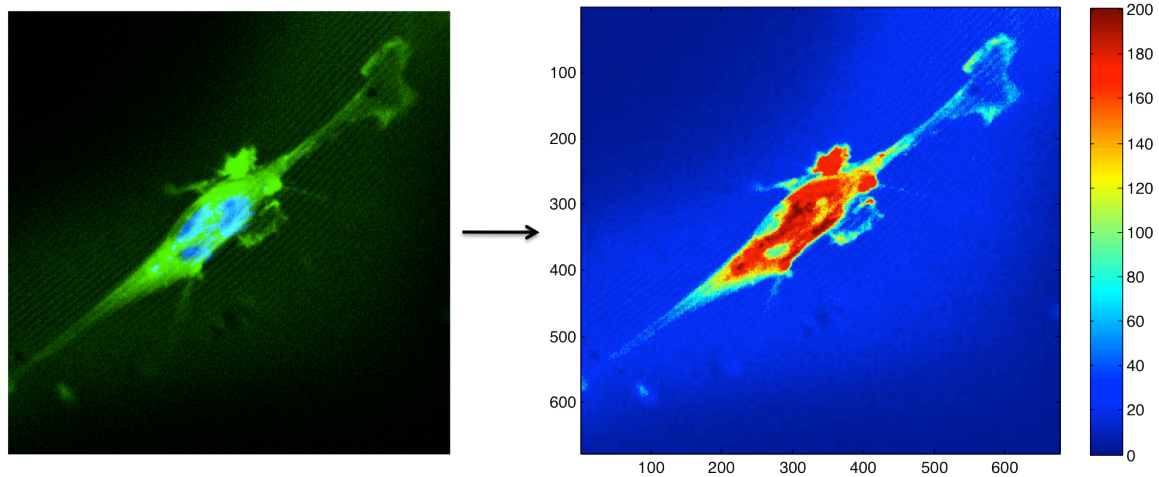


Figure 6. Image scaling process for neurons in MATLAB. A fluorescence image overlay containing an actin cytoskeleton stain and a nuclear counterstain was scaled according to fluorescence intensity.

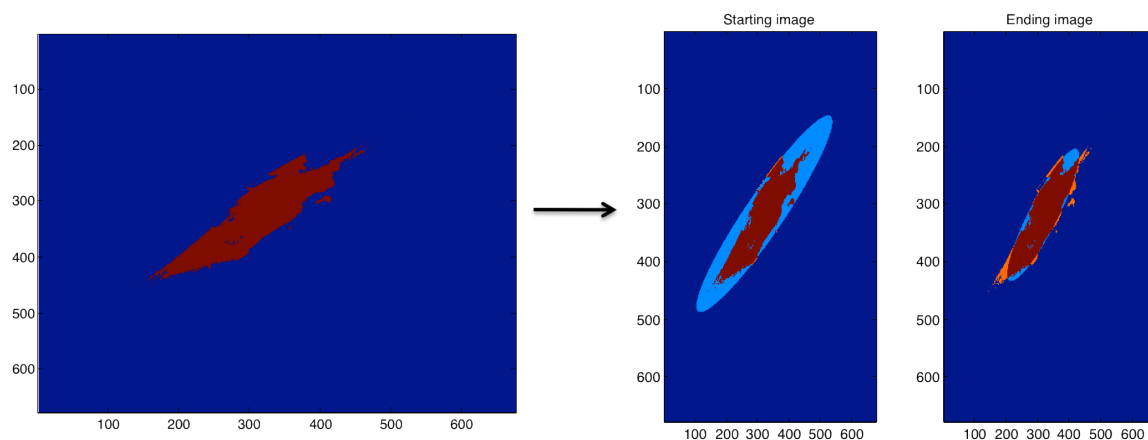


Figure 7. Discretized image processing of neurons in MATLAB. Discretized subimage (left) from scaled neuron image (Fig. 5). An initial ellipse was selected around the neuron soma (right image, left inlay), which was used as the “ellipse starting guess.” Resultant ellipse (right image, right inlay) is the product of the Gauss-Newton iterations, which converged to a local minimum around the cellular structures.

To properly match the cellular alignment data with scaffold orientation, primitive image thresholding was also necessary for the manual construction of “alignment” vectors along the gratings of the micropatterned silk films. First, transmission images were collected, in the same frame as the cells under observation (see Results, Figure 24). These images were then scaled in a similar fashion as the neurons in Figure 6, and discretized in the same fashion as Figure 7. This portion of the algorithm initially required manual input of the alignment vectors for the micropatterned films. The user was prompted to select two points in the direction parallel to the presented micropatterns. The output would be an angle relative to the horizon.

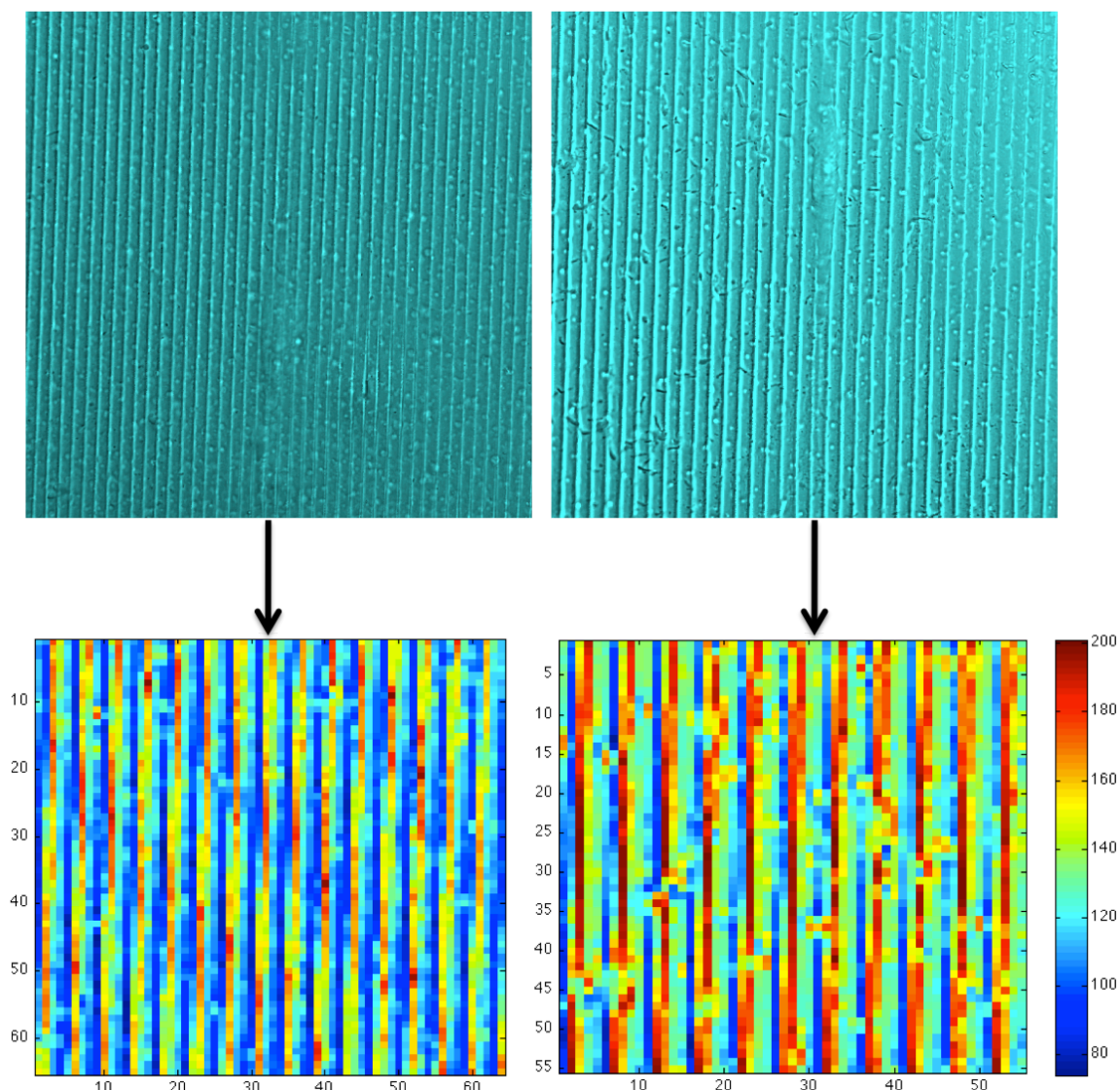


Figure 8. Transmission and scaled images of micropatterned silk scaffolds (300-17 pattern) with aligned neurons. Transmission image intensities are converted to scaled values (see colorbar for quantified, relative image intensity values). Gratings (micropatterns) are spaced $3.33 \mu\text{m}$ peak-to-peak.

From Figure 8, it is clear that there are micropatterns on the silk films, though isolating the parallel lines and obtaining their alignment is nontrivial. The first step in automating this process is discretizing the images, so that the parallel micropatterns are visible as pixels, with designation 1 (red). Valleys should therefore correspond to a pixel value of 0 (blue). The discretization of the image as seen in Figure 9 was possible as the peaks and valleys of the micropatterned silk scaffolds correspond to different transmission image intensities (based on scaffold depth).

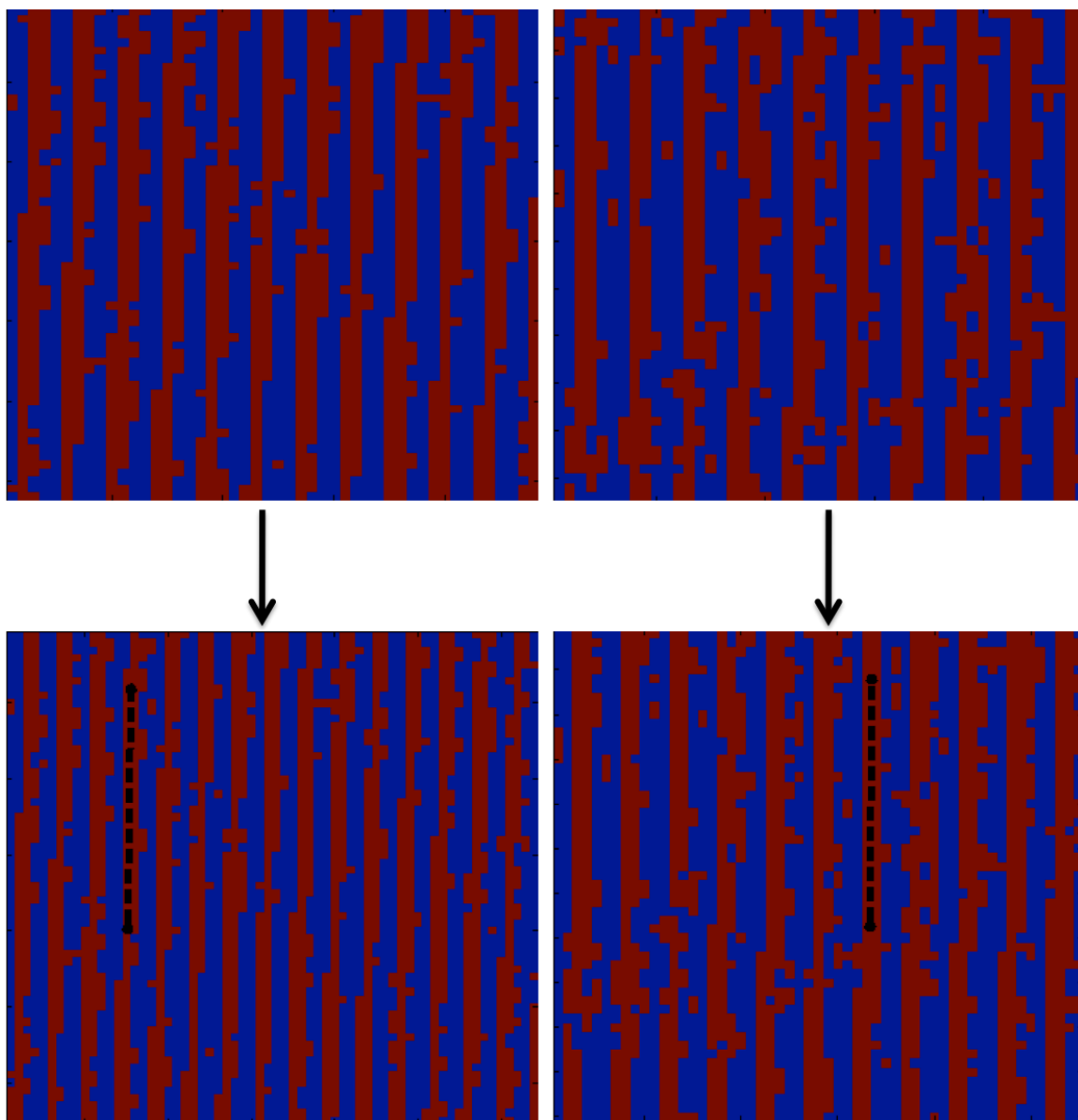


Figure 9. Discretized subimages, with manually determined vector, of micropatterned silk scaffolds (300-17) taken from transmission images from Figure 8.

Generation 2: The second-generation algorithm is completely automated, and it is described in detail below, in the “Quantification of Cellular Alignment” section.

Quantification of Cellular Alignment

The automated quantification of cellular alignment was constructed as three separate phases. In the first phase, a Gauss-Newton algorithm was used to find the five parameters describing the best-fit ellipse to the neuron soma (cell body). In phase two, a combination of a k-means clustering approach and a best fit line approach was used to determine, from the corresponding transmission image of the silk scaffold, the alignment angle of the scaffold relative to the horizon (x-axis). The resultant ellipse major axis is then compared

with the scaffold angle to determine the alignment of the cell to the scaffold. The final phase of the algorithm consists of choosing the degree threshold beyond which we classify the cells as not aligned with the scaffold. This is achieved through a nearness-to-uniformity measure by use of an NCP-criterion.

PHASE I: The $n \times n$ pixel space was mapped to $[0,1] \times [0,1]$ with spacing $1/(n-1)$. The optimization problem to be solved is

$$\min_{\mathbf{p}} \|\mathbf{h}(\mathbf{p}) - \mathbf{d}\|$$

Equation 11. Optimization problem for Gauss-Newton Algorithm.

where \mathbf{p} denotes the vector of length 5 containing σ_1 (length of major axis), σ_2 (length of minor axis), x_c (x-coordinate of the centroid), y_c (y-coordinate of the centroid), and θ (counterclockwise angle of the major axis relative to the x-axis). The vector \mathbf{d} is the vectorized, piecewise constant image described above. Thus, since the image is $n \times n$, \mathbf{d} is of length n^2 . The functional notation $\mathbf{h}(\mathbf{p})$ is used to represent a piecewise constant output image of an ellipse that results from the parameter values given in \mathbf{p} . The notation $\|\mathbf{v}\|$ means the Euclidean norm/length of a vector \mathbf{v} .

Since this is a non-linear least squares problem, we use a Gauss-Newton method to compute the solution to this optimization problem. Let \mathbf{p}_k denote the value of the parameters at iteration k , and let $\mathbf{r}_k = \mathbf{h}(\mathbf{p}_k) - \mathbf{d}$. Then the Gauss-Newton algorithm is (Heath, 2002):

For $i=1, \dots, \text{maximum iterations}$

- 1) Compute $\mathbf{h}(\mathbf{p}_k)$, \mathbf{r}_k , and \mathbf{J}_k (the Jacobian at iteration k)
- 2) Solve $(\mathbf{J}_k^T \mathbf{J}_k) \mathbf{s}_k = -\mathbf{J}_k^T \mathbf{r}_k$ for \mathbf{s}_k
- 3) $\mathbf{p}_{k+1} = \mathbf{p}_k + \mathbf{s}_k$
- 4) If $\frac{\|\mathbf{p}_{k+1} - \mathbf{p}_k\|}{\|\mathbf{p}_k\|} < \text{tol1}$, or $\|\mathbf{h}(\mathbf{p}_{k+1}) - \mathbf{d}\| < \text{tol2}$, stop

The Jacobian \mathbf{J}_k is an $n^2 \times 5$ matrix of partial derivative estimates computed using 1st order finite differences. Specifically, the (i,j) entry of \mathbf{J}_k is computed as

$$\frac{\mathbf{h}(\mathbf{p}_k) - \mathbf{h}(\mathbf{p}_k + \mathbf{e}_j)}{2\delta_j}$$

where δ_j denotes the spacing for the j th parameter, and \mathbf{e}_j is a vector of length 5 with all zeros except a δ_j in the j th position. We used $\delta_j, j=1, \dots, 4 = 10^{-4}$, and $\delta_5 = \pi/16$.

PHASE II: Once the best-fit ellipse was determined, it remains to compute the angle of alignment with respect to the scaffold beneath, which first means determining the angle of the scaffold relative to the x-axis.

Using confocal microscopy, two images were obtained simultaneously: a fluorescent cell image and a corresponding light microscopy, or transmission, image that reveals the pattern of the scaffold (see Results, Figure 27). It is clear to the naked eye that there are lines running through the transmission images that correspond to the periodic peaks and valleys in the folds of the silk, but it is not obvious how to automate the process of identifying the angles of these lines relative to the horizon.

Each cell's corresponding transmission image was used to determine the angle of the scaffold relative to the x-axis as follows. First, the image was passed through a k-means algorithm (Herrera, 2005; see Appendix) using 6 classes. The output is an image of 6 values, one value for each class. The pixels in the valleys get assigned to a class with the lowest pixel value. Thus, the k-means output image is taken and thresholded to obtain a binary image revealing only the valleys, which appear to the eye as a series of parallel lines (see Results, Figure 27).

Next it is necessary to isolate only one of these lines, so that we its angle with the x-axis can be computed. The pixels of intersection are found between the binary line image and an image containing a single line running from the upper left to lower right corner of the image (an identity matrix) (Fig. 10). Since the binary line image looks like a series of parallel lines, it is expected that the intersection image should consist of a roughly periodic sequence 1's and 0's running from the upper left to lower right. The difference between neighboring +1 pixels on this line is computed, and a search for the first pixel with a decent sized jump between it and its next +1 neighbors is performed. This process yields the corners of a box, or subimage, in which a single line (valley) can be isolated, followed by performing a least-squares best fit to the line (Heath, 2002). Finally, the angle between the best fit and the x-axis is computed. This angle is recorded as the alignment angle between the scaffold and x-axis.

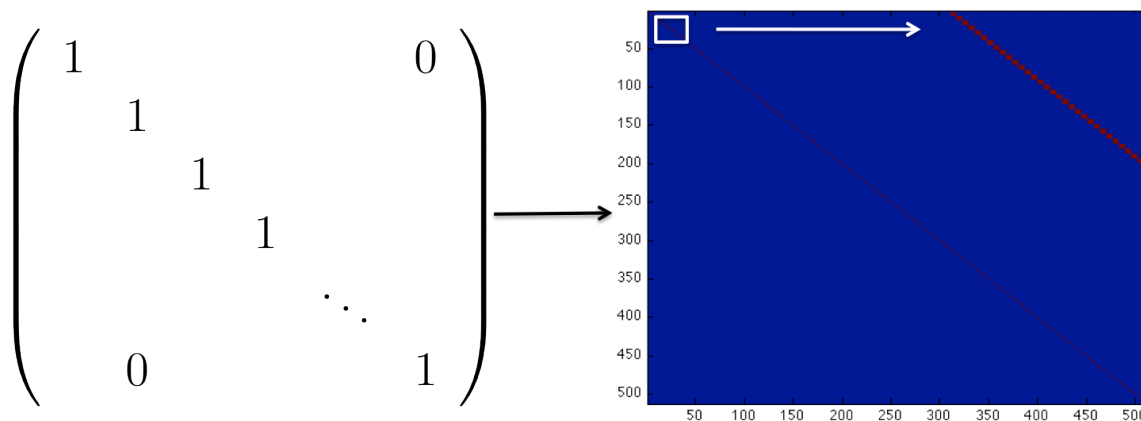


Figure 10. The identity matrix and its discrete image output, a 512x512 pixel image with diagonal pixels (value 1) in red, and all other pixels (value 0) in blue. Inlay of image output shows enlarged pixels across the upper diagonal portion.

PHASE III: It is hypothesized that the subset of cells that are truly aligned with the scaffold will display a uniform variation in their alignment angles, whereas the cells that

are not aligned are no longer uniformly distributed. The justification of this is two-fold. First, in the experiment, if cells are plated without scaffold, experiments performed have found the alignment angles to follow a uniform distribution. Second, the plot of alignment angles as measured in the first two phases of the algorithm is considered as a function of index of the example (Fig. 11). As the plot in Figure 11 illustrates, the uniform distribution yields a semi-linear regression, when increasing angles are plotted as neuronal index.

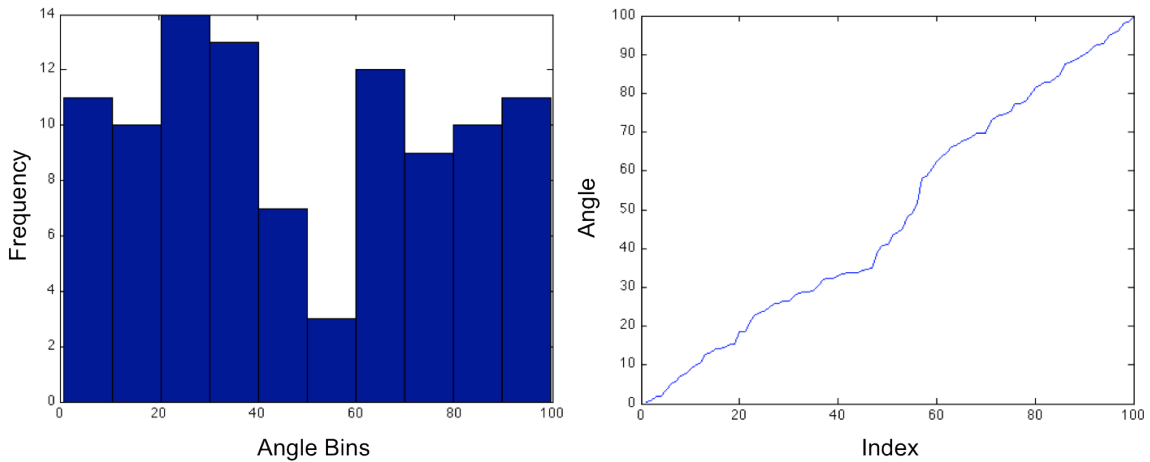


Figure 11. Computer-generated uniform random distribution ($n=100$). Histogram (10 bins) plotting frequency as a function of “angle” bins (left). Plot of uniform random distribution of “angles” (ordered lowest to highest), plotted as a function of index (right). Angle binning trends semi-linearly with the index in a uniformly distributed data set.

Thus, if the set of alignment angles is ordered in increasing order, begin with an empty set, and add angles to the set in order of increasing angle, at some point there should exist a set with a (nearly) uniform distribution, and if too many angles are added to the set, the uniformity disappears. It remains, therefore, to determine the angle for which that uniformity disappears. For this, an algorithm based on the so-called normalized cumulative periodogram is appropriate (Hansen *et al.*, 2006), called the NCP-criterion.

Algorithm Accuracy

To assess the precision of the algorithm, a randomly selected data set ($n=15$ cells) was reassessed for alignment and compared to the original data. The individual alignments were compiled as vectors, \mathbf{v}_{old} and \mathbf{v}_{new} . Variation in degree output was determined using the L1-norm divided by the sample size:

$$\sum_{i=1}^n |\mathbf{v}_{old,i} - \mathbf{v}_{new,i}| / n$$

Equation 12. L1-norm.

Quantification of Cellular Metabolism and Proliferation

DNA quantification

To quantify relative cell counts per well, Picogreen dsDNA assay (Invitrogen) was performed according to the manufacturer's protocol. Briefly, the P19 cells were permeabilized with 1 ml of a 0.1% Triton X-100 solution in the treatment wells, before being agitated with a pipette tip to shear the cells and release the DNA. The experimental DNA solution was then collected in Eppendorf tubes and stored until assay. To quantify DNA content, triplicates of each sample (25 μ L) were added to wells of a 96-well plate, after being vortexed for three seconds. Then, 75 μ L of 1X Tris-EDTA (TE) buffer and 100 μ L Working A solution (from manufacturer) were added to each well, before being incubated for 30 minutes away from light. Samples were read on a fluorometer, followed by interpolation based on a standard curve from λ DNA.

Metabolic assay

To quantify cellular metabolism, the chemical (3-(4,5-Dimethylthiazol-2-yl)-2,5-diphenyltetrazolium bromide (MTT) assay was performed according to the manufacturer's protocol (Invitrogen). A 5 mg/ml sterile-filtered MTT solution in PBS was diluted 1:10 in serum-free media. One milliliter MTT-media solution was added to each well, followed by a incubation for 2 hours at 37°C. The supernatant was then collected and discarded. Next, 500 μ l dimethyl sulfoxide (DMSO) was added to each well, and the silk films were broken with a micropipette tip. The solutions were then collected and centrifuged for 10 minutes at 1260 rpm. The remaining solutions were then analyzed for absorption spectra at 540 nm.

Imaging

Flat and micropatterned silk films

The silk films were examined for surface morphology using a scanning electron microscope (SEM) with an InLens detector (Supra55VP, Zeiss). Prior to imaging, the films were coated with platinum/palladium.

P19 cell imaging

The P19 neurons were imaged using both phase contrast microscopy (DM IL, Leica) and confocal imaging (DM IRE2, Leica). Prior to confocal microscopy, the cells were permeabilized for 15 minutes at room temperature using a 0.5% Triton X-100 solution in Dulbecco's phosphate buffered saline (PBS, Sigma-Aldrich). Blocking was then done for 30 minutes at room temperature using a 3% bovine serum albumin (BSA, Sigma-Aldrich) solution in PBS. The cells were then stained for actin using a 1:50 dilution of Alexa Fluor 488 phalloidin (Invitrogen) for 45 minutes and counterstained for the nucleus for 20 to 30 minutes using a 1:1000 dilution of a 10 mg/ml Hoechst 33342 (Sigma-Aldrich) or propidium iodide (Invitrogen) solution, according to the manufacturers' protocols. Prior

to imaging, the cells were then gently rinsed with PBS and maintained in PBS throughout imaging.

PC-12 cell imaging

Fluorescence images of the PC-12 cells were obtained using confocal microscopy (DM IRE2, Leica). Prior to imaging, the cells were fixed for 20 minutes in 10% formalin, followed by permeabilizing for 30 minutes at room temperature using a 0.5% Triton X-100 solution in PBS. The cells were then stained as described for the P19 cells, with the exception that the only nuclear stain used was Hoechst 33342. Additionally, for imaging PC-12 cells on silk films using confocal microscopy, slides were made. Silk films were mounted onto glass slides, treated with an anti-fade agent, and dried overnight prior to imaging (Dako, Carpinteria, CA).

Live calcium imaging

To quantify the molecular response of differentiated PC-12 cells to the bradykinin receptor family agonist bradykinin, live calcium imaging was performed using fluorescent dyes. Fluo-4 is a green fluorescent calcium dye commonly used in live cell imaging (Gee *et al.*, 2000). In the current experiment, the non-fluorescent analog of fluo-4, fluo-4 acetoxymethyl ester (Fluo-4 AM) was used (Invitrogen), which is cleaved to the fluorescent fluo-4 compound (Fig. 12) once inside of the cell.

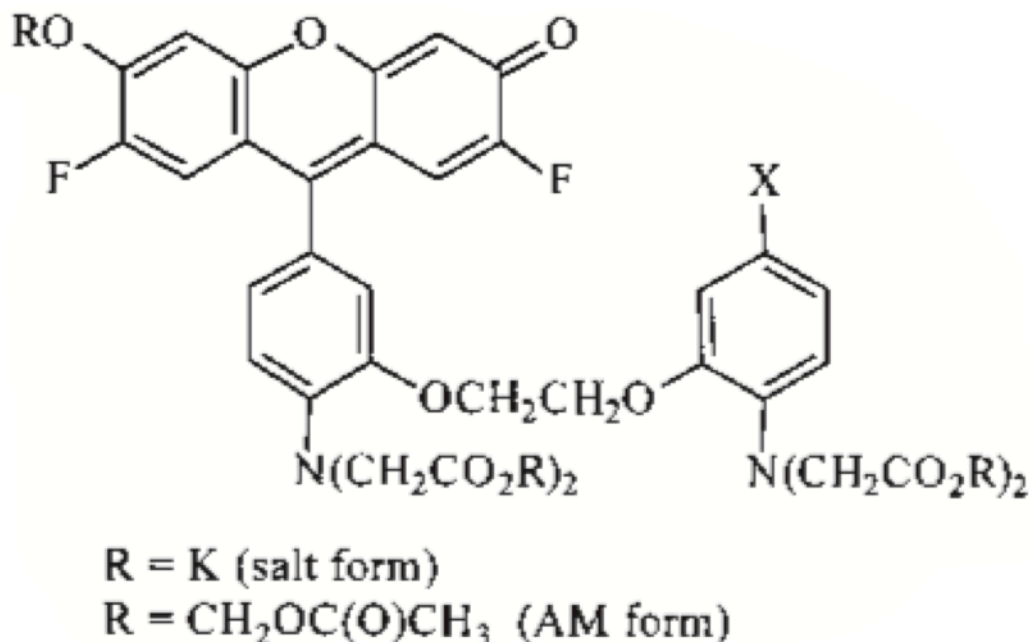


Figure 12. Fluo-4 dye molecular structure with and without acetoxymethyl ester group (AM, indicated as on of the R groups, bottom). Image taken from Gee *et al.*, 2000.

For live calcium imaging, fluo-4 AM dye was administered to the cells prior to imaging, according to the manufacturer's protocol (Invitrogen). Briefly, a 5 mM fluo-4 AM

solution in DMSO was diluted in phenol red-free Hank's buffered saline solution (HBSS, Sigma-Aldrich) modified with the addition of calcium and magnesium, to a final concentration of 5 μM and added to the PC-12 cultures, followed by a 60 minute incubation at 37°C. The cultures were then gently rinsed and incubated in HBSS for another 30 minutes to allow for complete de-esterification of the acetoxymethyl ester. Real-time imaging was performed using fluorescence confocal microscopy. A 488 nm argon laser was used for excitation, and the emission spectra were collected in the same range as green fluorescent protein (GFP). Time-lapse imaging was performed with two-second time resolution to properly observe calcium wave dynamics.

To experimentally perturb PC-12 calcium dynamics, bradykinin (Sigma-Aldrich), a BK receptor agonist, was used. Cells were imaged for 5 minutes prior to the introduction of the agonist to achieve a baseline fluorescence measurements, followed by 5 minutes imaging post-delivery. During imaging, the cells were bathed in the HBSS described above. Imaging was performed at room temperature, and solutions added to the cultures were warmed up to 37°C prior to imaging. Bradykinin was delivered to the cells at a final concentration of 50 μM .

Controlled Drug Release

Microsphere and film fabrication

Microspheres were prepared according to the lipid template protocol previously described (Wang *et al.*, 2007), using a ratio of 1 μg growth factor (GDNF or NGF) per ml of 8% silk solution (created using the protocol described above). This is a ratio of 10^{-3} mg growth factor per 80 mg silk (w/w). Bulk loaded silk films were cast in a low-protein-binding 48 well plate using a 0.5 $\mu\text{g}/\text{ml}$ solution of GDNF or NGF in concentrated silk (~25-30% w/v). A volume of 150 μl growth factor was used per film, with a total quantity of 0.45 μg growth factor per film. Microsphere-loaded films were prepared using 40 mg of silk microspheres per ml of concentrated silk solution. A volume of 150 μl of growth factor was used per film for a total loading of 6 mg growth factor per film.

Simplified drug release models show potential mechanisms of drug delivery. While the primary barrier for bulk-loaded drug (Fig. 13) is the silk scaffold (a primarily diffusion-based mechanism), microsphere-embedded films (Fig. 14) provide a secondary barrier to release, potentially delaying and extending the period over which drug is released into the desired system.

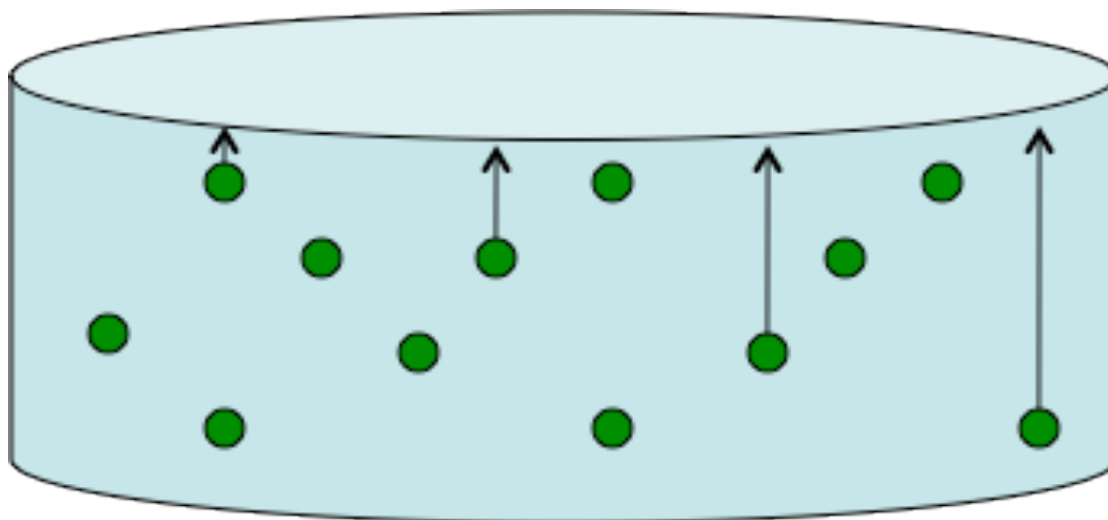


Figure 13. Silk fibroin films (light blue) bulk-loaded with GDNF (green).

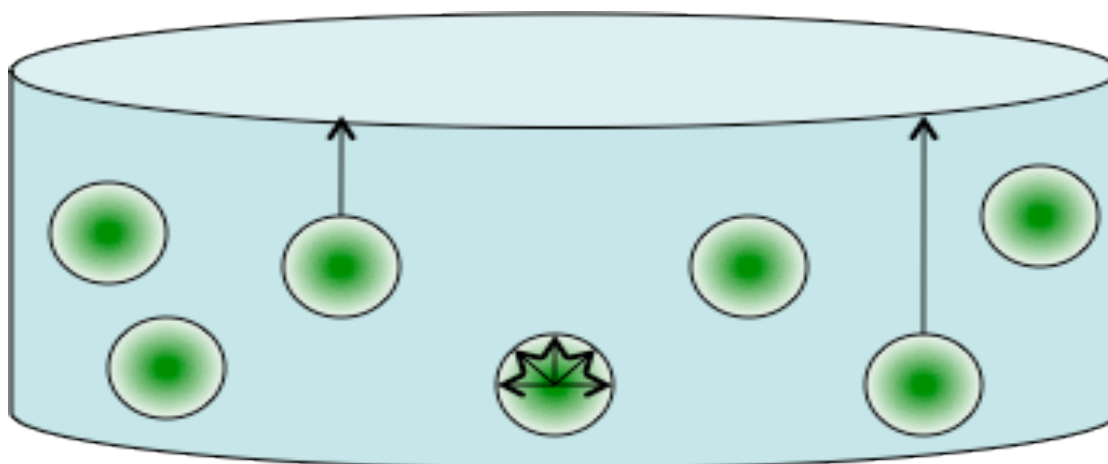


Figure 14. Silk fibroin films (light blue) embedded with GDNF microspheres (green).

Growth factor release studies

Studies were conducted with n=6 samples. For the bulk-loaded group (processing described above), the silk films were placed into 0.3 ml of PBS in low-protein-binding Eppendorf tubes. For the microspheres group, 4 mg of microspheres were suspended into 0.3 ml of PBS in low-protein-binding Eppendorf tubes. Studies were conducted at 37°C with shaking. Samples were collected over the course of two weeks, on days 1, 3, 6, 10, and 14. For each sample collection in the microspheres group, the microsphere solutions were centrifuged at 10,000 RPM for 5 minutes, before having the PBS supernatant collected. The microspheres were then resuspended in 0.3 ml fresh PBS.

Growth factor bioactivity assay

A bioactivity assay was conducted to assess growth factor viability post-release. Studies were conducted with $n=6$ samples, and three different treatment groups. PC-12 cells were exposed to either negative control media (growth medium with no growth factors), positive control media (growth medium supplemented with 50 ng/ml NGF, replenished every other day), or silk fibroin films bulk-loaded with glial cell line-derived neurotrophic factor (GDNF), eluting ~ 270 pg GDNF per day (see Results section). Bioactivity levels were determined using a simple PC-12 neurite outgrowth/differentiation assay. Cells expressing neurites of length greater than or equal to the length of the neuron soma (cell body) were counted as differentiated.

Statistics

Cellular adhesion studies

Statistical analysis was performed using a two-sample Student's t-Test. A p value of 0.05 was statistically significant. Measurements are represented as mean \pm standard deviation. Standard deviation is reported in the bar graphs.

Normalized cumulative periodogram

Statistical analysis was performed using Kolmogorov-Smirnov limits, to determine acceptable fluctuations in the data reflecting a uniform distribution. Data sets were considered "uniform" if contained within the boundaries of the Kolmogorov-Smirnov limits.

Results

Neuronal Interactions with Silk Fibroin Films

Silk fibroin films for the alignment of P19 neurons

Different silk films were manufactured to investigate the effects of groove width and pitch angle on the alignment of maturing nerve cells. The flat and micropatterned silk fibroin films were first imaged for qualitative surface morphology using scanning electron microscopy (SEM) to confirm that the imprinted patterns were properly presented to the seeded cells. Imaging showed that homogeneous surfaces were presented to the P19 neurons in both the case of flat and micropatterned silk films (see Materials and Methods, Figure 4). The dimensions of these films are displayed in Table 5 (see Materials and Methods).

After characterizing the surface morphology of the silk films, neuronally-differentiated P19 cells were then plated onto laminin-coated and non-coated films and analyzed using phase contrast and fluorescent confocal microscopy. Qualitatively, the P19 neurons plated onto the micropatterned films exhibited more elongated morphologies when compared to those on the flat films (Fig. 15). After addressing cell differentiation on the silk films, cellular alignment was assessed.

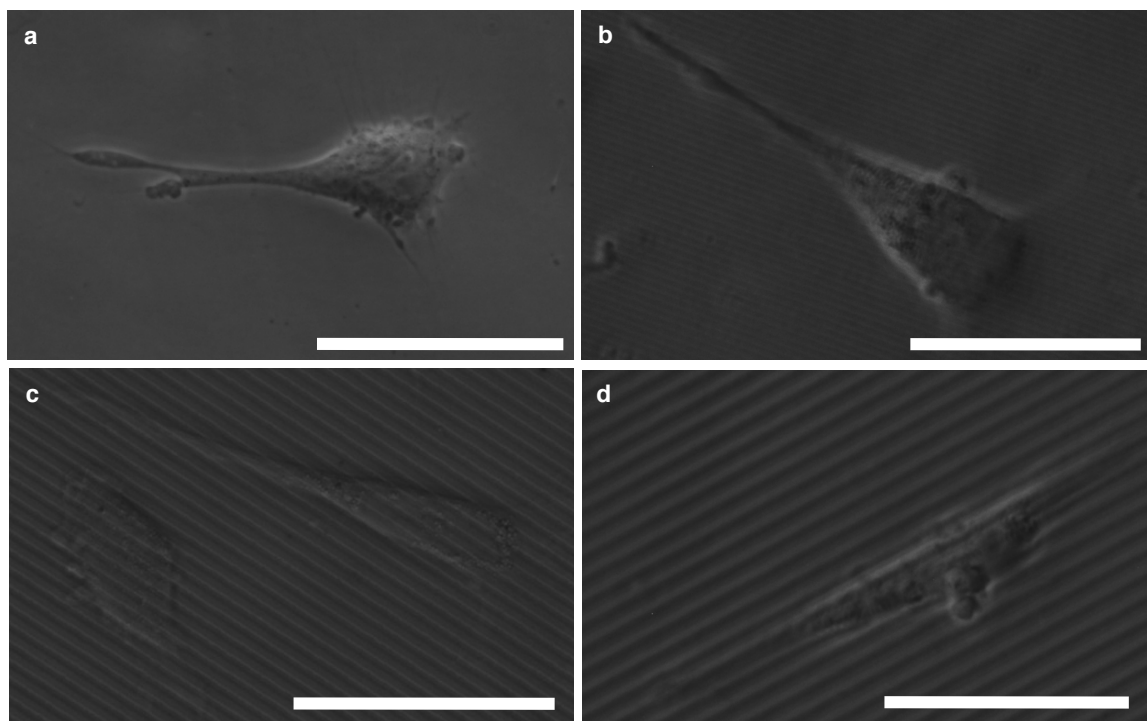


Figure 15. Phase contrast micrographs of P19 neurons on flat and micropatterned silk films. Micrographs displaying cells on flat (a) and aligned 600-17 (b), 300-8 (c), and 300-17 (d) silk films. Scale Bar, 25 μ m.

Alignment of the cells on the various silk film arrays was addressed manually based on primary (longest) neurite orientation with respect to the underlying scaffold patterning

(see Materials and Methods, Figure 5). A MATLAB algorithm was developed to manually assess scaffold and cellular alignment, with respect to one other (using the Law of Cosines). A cell was considered aligned if its longest neurite was $\leq 20^\circ$ off of the axis of alignment (the vector direction of the micropatterned films).

The degree of nerve alignment was found to be both a function of a given film's groove width and pitch angle (degree of film incline with respect to the horizontal surface) (Fig. 16). The best alignment was found using the 300-17 films (1 groove per $3.33 \mu\text{m}$, 17° angle). Cellular alignment was obtained on the order of $\sim 70\%$ for the 300-17 films, compared to $\leq 65\%$ alignment for the 300-8 films and $< 50\%$ alignment on the 600-17 films (Fig. 16). A general trend observed was that wider and deeper patterns in the micron-width range yielded superior alignment to narrower and shallower films. Additionally, greater pitch angle of silk films encourages increased alignment, based on the augmented alignment of the 300-17 films, relative to the 300-8 films. The neurons on the flat silk films had neurites evenly distributed through all of the angle bins (data not shown). Higher order alignment is most likely due to the accommodating groove width, which would allow neural processes to sink into pattern troughs. Increase in angle pitch should also promote this process, as is apparent in comparing the 300-17 and 300-8 treatment groups.

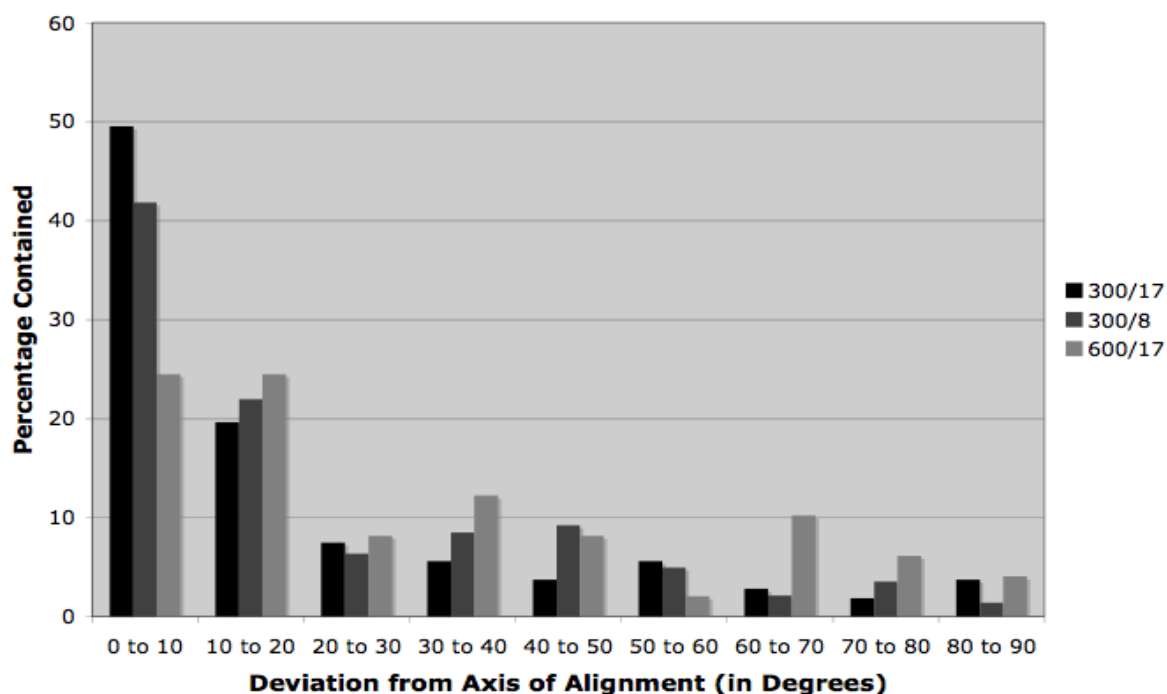


Figure 16. P19 neuron alignment on micropatterned silk films. Histogram of neuron alignment on micropatterned films after 5 days in culture (n=6).

Adhesion and proliferation on laminin-functionalized silk films

To obtain increased cellular adhesion and spread neuronal morphologies as observed in the literature (Recknor *et al.*, 2006), natural mouse laminin protein was absorbed to the silk films. Varying concentrations of laminin were used to optimize protein concentration

on the silk films. Neuronal adhesion and proliferation profiles were assessed using the PicoGreen assay (which quantifies DNA content) at 8 and 24 hours, respectively. Optimal results were observed with the addition of 5 μg laminin per film, with statistical significance observed both at the 8- and 24-hour time points ($p < 0.05$) (Fig. 17). No statistically significant difference was found between the 5 μg and 10 μg laminin-treated groups at either time point.

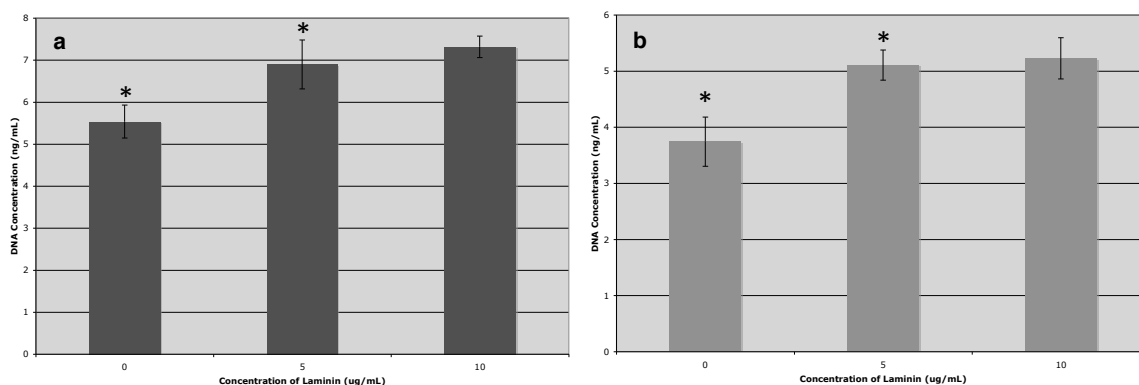


Figure 17. Nerve adhesion and proliferation profiles on laminin-adsorbed silk fibroin films. Nerve adhesion (a) and proliferation (b) assays (PicoGreen) were taken at 8 hours and 24 hours, respectively. Significance was found between all data points except for 5 μg and 10 μg laminin. * denotes significance at $p < 0.05$.

Adhesion and proliferation after systemic delivery of NGF

Short-term studies investigating the effect of nerve growth factor (NGF) on the PC-12 cell line have shown increased initial rates of cell adhesion after systemic exposure to this growth factor (Schubert and Whitlock, 1977); however, studies of this nature have not been performed using the P19 cell line. In the present study, concentrations of NGF ranging from 1-500 ng/mL were added to differentiated P19 neuron cultures, at the time of plating onto flat silk fibroin films.

A PicoGreen DNA quantification assay was then performed at designated time points to quantify relative cell counts. Optimal cellular adhesion at the 8-hour time point was observed with the addition of 100 ng/mL NGF (Fig. 18a). However, at 24 hours the statistical significance observed between the 50 ng/mL and 100 ng/mL NGF treatment groups diminished (Fig. 18b). This same effect was also observed when the same experiment was run but with the addition of 5 μg natural mouse laminin adsorbed onto each silk film prior to cell plating (Fig. 18c).

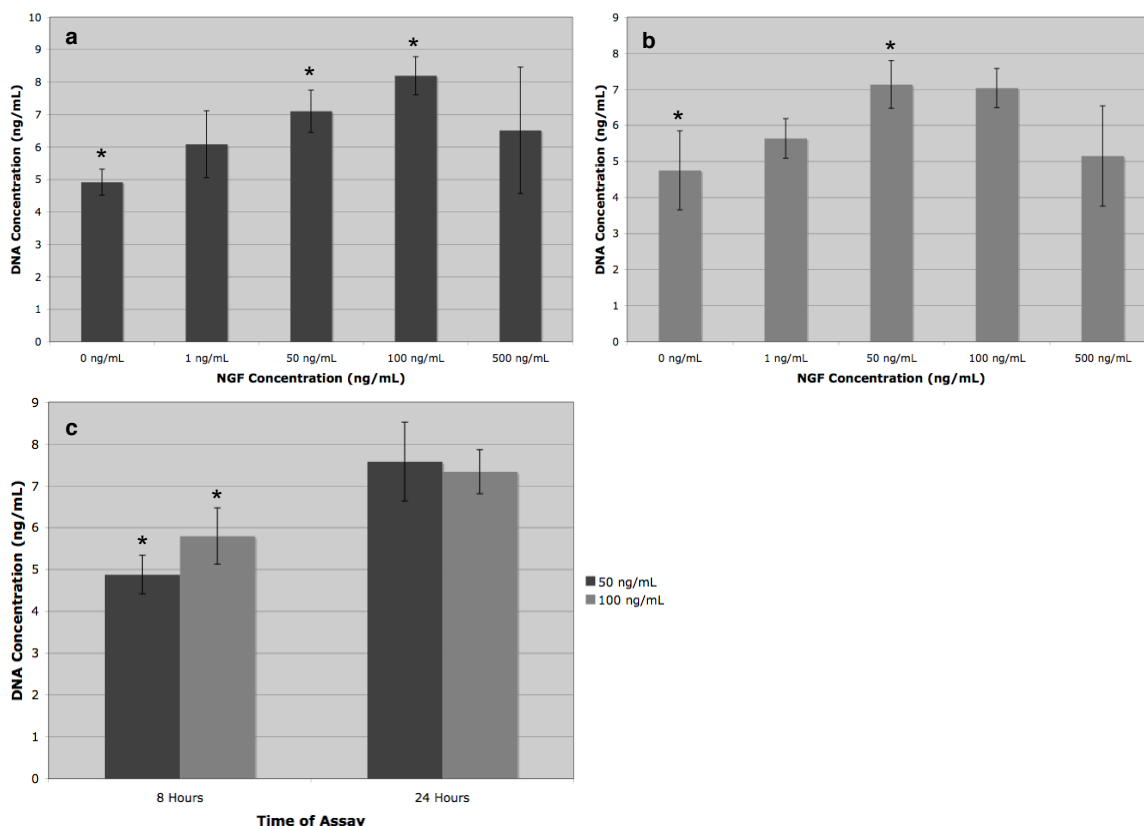


Figure 18. Adhesion and proliferation profiles after systemic delivery of nerve growth factor (NGF) to silk and laminin-adsorbed surfaces. Adhesion (a) and proliferation (b) profiles after systemic NGF delivery, on a silk fibroin surface. At 24 hours (b), the statistical significance between 50 ng/mL and 100 ng/mL diminished. c) Adhesion (8 hours) and proliferation (24 hours) of P19 neurons on laminin-adsorbed silk films, after exposure to displayed concentrations of NGF. * denotes significance at $p < 0.05$.

Bradykinin-induced Ca^{2+} fluxes in PC-12 neuronal cultures

To investigate the possibility of observing calcium (Ca^{2+}) dynamics of PC-12 cells in culture, live calcium imaging was performed during the introduction of bradykinin, an agonist of the bradykinin receptor family. Live calcium imaging is a non-invasive mechanism for assessing some of the molecular and electrophysiological properties of neuronal populations in culture. After PC-12 neurons were differentiated with NGF (for > 1 week), calcium fluxes were measured in response to bradykinin with time resolution on the order of two seconds. Calcium dynamics specifically within the neuron soma (cell body) were investigated. Visual characterization revealed significant changes in calcium concentrations within the neuron soma (Fig. 19). Quantification of relative changes in intracellular calcium concentrations was performed using ImageJ software (NIH).

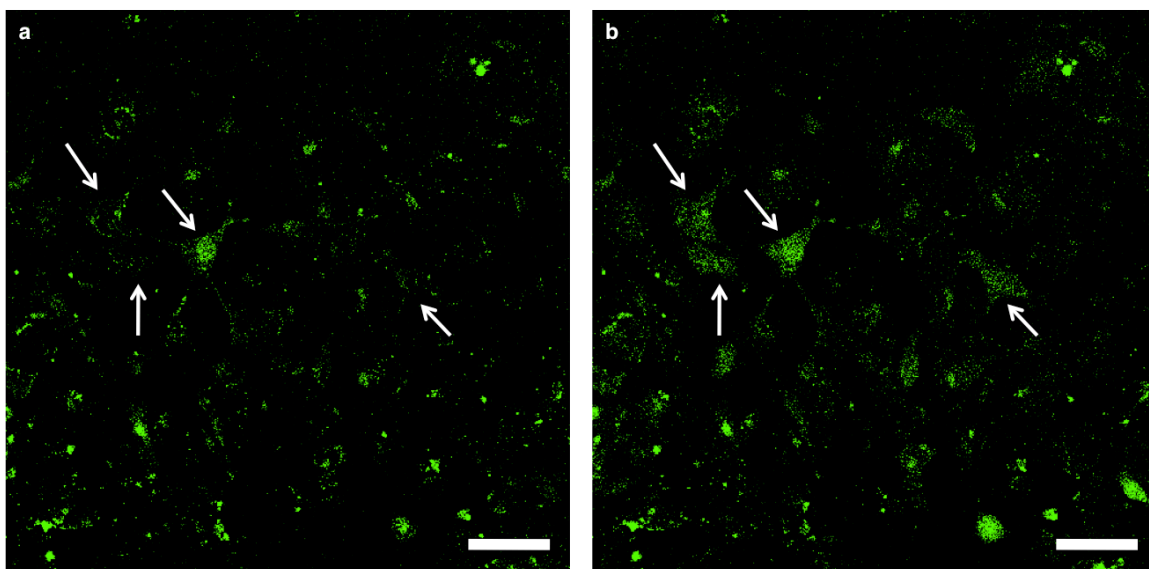


Figure 19. Live calcium imaging of PC-12 neurons on glass surfaces. Images reveal intracellular calcium fluxes before (a) and after (b) introduction of bradykinin to the culture. Arrows indicate cells that were selected for analysis of calcium spiking dynamics. Scale bar, 50 μm .

The calcium dynamics of the PC-12 neuron soma were found to be highly sensitive to bradykinin, reaching intracellular calcium levels up to 4.5 times higher than normal (value is based on population response) (Fig. 20, right). PC-12 responses to bradykinin, on a cell-by-cell basis were observed to be fairly heterogeneous and scaled (Fig. 20, left). The measurable temporal response of the PC-12 cells to the agonist suggest that confocal microscopy for live dynamic calcium imaging may be suitable for testing neuronal cell viability and excitability on biomaterial scaffolds.

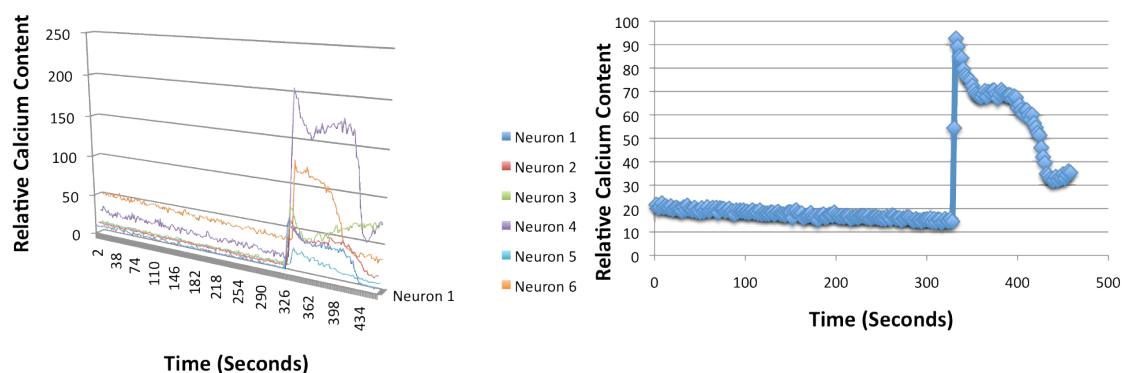


Figure 20. Intracellular PC-12 calcium dynamics in response to the bradykinin receptor family agonist, bradykinin. Individual cells (left) reveal a heterogeneous (scaled) response of the PC-12 cells to bradykinin. Population response (right) shows a ~4.5 fold increase in intracellular calcium in response to bradykinin.

Controlled Drug Release

Silk fibroin films for the controlled release of neurotrophic factors

Studies investigating the controlled release of glial cell line-derived neurotrophic factor (GDNF) and growth factor bioactivity were conducted. For controlled release studies, two different drug delivery mechanisms were chosen based on desirable release properties for applications in peripheral nerve tissue engineering: burst release and slow, delayed release. For burst release kinetics, microspheres alone in solution were used. For delayed release, silk films containing bulk-loaded growth factor, and microspheres embedded in silk films were used.

Microspheres alone in solution showed burst release kinetics, eluting ~65% of the encapsulated growth factor on Day 1 (Fig. 21a). Embedding these silk microspheres into silk fibroin films was able to significantly slow the release, yielding a logarithmic release profile. This limited the release of the neurotrophic factor to ~40% elution on the first day (Fig. 21b). Bulk-loaded silk films yielded a supra-linear release profile up to Day 3, after which the films linearly eluted ~270 pg GDNF per day ($R^2=0.99$) for the duration of the experiment (14 days) (Fig. 21c). These varying release profiles offer different modalities of drug release for neural tissue engineering.

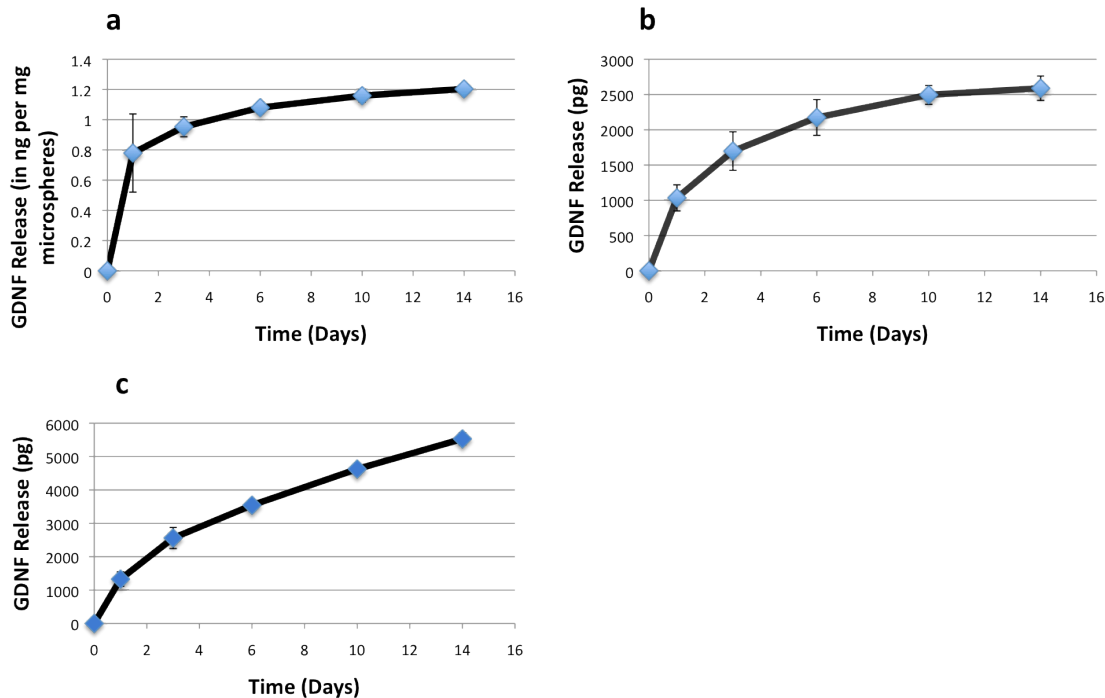


Figure 21. Cumulative GDNF release profiles from different silk biomaterial modules over two weeks. a) Silk microspheres, alone, in solution. b) Microsphere-encapsulating silk films. c) Bulk-loaded silk films.

Post-release GDNF bioactivity

Short-term studies investigating glial cell line-derived neurotrophic factor (GDNF) bioactivity after encapsulation in silk biomaterials were conducted. An adhesive variant of the PC-12 cell line, a neurotrophic factor-sensitive cell population, was used. After 5 days in culture, the cells were stained (for their cytoskeleton and nucleus) and imaged using fluorescent confocal microscopy to observe neurite outgrowth. Cells were considered “differentiated” if the length of their primary (longest) projection was greater than or equal to the length of the neuron soma (cell body). Examples of differentiated cells are shown in Figure 22b and 22c.

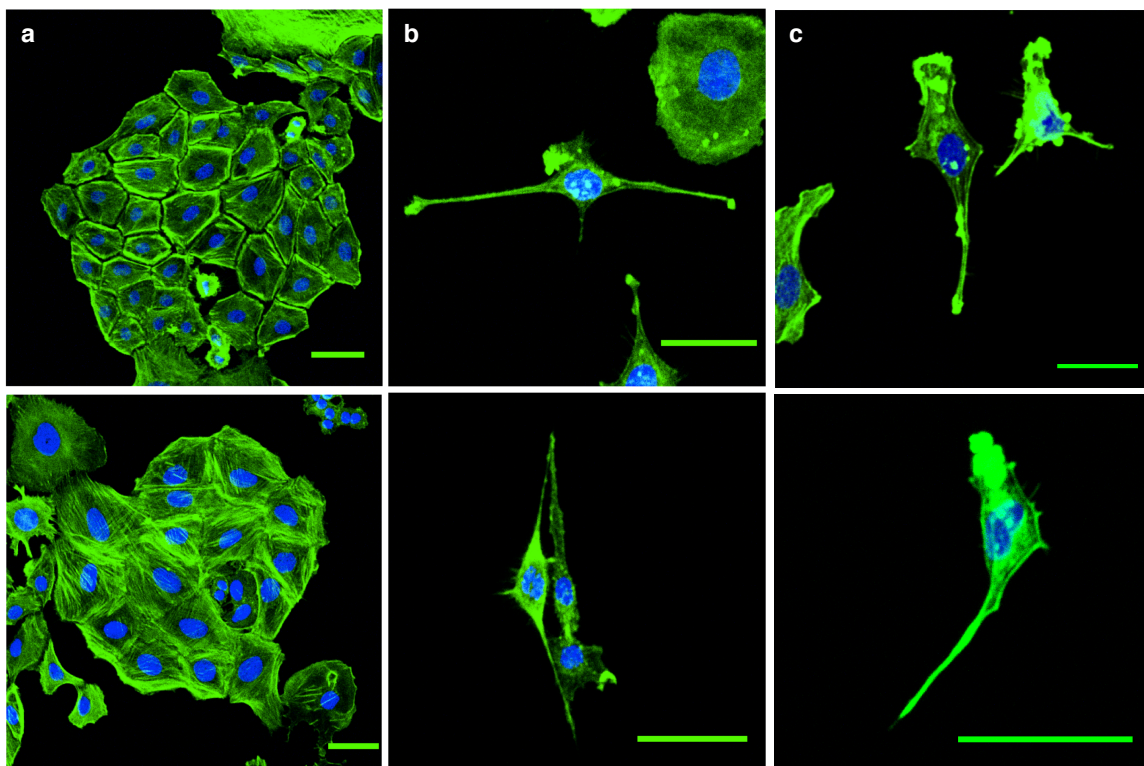


Figure 22. Bioactivity assay for PC-12 neurite outgrowth after neurotrophic factor delivery. a) Negative control (no neurotrophic factors). b) Positive control (50 ng/ml NGF). c) Experimental group, bulk-loaded glial cell line-derived neurotrophic factor (GDNF) eluting ~270 pg/day. Actin cytoskeletal stain (phalloidin) with nuclear counterstain (Hoechst 33342). Scale Bar, 50 μ m.

Minimal differentiation was seen in the negative control group, which received no growth factors. The negative control population was characterized by colonies of proliferating, undifferentiated cells as seen during expansion of the PC-12 cell line (Fig. 22a). Marked neurite outgrowth was observed in both the positive control (treated with 50 ng/ml NGF) and the group treated with silk films containing bulk-loaded GDNF (Figs. 22b-c). The bulk-loaded GDNF films outperformed the negative control 2-3 times over, with respect to percentage differentiation (Fig. 23). Neurite outgrowth in the bulk-loaded GDNF group is indicative of retention of growth factor bioactivity post-release.

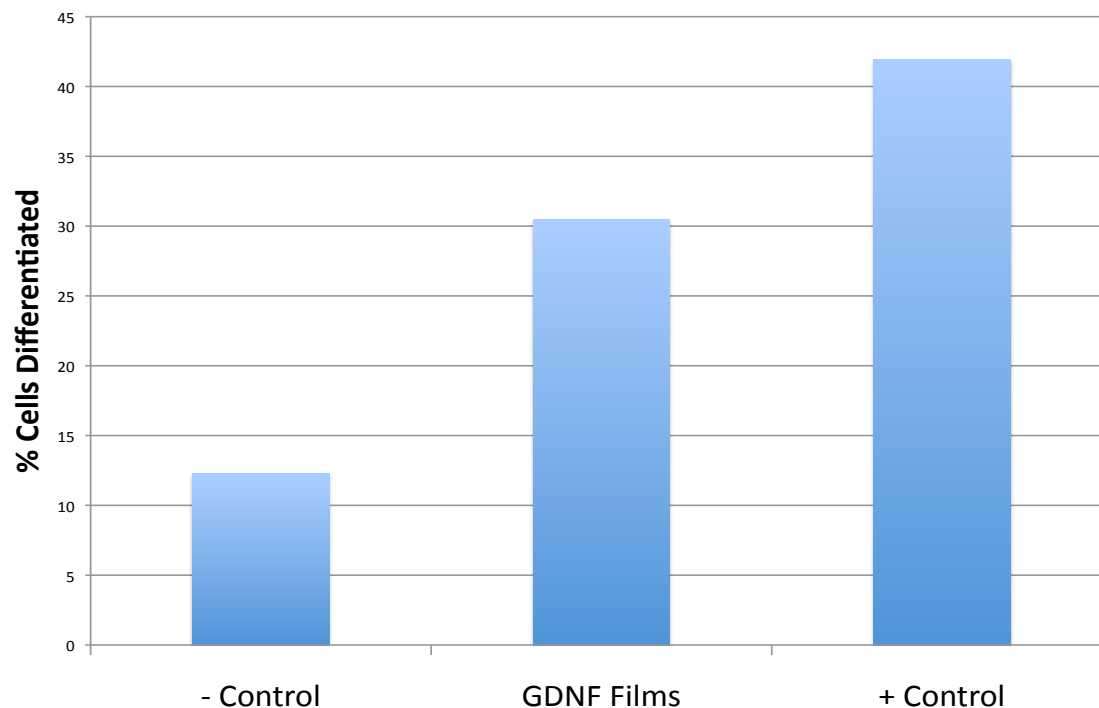


Figure 23. PC-12 neurite outgrowth quantified after neurotrophic factor delivery. $n \geq 200$ per treatment group.

Automated Assessment of Cellular Alignment

PC-12 neurons were grown on two different silk films (one micropatterned, 300-17 film, and another flat film) for 7 days, and then imaged for cellular alignment. An automated algorithm was developed for quantitatively assessing the alignment of PC-12 neurons on the silk fibroin films. From two images, a transmission image of the scaffold surface (see Materials and Methods, Figure 8, top) and a fluorescent confocal micrograph of the neuron (Fig. 24), this algorithm was able to quantify the relationship between the cell and the film's axis of alignment, determined to be the angle of alignment. Additionally, other elliptical parameters could be extrapolated based on the convergence of the ellipse on the neuron, using the Gauss-Newton algorithm.

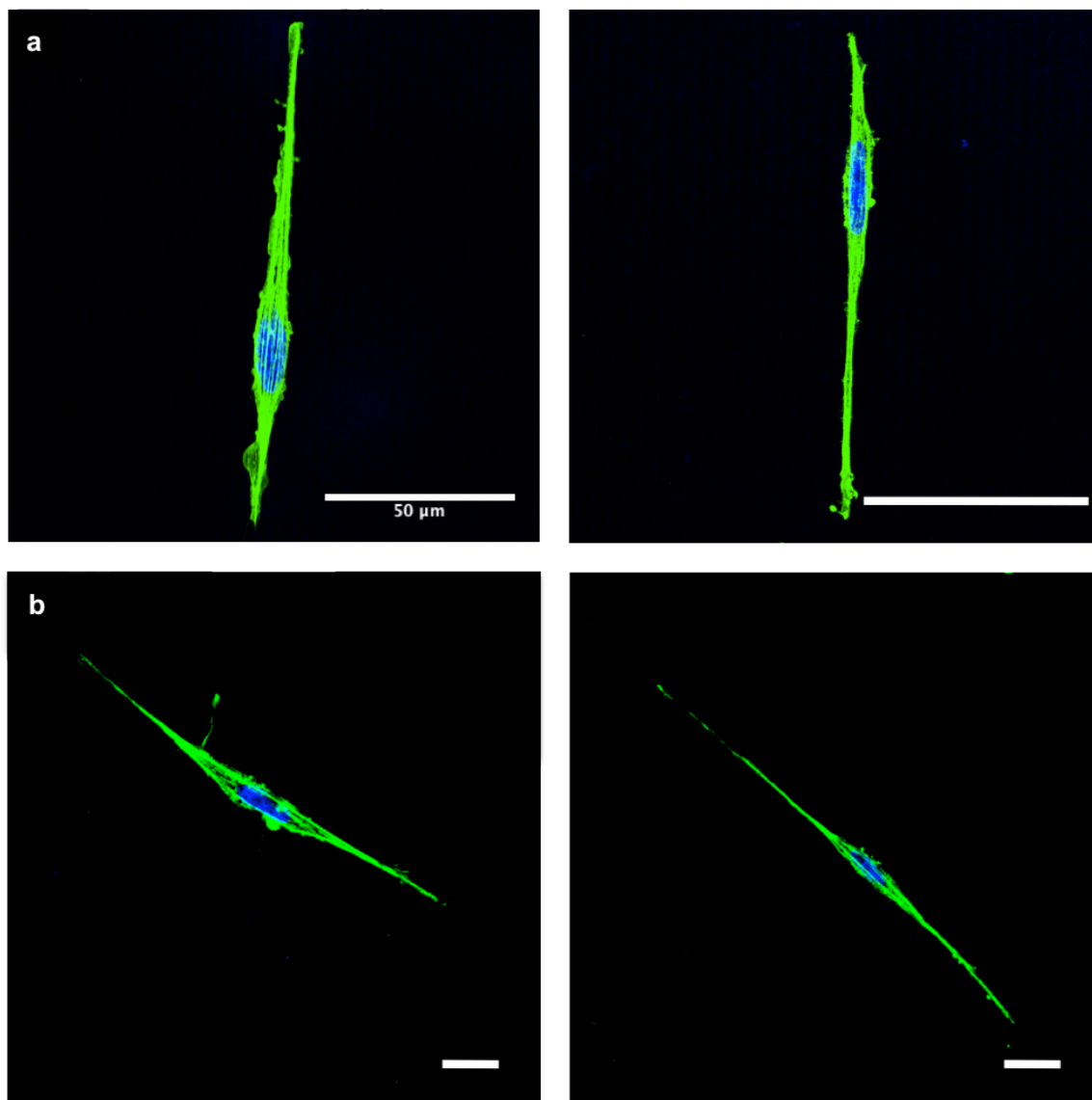


Figure 24. PC-12 neurons on micropatterned (a) and flat (b) silk films. Cells are stained with phalloidin (for actin cytoskeleton) and counterstained with Hoechst 33342 (for nucleus). Scale bar, 50 μm .

Cellular image processing

The confocal micrographs (Fig. 24) of the PC-12 neurons were collected and analyzed. The first step in the algorithm is to threshold and discretize images of the cells, so that the Gauss-Newton algorithm may converge on a discrete set of pixels. The process of image thresholding is shown below, in Figure 25 (cells on micropatterned films) and Figure 26 (cells on flat films).

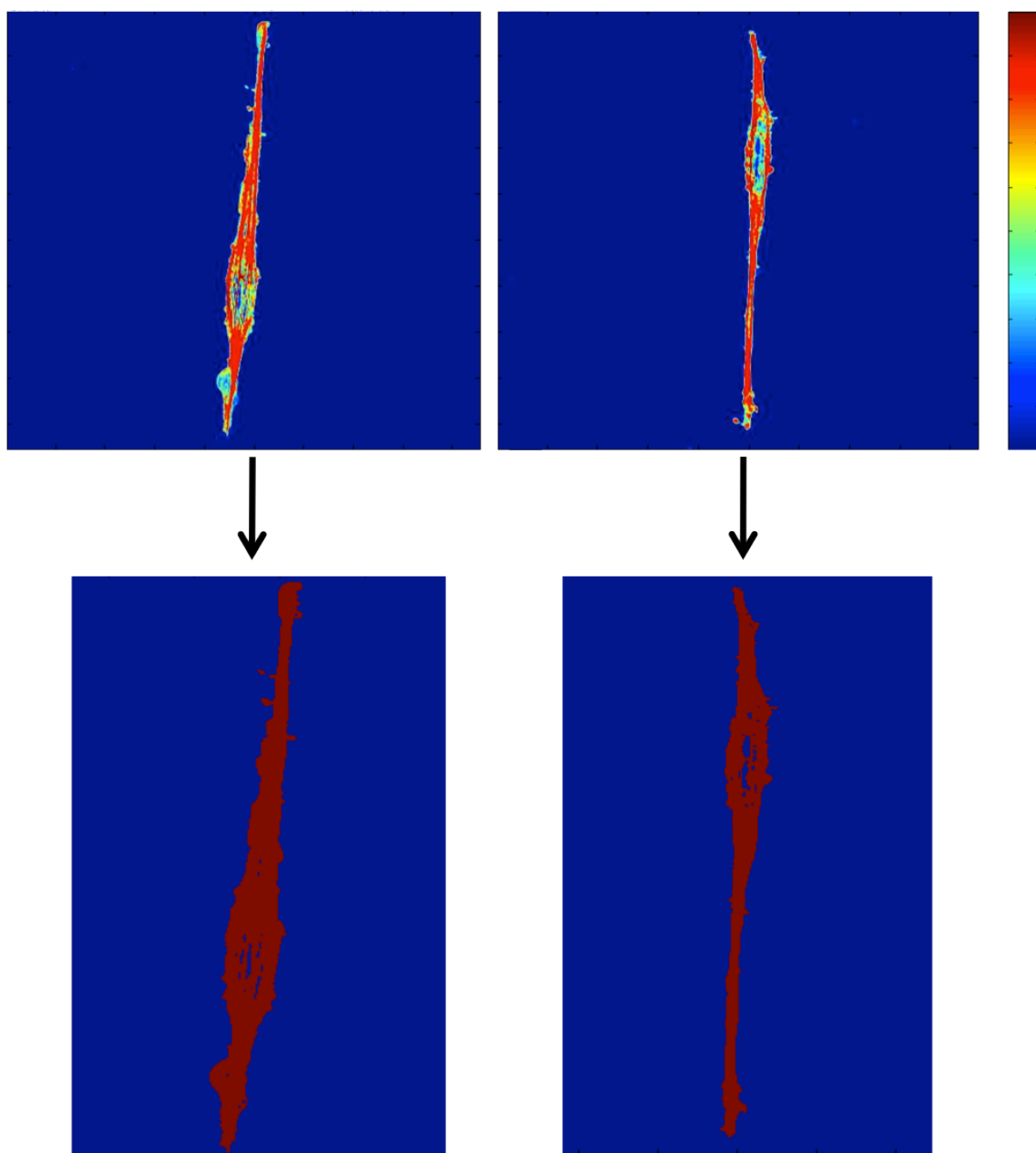


Figure 25. Scaled images of PC-12 neurons on micropatterned silk films (from images in Figure 24a). Images were scaled from fluorescent micrographs and then discretized.

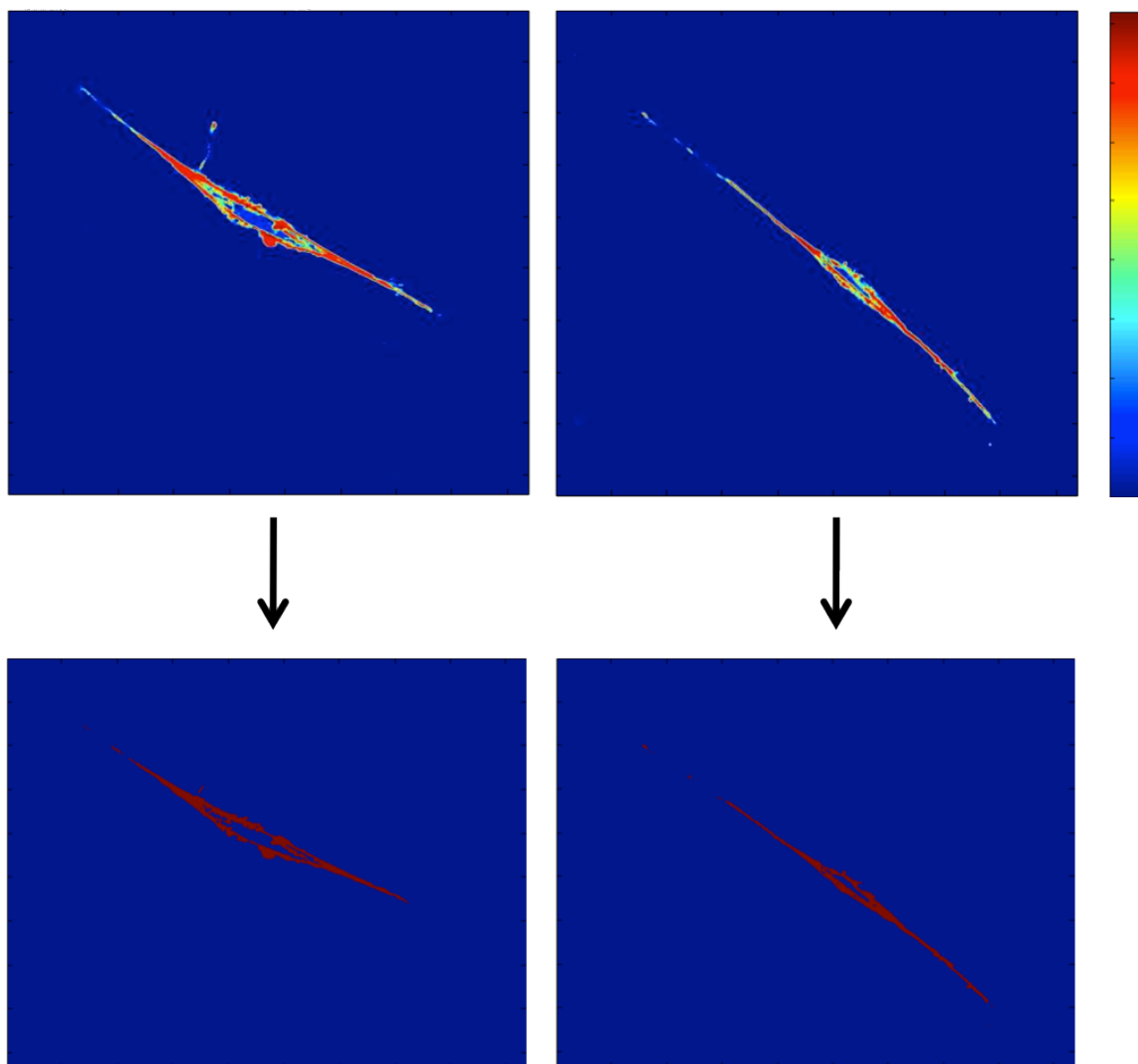


Figure 26. Scaled images of PC-12 neurons on flat silk films (from images in Figure 24b). Images were scaled from fluorescent micrographs and then discretized.

Scaffold image processing

Confocal micrographs (Fig. 27) of the underlying micropatterned silk films were collected and analyzed, alongside the cellular data. The next step in the algorithm is to calculate the angle of the silk scaffold with respect to the x-axis. Thus, this portion of the algorithm takes the collected transmission image of the micropatterned silk films and converts it into a value, theta, which is the angle of the micropatterns with respect to the horizon (x-axis).

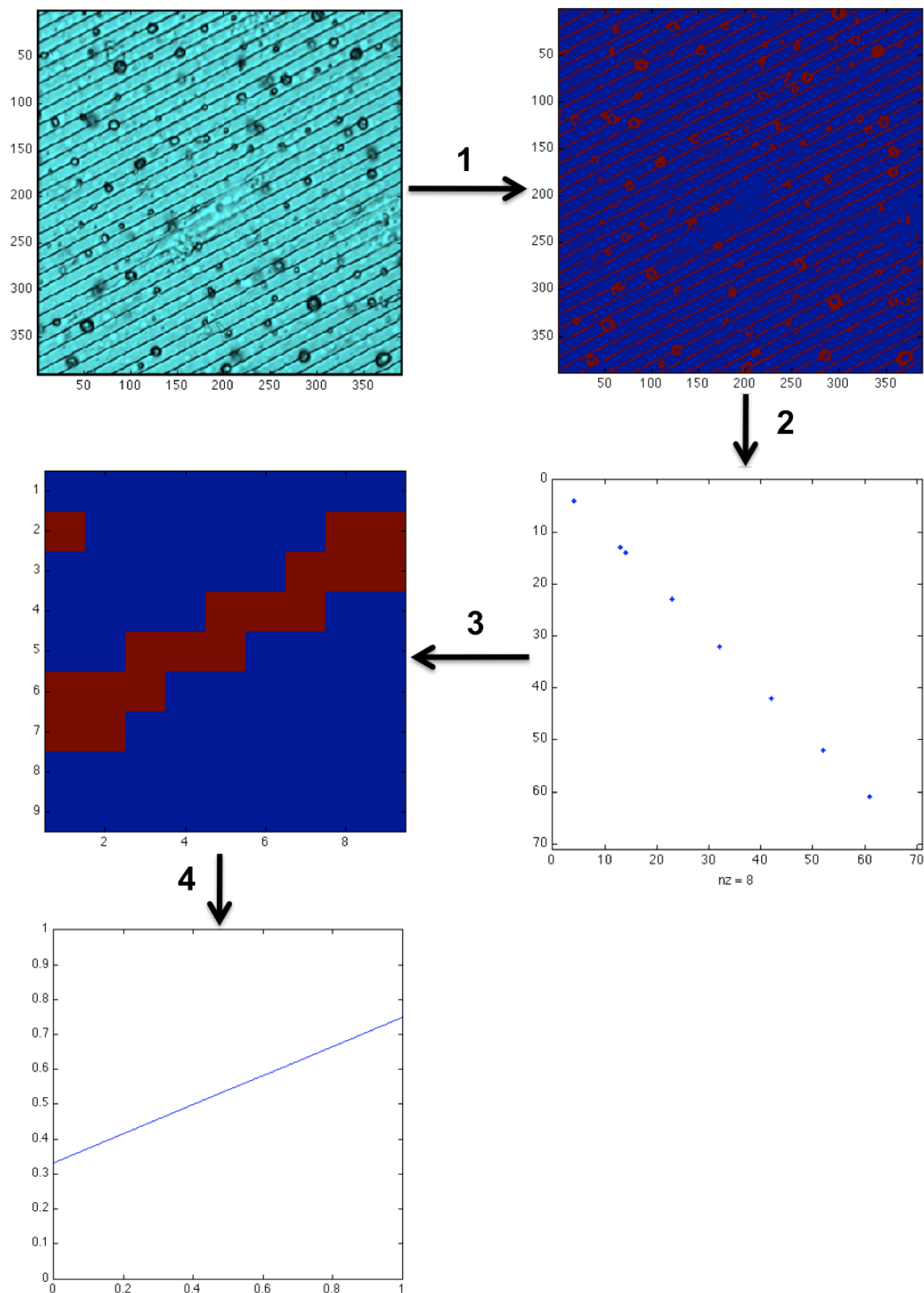


Figure 27. Scaffold image processing scheme. The original transmission image (top left) is converted into a binary, sorted image (1), analyzed for groove spacing (2), translated into a ~ 1 pixel-wide image (3), and fit with a linear least-squares regression to yield an angle output (4).

The algorithm was able to accomplish the above goals, through the following steps (Figure 27): 1) The transmission image of the micropatterned silk film is analyzed using k-means clustering, a method of cluster analysis, which takes the image data and finds a group of k clusters (means), around which n observations are distributed (the i^{th} observation is clustered with the mean to which it is closest). In the case of the current algorithm, 6 different means were selected, and this led to the isolation of a series of repeating ~ 1 pixel-width lines, which corresponded one-to-one with the valleys of the micropatterns. 2) These lines were then identified through their periodicity (repeats), by dividing the subimage with the image output of an identity matrix (see Materials and Methods for greater detail). The intersection of the identity matrix and the periodic lines is then plotted. 3) Once these lines are identified, the algorithm selects one of the intersecting lines, which is a set of pixels, which take on discrete values (0 or 1). The patterns correspond to a pixel value of 1. 4) After this line is isolated, a simple linear least-squares line fit is performed on this set of pixels, and a vector output is the result. The angle of this vector with respect to the x-axis is the same angle of the micropatterns with respect to the horizon.

Angle outputs

To solve for the angle between the micropatterns and the cells, a simple calculation is required. Because both angles obtained are with respect to the x-axis, subtraction between the two obtained values yields the difference (in angle) between the film and cell. A population analysis was performed on the alignment data collected from PC-12 neurons plated on both flat and micropatterned silk films. Based on earlier calculations, a 7-bin histogram displaying the absolute orientation of the PC-12 neurons was constructed, with a bin width on the order of ~ 12 degrees per bin for flat films, and ~ 10.6 degrees per bin for micropatterned films. Data from flat films ($n = 47$) and micropatterned films ($n = 127$) is displayed in Figure 28.

For the flat films, the center of the first bin was 10.55 degrees, with 7 cells falling within this bin ($< 15\%$ alignment). For the micropatterned films, cellular alignment was on the order of $\sim 65\%$, with 82 neurons falling within the first bin. It is visually apparent that there are linear trends in both data sets, which underlie statistical distributions. In the current case, this is the uniform distribution. To further analyze these data sets, a normalized cumulative periodogram (NCP) is required to understand when the data set transforms from a uniform distribution to something else.

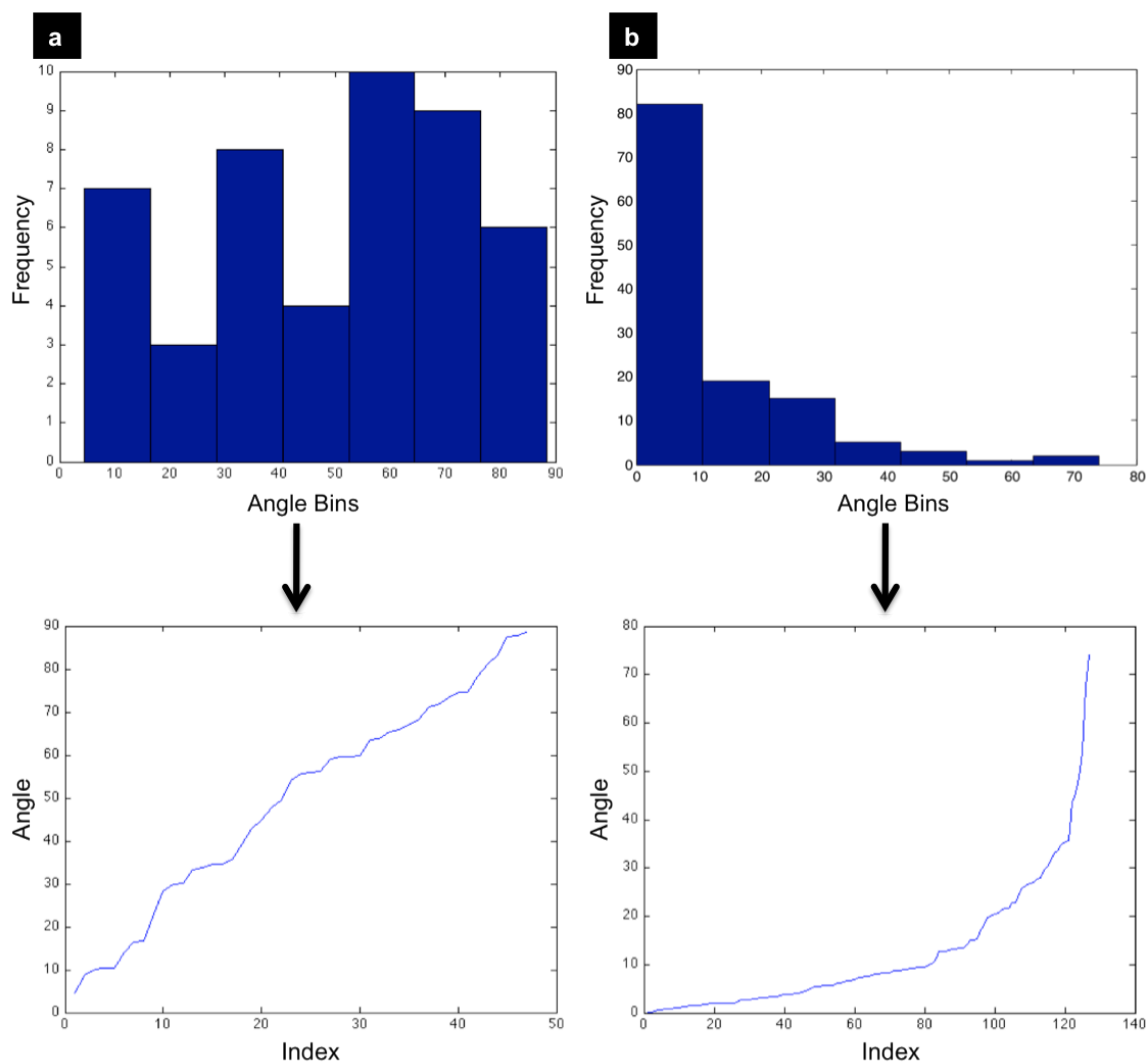


Figure 28. PC-12 neuron alignment data on flat (a) and micropatterned (b) silk scaffolds. Histograms (top) display binning of cells in angles ranging from 0-90 degrees. Angle distributions (bottom) reveal trends in the data, which contain underlying probability distributions. Bottom data is further analyzed using the normalized cumulative periodogram (NCP).

Normalized cumulative periodogram

To better understand the underlying probability distributions from cellular alignment data, the normalized cumulative periodogram (NCP) was used to assess uniformity in cellular alignment. Uniformly distributed data on a NCP trends semi-linearly. This technique was also applied to the micropatterned silk film data to observe the divergence of cellular alignments from a uniform distribution (Fig. 29). Uniform distribution is observed to diminish at NCP #22, which corresponds to an angle of ~ 2 degrees.

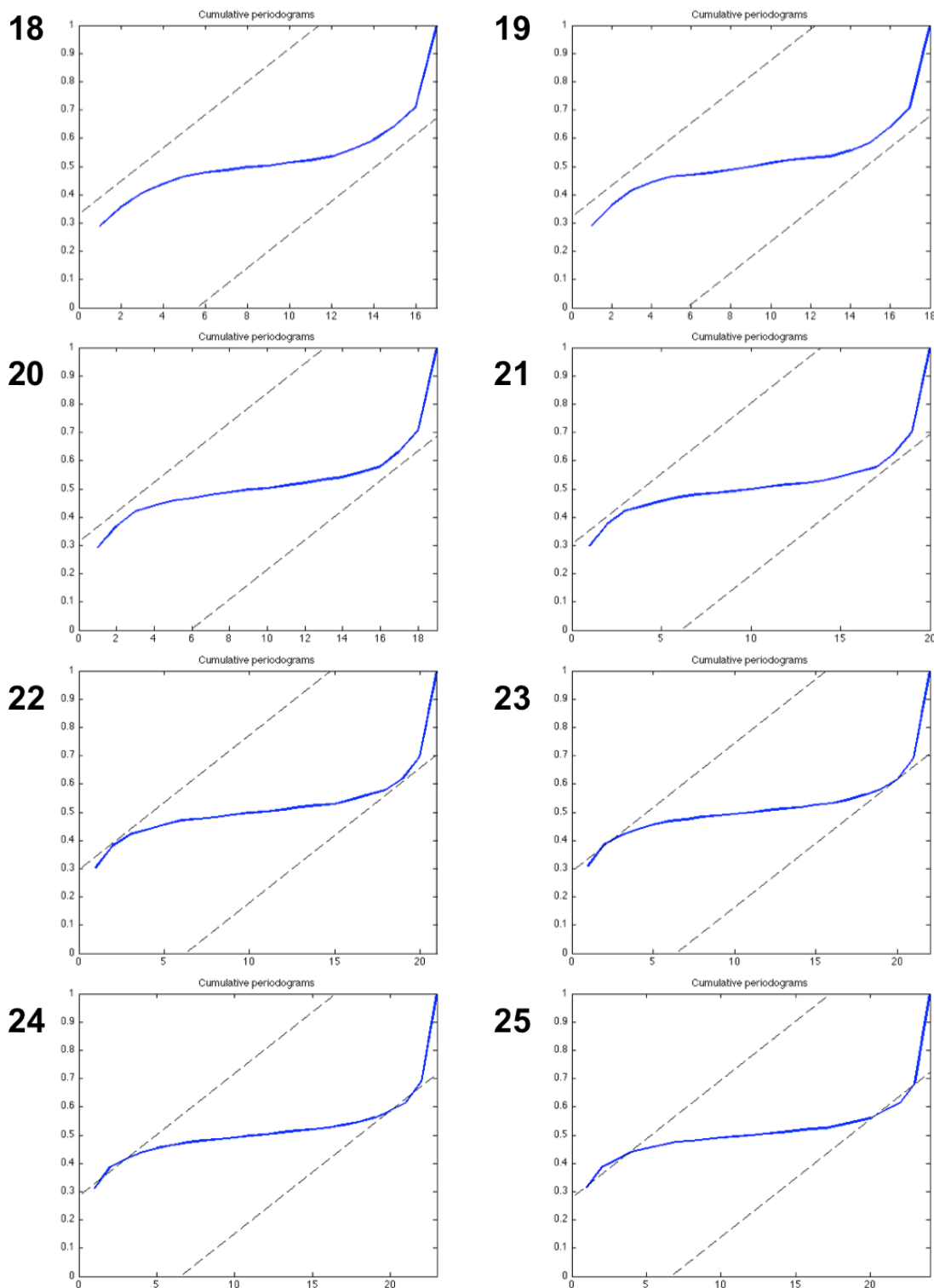


Figure 29. Normalized cumulative periodogram (NCP) of neuron soma angle distributions on micropatterned silk films. Uniform distribution threshold is observed at NCP #22.

Algorithm accuracy

To assess the precision of the Gauss-Newton algorithm, a randomly selected data set (n=15 cells) was reassessed for alignment and compared to the original data. The precision of the algorithm's convergence was to determine the appropriate width of bins for the alignment histograms. The individual cellular degree (of alignment) values were compiled as vectors, \mathbf{v}_{old} and \mathbf{v}_{new} . Variation in degree output was determined using a scaled L1-norm, where the L1-norm was divided by the sample size (see Materials and Methods section for further details).

For the scaled norm (the average difference between the degree inputs), we found that the code was accurate to ± 3.479 degrees. This means that any binning less than ~ 7 degrees is too stringent a constraint on the algorithm (the code cannot discern between alignments within the 7-degree range). Therefore, binning on the order of ~ 10 degrees was chosen for histogram analysis.

Discussion

The neuron is the functional unit of the nervous system, which is responsible for the conduction of electrical signals throughout the body. The peripheral nervous system, the body's nervous tissues excluding the brain and spinal cord, is responsible for sensory input and motor output into and from the central nervous system, respectively. When peripheral nerves are damaged, signals to and from the central nervous system are interrupted, and functions such as sensation and motor activity are limited. The most extreme case of peripheral nerve injury is that of nerve transection, where the nervous tissue is physically separated. Without surgical intervention, this physical insult leads to loss of function of the nerve. Thus, the field of peripheral nerve regeneration seeks to physically and functionally reconnect the two ends of the severed nerve cable.

Nerve regeneration is a complex process that requires the presence of numerous factors, signaling cues, and design parameters to be successful. The most effective way to incorporate all of these factors to treat peripheral nerve damage has been to develop a nerve guidance conduit (NGC). A useful nerve guide or conduit should contain some key design parameters: anisotropy to allow for directional outgrowth of the axons, controlled release/delivery of growth factors in tandem/adhesive molecules such as laminin and fibronectin, biocompatibility, biodegradability to complement the nerve regeneration rate, and conduit porosity to allow sufficient nutrient infusion while limiting fibrous tissue infiltration. Additionally, the importance of scaffold selection cannot be ignored. Biopolymers and synthetic materials may both contribute to the development of more successful solutions than nerve autografts, though they each have limitations. While biopolymers offer the highest degree of biocompatibility and cellular affinity, synthetic materials often offer a higher degree of modifications. The goal of peripheral nerve repair is to promote the robust regenerative response of the proximal nerve cable, so that it may eventually grow through its distal end, and recover functionality through synapsing with its original output. Though there exist many bioengineering strategies currently in use to address these challenges, there remains no biomaterial solution today than has been shown to outperform the autologous nerve graft; though, there are many strategies that are encouraging.

To date, complete functional recovery of peripheral nerves after damage is infrequent. Long gaps between nerve ends limit the potential for regeneration due to poor nerve re-growth, which proceeds at a rate of ~1 mm per day (S. Walsh and R. Midha, 2009). Exposure of neurons to specific adhesive proteins and growth factors has been shown to favorably impact cell growth and survival (Evercooren *et al.*, 1982). In the present work, we were interested in augmenting cellular adhesion of P19 neurons onto flat silk films. Silk is a versatile biomaterial, which is easily chemically modified and doped with different growth factors. Specifically, drug release effects of nerve growth factor (NGF) on the differentiation of the PC-12 cell line have been well-characterized (Uebersax *et al.*, 2007), as well as the alterations of surface chemistry with adhesive peptide RGD (Sofia *et al.*, 2001). In the current studies, cellular adhesion and proliferation of P19 neurons in response to adhesive protein laminin and neurotrophic factor NGF were

studied. Optimized responses to systemic delivery of nerve growth factor was found at a concentration of 50 ng/ml, while the most positive effects were observed with laminin protein at a concentration of 5 μ g/ml.

In addition to protein cues, topographical cues are able to influence neurite outgrowth via contact guidance, leading to axonal alignment on patterns on the micro- and nano- scales (Li and Hoffman-Kim, 2008). More recently, it has been shown that cellular alignment *in vivo* can promote a robust regenerative response that is not observed on isotropic surfaces (Kim *et al.*, 2008; Clements *et al.*, 2009). Alignment of nerve fascicles is an integral part of nerve regeneration. Indeed, the majority of microsurgical and tissue engineering approaches to nerve repair seek to re-align the ends of regenerating fibers (Evans, 2001). The current research screened micropatterned silk film arrays, and found that cellular alignment was both a function of pitch angle and pattern width. Optimized results were obtained using films with 300 grates per mm and a 17° pitch angle. We were able to achieve cellular alignment on the order of ~70%, making micropatterned silk films a well-suited biomaterial scaffold for *in vivo* nerve regeneration applications.

In spite of the existence of numerous technologies developed to align cell on biomaterial platforms, there are no satisfactory automated algorithms available for the objective assessment of neuronal alignment. Despite the need for a more objective assessment of cellular orientation, the most common assessment of cellular orientation uses statistical tests, which generate analyses based on hand-made, subjective measurements of neurite/soma position and orientation (Li and Hoffman-Kim, 2008). More recent work has attempted to develop semi-automated algorithms to model cellular and subcellular structures as ellipses.

One approach to this problem has been a direct ellipse-specific fitting of data points (Fitzgibbon *et al.*, 1999). This technique seeks to model data as a quadratic polynomial and fit the data directly based on a linear least squares approach. It also allows for low noise sensitivity and relatively low computational cost. Thus, this technique has been used by numerous groups for analyses such as modeling the deformation of cardiomyocyte nuclei in response to cardiac tissue dynamics (Bray *et al.*, 2010), and approximating the arborization of dorsal root ganglia (DRG) neurites in responses to varying concentration gradients of nerve growth factor (NGF) (Haines and Goodhill, 2010). The current project's goal was to develop an algorithm modeling a maturing PC-12 neuron as an ellipse, and then extract cellular orientation data from the algorithm's convergence on a solution. This problem required a different approach than the available techniques. The convergence of an ellipse on the discretized image of a cell requires solving a nonlinear least squares problem. For this, a low-cost Gauss-Newton algorithm was used to extract elliptical parameters.

The algorithm used to obtain relative cellular alignment on a silk film was completely automated. While Bray uses complex filtering methods to rid images of noise, and Haines and Goodhill require manual image manipulation for proper implementation of the ellipse-specific fitting algorithm, no user input beyond two initial images, a transmission image of the micropatterned silk film and a fluorescent image of the cell, is required.

Additionally, this algorithm is less sensitive to noise based on two image thresholding processes built into the algorithm, which can cancel out noise by a) subtracting image content below the mean scaled pixel values (automated), and b) carefully selecting a “starting guess” ellipse (at the cost of complete automation), if desirable. Through our results, we have also shown that the current algorithm can accurately assess cellular alignment through an elliptical approximation, on the order of $\pm 3.5^\circ$.

Additionally, our algorithm has the option of extrapolating axis parameters (major and minor) and centroid location, which allow for the determination of cellular eccentricity, and relative location of the ellipse in the image, respectively. Similar to previous work, the current algorithm could be applied to determine nuclear deformation or repositioning in anisotropically distributed tissues (Bray *et al.*, 2010). This technique can also be broadly applied, across cell types with polarized (elliptical) morphologies. To offer a brief list, this technique may be able to assess the alignment of cell types such as fibroblasts, myocytes, and endothelial cells (Karlson *et al.*, 1999).

A more powerful implementation of this algorithm may be for prediction of *in vivo* success of anisotropic biomaterials. Alignment of neural cell types is intrinsically related to nerve cell function—tracking of the growth cone along the proper axis of alignment leads to the appropriate formation of functional synapses. Thus, if one could tie degree of *in vitro* alignment to *in vivo* regeneration, using the statistical tests currently applied, a model could be developed, yielding predictions of *in vivo* regenerative success prior to nerve conduit implantation. This may lead to the establishment of standards for cellular alignment prior to implantation.

Future Directions

Optimizing Neurotrophic Factor Combinations for Nerve Repair

The role of controlled drug release in neural repair applications is to match the release kinetics to that of the regenerating nerve. Since the current work has demonstrated multiple mechanisms of drug delivery with varying release kinetics, the next step would further investigate neurotrophic factor synergy *in vitro* and *in vivo*. The current studies focused on the controlled release and post-release bioactivity of glial cell line-derived neurotrophic factor (GDNF), which is one of many growth factors essential for successful peripheral nerve regeneration (for further details, see Table 3b in the Background section). Other growth factors such as nerve growth factor (NGF), NT-3, and NT-4/5 also play important roles in neural repair.

Synergistic effects between growth factors such as GDNF, NGF, and CNTF have been heavily characterized (Deister and Schmidt, 2006); however, there exists much less data in the literature concerning the effect of time-dependent release of neurotrophic factors on peripheral nerve regeneration. Future studies would emphasize the importance of the role of sustained release kinetics and time delays, which would be able to more appropriately match the growth and guidance demands of the regenerating axons through critically-sized nerve defects.

In cases of peripheral nerve injury, surgical intervention is not always immediate, which can lead to chronic axotomy of the damaged nerve. To overcome this barrier, continuous delivery of exogenous growth factors becomes necessary. A recent study found that sustained release of the neurotrophic factors BDNF and GDNF played an essential role in governing the regeneration process (Gordon, 2009). While 7 days of continuous growth factor infusion reversed the effects of delayed treatment, it was only after 30 days of continuous infusion that significant differences in regeneration were observed. This study argues for the necessity of sustained release systems for controlled drug release in peripheral nerve repair applications.

Using the silk drug delivery system described earlier, continuous release of GDNF (and other growth factors) over a 30-day period may be possible. Additionally, other silk technologies such as lyophilized hydrogels have demonstrated sustained release of up to 38 days, with kinetics simply altered based on silk protein concentration (Guziewicz *et al.*, 2011). In combination, these technologies may be further developed to obtain tailored release properties for specific peripheral nerve injuries.

Automated Image Processing of Aligned Neurons

The ultimate goal in nerve image processing is automation in the assessment of nerve cell alignment. The current algorithm described is completely automated. This work can be extended further to accommodate other published aspects of image processing. The identification and selection of individual cells and cell populations based on cell eccentricity and clustering, respectively, would simplify the process through which neuronal cells are determined. Additionally, this would effectively eliminate the need for

manual selection of cells on which to perform data analyses, making this process completely objective and image input-dependent. Further, in studies concerned with developmental neurobiology, morphological changes in cellular structures could be tracked using a modified version of this algorithm, similar to what studies on changes in nuclear morphology were able to accomplish.

PC-12 Excitability on Patterned Silk Scaffolds

While we were able to physically align the neurons on micropatterned silk scaffolds, there still remains the question of cell functionality. While these cells are viable, it is uncertain whether or not these scaffolds are capable of supporting electrical excitability of the neurons. Studies currently underway are investigating this question through actively perturbing calcium dynamics, using fluorometric dyes coupled with time-lapse confocal microscopy with temporal resolution on the order of seconds. Cellular responses to nerve-specific agonists will be able to determine if cells are electrically excitable on the micropatterned silk films. Another possible direction of this project is to use electrophysiological methods, such as patch clamping, to understand the electrical properties of neurons on the films. This technique is more technically challenging, though it offers a much more accurate picture of cellular dynamics and temporal resolution orders of magnitude greater.

***In Vivo* Studies for Evaluating Silk Nerve Guidance Conduits**

The goal of this research was to further develop silk technologies for peripheral nerve repair and to eventually translate these developments into clinical devices, such as the nerve guidance conduit. Thin-films within nerve guidance conduits have already proven to be a highly successful technique, *in vivo*, helping bridging critically-sized defects in rat models (Kim *et al.*, 2008; Clements *et al.*, 2009). These same technologies may be further developed for combination with silk tube *in vivo* studies currently being conducted in collaboration with groups at the University of Pittsburgh and Wake Forest University.

Conclusions

The current research has demonstrated a novel method for the alignment and automated assessment of alignment for neuronally differentiated cell lines. Micropatterned silk fibroin film arrays were generated using a simple PDMS-negative silk casting technique and assessed for use in aligning neuronal cultures, derived from the P19 cell line. Results from these studies indicate that micropattern width and pitch angle are important design parameters for obtaining optimal nerve cell alignment. Once these films were assessed for efficacy, the top-performing film was used to align and analyze the alignment of the PC-12 cell line. The analysis of the PC-12 cellular alignment led to the development of a fully automated algorithm, which could assess both absolute cellular orientation and the angle range of alignment.

These techniques provide tools for obtaining neuron alignment and monitoring morphological changes in response to micropatterned environments. These tools will hopefully lead to automated *in vitro* screens, which can assess the efficacy of micropatterned scaffolds in aligning neurons. In the future, it may also be beneficial to use cellular auto-fluorescence to track cells over time, to observe the alignment process and synaptogenesis.

The above research is a small step in understanding the nerve alignment and regeneration process. The presented methods will hopefully be developed further to both better understand the neuron alignment process and develop anisotropic scaffolds, which yield optimized cellular alignment for eventual applications *in vivo*.

Appendix

Nerve Cell Alignment Algorithms

Manual Nerve Cell Alignment Code

```
%CELL_PROGRAM.m
```

```
%%%% Calculate the angle between two vectors as defined by three points; also
calculate the length of the second vector JML, AN
```

```
clear all
```

```
%(atan((y2-y1)/(x2-x1)) - atan((y4-y3)/(x4-x3))) *180/pi;
```

```
[filename, pathname]=uigetfile('*.tif','Choose Files','MultiSelect','on');
num_files=length(filename);
namestring= [char pathname char filename];
image=imread(namestring);
figure, imshow(image);
hold on;
```

```
%get point
data=double(image);
data=rgb2gray(data);
```

```
data=ginput;
```

```
total=length(data);
```

```
index=1;
```

```
counter=1;
```

```
while index< total
```

```
%inputs
x1=data(index,1);
y1=data(index,2);
```

```
x2=data(index+1,1);
y2=data(index+1,2);
```

```

x3=x2;
y3=y2;

x4=data(index+2,1);
y4=data(index+2,2);

% output stores 1-angle, 2-length, 3-x1, 4-y1, 5-x2, 6-y2, 7-y4, 8-y4

output(counter,1)=(atan((y2-y1)/(x2-x1)) - atan((y4-y3)/(x4-x3))) *180/pi;

output(counter,2)=sqrt((x4-x3)^2 + (y4-y3)^2);

output(counter,3)=x1;
output(counter,4)=y1;
output(counter,5)=x2;
output(counter,6)=y2;
output(counter,7)=x4;
output(counter,8)=y4;

index=index+3;

counter=counter+1;

end

%angle
output

```

Starting Image Guess

```

%makeimageNew.m

function [Z]=makeimage(p,N)

%N=size(p,1);

hstep=1/(N-1);

sigma1=p(3); sigma2=p(4);
h=p(1); k=p(2);
theta=p(5);

[X,Y]=meshgrid(0:hstep:1,0:hstep:1); Y=flipud(Y);

```

```
zed=(1/sigma1^2)*(((X-h)*cos(theta))+((Y-k)*sin(theta))).^2+(1/sigma2^2)*((-X-h)*sin(theta))+((Y-k)*cos(theta)).^2;
```

```
Z=zeros(size(X));
f=find(zed<=1); Z(f)=1;
```

Gauss-Newton Algorithm

```
%gnv3J.m
```

```
function [im,x]=gnv3J(x0,trueim,maxstep,tol,tol2,N)
[r,J,F,im]=myfunction(x0,trueim,N);
```

```
x=x0;
F=10000;
```

```
for i=1:maxstep
    s=J\(-r);
    xold=x;
    x = x + s;
    [i,norm(x-xold)/norm(xold),F]

    if (norm(x-xold)/norm(xold)<tol)
        break
    return
end
```

```
if F<tol2
    break
end
```

```
end
```

```
[r,J,F,im]=myfunction(x,trueim,N);
```

```
end
end
```

```
function [r,J,F,guess]=myfunction(y,trueim,N)
guess=makeimageNew(y,N);
```

```
r=guess(:)-trueim(:);
```

```
%Epsilons are deltas from Materials and Methods Section, used to determine parameter spacing
```

```

epsilon1=.001; epsilon2=.001;
epsilon3=.001; epsilon4=.001;
epsilon5=pi/16;

%Input entries for Jacobian matrix
newy=y; newy(1)=y(1)+epsilon1;
newZ=makeimageNew(newy,N); newy(1)=y(1)-epsilon1;
newZ2=makeimageNew(newy,N);
J(:,1)=.5*(1/epsilon1)*(newZ(:) - newZ2(:));

newy=y; newy(2)=y(2)+epsilon2;
newZ=makeimageNew(newy,N); newy(2)=y(2)-epsilon2;
newZ2=makeimageNew(newy,N);
J(:,2)=.5*(1/epsilon2)*(newZ(:)- newZ2(:));

newy=y; newy(3)=y(3)+epsilon3;
newZ=makeimageNew(newy,N); newy(3)=y(3)-epsilon3;
newZ2=makeimageNew(newy,N);
J(:,3)=.5*(1/epsilon3)*(newZ(:)-newZ2(:));

newy=y; newy(4)=y(4)+epsilon4;
newZ=makeimageNew(newy,N); newy(4)=y(4)-epsilon4;
newZ2=makeimageNew(newy,N);
J(:,4)=.5*(1/epsilon4)*(newZ(:)-newZ2(:));

newy=y; newy(5)=y(5)+epsilon5;
newZ=makeimageNew(newy,N); newy(5)=y(5)-epsilon5;
newZ2=makeimageNew(newy,N);
J(:,5)=.5*(1/epsilon5)*(newZ(:)-newZ2(:));

F=.5*r'*r;

end

```

Cellular Alignment Algorithm with User Display

```

%test2.m

I1=imread('Image1b.png', 'png');
X=rgb2gray(I1);
X=double(X); figure(1); imagesc(X); colorbar

[N,M]=size(X);

if (N~=M)
    disp('warning, input image not square.')

```

```

    return
end;

%Instructions for Gauss-Newton algorithm. Choose starting ellipse and iterate.
figure(1);
disp('Click your estimate of the centroid. Then click estimate of the distance of long side
from centroid. Then click estimate of distance of short side from center')

[x,y]=ginput(3);

h=1/(N-1);
xv=x*h;
yv=(N-y)*h;

sig1=sqrt((xv(1)-xv(2))^2 + (yv(1)-yv(2))^2);
sig2=sqrt((xv(1)-xv(3))^2 + (yv(1)-yv(3))^2);

theta=atan((yv(2)-yv(1))/(xv(2)-xv(1)));

p=[xv(1);yv(1);sig1;sig2;theta];

startim=makeimageNew(p,N);

pv=[xv(1);yv(1);sig1+2*h;sig2+2*h;theta];

maskim=makeimageNew(pv,N);
Y=maskim.*X; f=find(Y); med=mean(Y(f));
f=find(Y>=med);
Y=zeros(size(X)); Y(f)=1;

%Plot scaled image of cell
figure(2); imagesc(Y);

%Plot discretized image with starting ellipse guess.
figure(3); subplot(1,2,1); imagesc(startim+3*Y); title('Starting image')

maxstep=300; tolrel=1e-4; tolF=10; x=p;
nans='y';

while strcmp(nans,'y')

[im,x]=gnv3J(x,Y,maxstep,tolrel,tolF,N);

%Add convergent ellipse image
figure(3); subplot(1,2,2); imagesc(im+3*Y); title('Ending image')

```

```

nans = input('Run longer? y/n','s');

end;

%Angle output after convergence of the Gauss-Newton algorithm
theta_new=x(5)*180/pi

figure(1); [x,y]=ginput(1);

hold on

plot(x,y,'k','*', 'linewidth',3)

[x2,y2]=ginput(1);
x=x*h; y=(N-y)*h;
x2=x2*h; y2=(N-y2)*h;

```

Scaffold Alignment Code

```

%silk_align.m

%Selection of 'line' for obtaining scaffold angle of alignment
figure(1);
[xx,yy]=ginput(2); %click the upper left, then lower right, diagonals of the box.

xx=round(xx); yy=round(yy);

T=X(yy(1):yy(2),xx(1):xx(2));

figure; imagesc(T); colorbar;

m=median(T(:));

f1=find(T>m); f2=find(T<=m);
T(f1)=1; T(f2)=0;

not_happy=1;

while not_happy
figure; imagesc(T); colorbar;
hold on; [xx,yy]=ginput(1); plot(xx,yy,'k*', 'linewidth',4); %marks one end of the line.
[xx2,yy2]=ginput(1);

plot([xx,xx2],[yy,yy2],'k*--', 'linewidth',4);

```

```
figure(gcf)
not_happy = input('Repeat line selection? Enter 1 for Yes and 0 for no. ');
end;
```

```
theta_align=atan((yy-yy2)/(xx-xx2));
theta_align=abs(theta_align)*180/pi
```

Automated Scaffold Alignment Code

k-means clustering code

```
%kmeans.m
```

%k-means code uses k-means clustering to segment the scaffold image into different “means” around which the pixels are clustered. The pixel cluster with the most apparent ‘lines’ was selected for use in image analysis.

```
function [mu,mask]=kmeans(ima,k)
```

```
%%%%%%%%%%%%%%%%%%%%%%%%%%%%%%%%%%%%%%%%%%%%%%%%%%%%%%%%%%
%%%%%%%%%%%%%%%%%%%%%%%%%%%%%%%%%%%%%%%%%%%%%%%%%%%%%%%%%%
```

```
% kmeans image segmentation
```

```
% Input:
```

```
% ima: grey color image
```

```
% k: Number of classes
```

```
% Output:
```

```
% mu: vector of class means
```

```
% mask: clasification image mask
```

```
% Author: Jose Vicente Manjon Herrera
```

```
% Email: jmanjon@fis.upv.es
```

```
% Date: 27-08-2005
```

```
%%%%%%%%%%%%%%%%%%%%%%%%%%%%%%%%%%%%%%%%%%%%%%%%%%%%%%%%%%
%%%%%%%%%%%%%%%%%%%%%%%%%%%%%%%%%%%%%%%%%%%%%%%%%%%%%%%%%%
```

```
% check image
```

```
ima=double(ima);
```

```
copy=ima;    % make a copy
ima=ima(:);  % vectorize ima
mi=min(ima); % deal with negative
ima=ima-mi+1; % and zero values

s=length(ima);

% create image histogram
m=max(ima)+1;

h=zeros(1,m);

hc=zeros(1,m);

for i=1:s

    if(ima(i)>0) h(ima(i))=h(ima(i))+1;end;

end

ind=find(h);

hl=length(ind);

% initiate centroids
mu=(1:k)*m/(k+1);

% start process

while(true)

    oldmu=mu;

    % current classification

    for i=1:hl

        c=abs(ind(i)-mu);

        cc=find(c==min(c));

        hc(ind(i))=cc(1);
```

```
end

%recalculation of means

for i=1:k,
    a=find(hc==i);
    mu(i)=sum(a.*h(a))/sum(h(a));
end

if(mu==oldmu) break;end;

end

% calculate mask

s=size(copy);
mask=zeros(s);

for i=1:s(1),
    for j=1:s(2),
        c=abs(copy(i,j)-mu);
        a=find(c==min(c));
        mask(i,j)=a(1);
    end
end

end

mu=mu+mi-1; % recover real range
```

Scaffold Alignment Code
%scaff2.m

```

X = imread('PicturerGr.png');

figure; imagesc(X); axis('square')

X=X(2:end-1,2:end-1,:); %for some reason, this image has a row and column of zeros,
so get rid of them.

[m1,m2]=kmeans(X,10); %calls the kmeans algorithm w/ 6 classes.

tmp=rgb2gray(m2); %convert the result to grayscale.

tmp=(tmp==min(tmp(:))); %threshold to get the valleys only.

figure; imagesc(tmp); axis('square') %display it.

[h,w]=size(tmp);

I=eye(h,h); %identity of same size as binary image

F=tmp&I; %the and does a logical and, so creates an image of zeros and 1's

figure; spy(F(1:70,1:70)); axis('square') %do a sparsity plot of just the first 70x70

f=diag(F); %take out the diagonal from the intersection image. It has just 0's and
1's

ind=find(f); %figure out the indicies where there are 1's.

d=diff(ind); %compute the spacing between where there are interesection points. Big
values of d mean lots of space between

%valleys

mi=find(d>=median(d)); %compute the median value of the spacings. Some valley's
don't get picked up by this approach.

r=floor(median(d)/2);

idx=mi(2); check=d(idx-1)>=median(d); knt=3; len=length(mi);

while (~check)&&(knt<=len)

idx=mi(knt);

```

```

check=d(idx-1)>=median(d); knt=knt+1;
end

myim=tmp(ind(idx)-r:ind(idx)+r,ind(idx)-r:ind(idx)+r);

figure; imagesc(myim); axis('square')

%now fit a line to the data points. The image is square, so we can think
%of the lower left as 0,0.

[nx,ny]=size(myim)
h=1/(nx-1);

knt=1;
for i=1:nx
    for j=1:ny
        if myim(i,j)==1 %then record that as a data point.
            b(knt,1)=h*(nx-i);
            A(knt,2)=h*j; A(knt,1)=1; knt=knt+1;
        end
    end
end

v=A\b; %the slope is the 2nd entry in the vector; the first entry in v is the y-intercept.
x=[0:h:1]; y=v(1)+v(2)*x; figure; plot(x,y); axis([0,1,0,1]); axis('square')

%angle with the x-axis, in degrees.

theta=acos(v(2))*180/pi

```

Materials Processing

Preparation of porous silk nerve guides

Porous silk tubes were prepared according to previously described protocols, with slight modifications (Lovett *et al.*, 2007). Tubes were formed by dipping stainless steel wire (1.7 mm diameter, Type 304V, Small Parts, Miami Lakes, FL) into concentrated silk fibroin (20-30% w/v) blended with 7 wt% poly(ethylene oxide) (PEO) at a ratio of 98/2 (wt%) silk fibroin/PEO. The silk fibroin/PEO blends were gently mixed with a micropipette tip before sonicating for 10 minutes. The stainless steel wires were dipped into the silk/PEO and, when evenly coated, dipped in methanol to transform the amorphous silk solution into the β -form silk fibroin conformation, characterized by anti-parallel β -sheets (Jin and Kaplan, 2003). Tubes were alternately dipped in the silk/PEO blend and methanol until the steel wire was evenly coated with a tube wall thickness of \sim 0.6 mm (3-5 times). To incorporate PLGA microspheres into the luminal side of the tube, after sonication of the 98/2 (wt%) silk/PEO blend, microspheres were added at 100 mg/ml and gently mixed with a micropipette tip. Tubes were prepared by repeating the alternate dipping process 2-3 times using the microsphere-loaded silk blend, followed by 1-2 dips in an unloaded 98/2 (wt%) silk/PEO blend. The coated wires were then left to dry overnight before being cut at each end, placed in a surfactant solution to remove the tubes from the wires, and placed in distilled water to extract the PEO from the silk/PEO tubes, leaving porous silk tubes.

Bibliography

Adams DN, Kao EYC, Hypolite CL, Distefano MD, Hu WS, Letourneau PC. Growth cones turn and migrate up an immobilized gradient of the laminin IKVAV peptide. *J. Neurobiol.* **2005**, 62, 134-147.

Apel PJ, Garrett JP, Sierpinski P, Ma J, Atala A, Smith TL, Koman LA, Van Dyke ME. Peripheral Nerve Regeneration Using a Keratin-Based Scaffold: Long-Term Functional and Histological Outcomes in a Mouse Model. *J. Hand Surg.* **2008**, 33, 1541-1547.

Battiston B, Tos P, Cushway TR, Geuna S. Nerve repair by means of vein filled with muscle grafts I. Clinical Results. *Microsurgery* **2000**, 20, 32-36.

Battiston B, Tos P, Geuna S, Giacobini-Robecchi MG, Guglielmone R. Nerve repair by means of vein filled with muscle grafts. II. Morphological Analysis of Regeneration. *Microsurgery* **2000**, 20, 37-41.

Bellamkonda RV. Peripheral nerve regeneration: An opinion on channels, scaffolds and anisotropy. *Biomaterials* **2006**, 27, 3515-3518.

Bray MAP, Adams WJ, Geisse NA, Feinberg AW, Sheehy SP, Parker KK. Nuclear morphology and deformation in engineered cardiac myocytes and tissues. *Biomaterials* **2010**, 31, 5143-5150.

Brunetti V., Maiorano G, Rizzello L, Sorce B, Sabella S, Cingolani R, Pompa PP. Neurons sense nanoscale roughness with nanometer sensitivity. *Proc. Natl. Acad. Sci. USA* **2010**, 107, 6264-6269.

Burnett MG and Zager EL. Pathophysiology of nerve injury: A brief review. *Neurosurg. Focus* **2004**, 16, 1-7.

Cao X and Shoichet MS. Defining the concentration gradient of nerve growth factor for guided neurite outgrowth. *Neuroscience* **2001**, 103, 831-840.

Cecchini M, Bumma G, Serresi M, Beltram F. PC12 differentiation on biopolymer nanostructures. *Nanotechnology* **2007**, 18, 1-7.

Chiu DTW and Strauch B. A prospective clinical evaluation of autogenous vein grafts used as a nerve conduit for distal sensory nerve defects of 3 cm or less. *Plast. Reconstr. Surg.* **1990**, 86, 928-934.

Clements IP, Kim YT, English AW, Lu X, Chung A, Bellamkonda RV. Thin-film enhanced nerve guidance channels for peripheral nerve repair. *Biomaterials* **2009**, 30, 3834-3846.

Coleman MP and Freeman MR. Wallerian degeneration, Wld^S, and Nmnat. *Annu. Rev. Neurosci.* **2010**, 33, 245-267.

Dadsetan M, Knight AM, Lu L, Windebank AJ, Yaszemski MJ. Stimulation of neurite outgrowth using positively charged hydrogels. *Biomaterials* **2009**, 30, 3874-3881.

Deister C and Schmidt CE. Optimizing neurotrophic factor combinations for neurite outgrowth. *Journal of Neural Engineering* **2006**, 3, 172-179.

Dellon AL and Mackinnon SE. An alternative to the classical nerve graft for the management of the short nerve gap. *Plast. Reconstr. Surg.* **1988**, 82, 849-856.

Ding F, Wu J, Yang Y, Hu W, Zhu Q, Tang X, Liu J, Gu X. Use of tissue-engineered nerve grafts consisting of a chitosan/poly(lactic-co-glycolic acid)-based scaffold included with bone marrow mesenchymal cells for bridging 50-mm dog sciatic nerve gaps. *Tissue Engineering: Part A* **2010**, 16, 3779-3790.

Dodd J and Jessell TM. Axon guidance and the patterning of neuronal projections in vertebrates. *Science* **1988**, 242, 692-699.

Dodla MC and Bellamkonda RV. Differences between the effect of anisotropic and isotropic laminin and nerve growth factor presenting scaffolds on nerve regeneration across long peripheral gaps. *Biomaterials* **2008**, 29, 33-46.

Fitzgibbon A, Pilu M, Fisher RB. Direct Least Square Fitting of Ellipses. *IEEE Transactions on Pattern Analysis and Machine Intelligence* **1999**, 21, 476-480.

Frandsen PE, Jonasson K, Nielsen HB, Tingleff O. Unconstrained optimization. *IMM* **2004**, 86 pages.

Gee KR, Brown KA, Chen WNU, Bishop-Stewart J, Gray D, Johnson I. Chemical and physiological characterization of fluo-4 Ca²⁺-indicator dyes. *Cell Calcium* **2000**, 27, 97-106.

Ghaznavi AM, Kokai LE, Lovett ML, Kaplan DL, Marra KG. Silk fibroin conduits: A cellular and functional assessment of peripheral nerve repair. *Ann. Plast. Surg.* **2011**, Epub ahead of print.

Gil ES Park SH, Marchant J, Omenetto F, Kaplan DL. Response of human corneal fibroblasts on silk film surface patterns. *Macromol. Biosci.* **2010**, 10, 664-673.

Glasby MA, Gschmeissner SG, Hitchcock RJ, Huang CL. The dependence of nerve regeneration through muscle grafts in the rat on the availability and orientation of basement membrane. *J. Neurocytol.* **1986**, 15, 497-510.

Gordon T. The role of neurotrophic factors in nerve regeneration. *Neurosurgery Focus* **2009**, 26, 1-10.

- Greene LA and Tischler AS. Establishment of a noradrenergic clonal line of rat adrenal pheochromocytoma cells which respond to nerve growth factor. *Proc. Natl. Acad. Sci. USA* **1976**, 73, 2424-2428.
- Gundersen RW. Response of sensory neurites and growth cones to patterned substrata of laminin and fibronectin *in vitro*. *Developmental Biology* **1987**, 121, 423-431.
- Guziewicz N, Best A, Perez-Ramirez B, Kaplan DL. Lyophilized silk fibroin hydrogels for the sustained local delivery of therapeutic monoclonal antibodies. *Biomaterials* **2011**, 32, 2642-2650.
- Haines C and Goodhill GJ. Analyzing neurite outgrowth from explants by fitting ellipses. *Journal of Neuroscience Methods* **2010**, 187, 52-58.
- Hansen PC, Kilmer ME, Kjeldsen RH. Exploiting residual information in the parameter choice for discrete ill-posed problems. *BIT Numerical Mathematics* **2006**, 46, 41-59.
- Heath MT. *Scientific Computing: An Introductory Survey*, 2nd ed.; McGraw-Hill: New York, 2002.
- Hoffman-Kim D, Mitchel JA, Bellamkonda RV. Topography, cell response and nerve regeneration. *Annu. Rev. Biomed. Eng.* **2010**, 12, 203-231.
- Ide C. Nerve regeneration through the basal lamina scaffold of the skeletal muscle. *Neuroscience Research* **1984**, 1, 379-391.
- Jiang X, Lim SH, Mao HQ, Chew SY. Current applications and future perspectives of artificial nerve conduits. *Experimental Neurology* **2010**, 223, 86-101.
- Jiao H, Yao J, Yang Y, Chen X, Lin W, Li Y, Gu X, Wang X. Chitosan/polyglycolic acid nerve grafts for axon regeneration from prolonged axotomized neurons to chronically denervated segments. *Biomaterials* **2009**, 30, 5004-5018.
- Jin HJ and Kaplan DL. Mechanism of silk processing in insects and spiders. *Nature* **2003**, 424, 1057-61.
- Johnson EO and Soucacos PO. Nerve repair: Experimental and clinical evaluation of biodegradable artificial nerve guides. *Injury* **2008**, 39S, 530-536.
- Jones-Villeneuve EMV, McBurney MW, Rogers KA, Kalnins VI. Retinoic acid induces embryonal carcinoma cells to differentiate into neurons and glial cells. *J. Cell Biology* **1982**, 94, 253-262.
- Jones-Villeneuve EMV, Rudnicki MA, Harris JF, McBurney MW. Retinoic acid-induced neural differentiation of embryonal carcinoma cells. *Molecular and Cellular Biology* **1983**, 3, 2271-2279.

Kelleher MO, Al-Abri RK, Eleuterio ML, Myles LM, Lenihan DV, Glasby MA. The use of conventional and invaginated autologous vein grafts for nerve repair by means of entubulation. *British J. Plast. Surg.* **2001**, 54, 53-57.

Kim UJ, Park J, Li C, Jin HJ, Valluzzi R, Kaplan DL. Structure and Properties of Silk Hydrogels. *Biomacromolecules* **2004**, 5, 786-792.

Kim YT, Haftel VK, Kumar S, Bellamkonda RV. The role of aligned polymer fiber-based constructs in the bridging of long peripheral nerve gaps. *Biomaterials* **2008**, 29, 3117-3127.

Kokai LE, Ghaznavi AM, Marra KG. Incorporation of double-walled microspheres into polymer nerve guides for the sustained delivery of glial cell line-derived neurotrophic factor. *Biomaterials* **2010**, 31, 2313-2322.

Kokai LE, Lin YC, Oyster NM, Marra KG. Diffusion of soluble factors through degradable polymer nerve guides: Controlling manufacturing parameters. *Acta Biomaterialia* **2009**, 5, 2540-2550.

Lee H, McKeon, RJ, Bellamkonda RV. Sustained delivery of thermostabilized chABC enhances axonal sprouting and functional recovery after spinal cord injury. *Proc. Natl. Acad. Sci. USA* **2010**, 107, 3340-3345.

Lee SK and Wolfe SW. Peripheral nerve injury and repair. *J. Am. Acad. Orthop. Surg.* **2000**, 8, 243-252.

Lawrence BD, Cronin-Golomb M, Georgakoudi I, Kaplan DL, Omenetto FG. Bioactive Silk Protein Biomaterial Systems for Optical Devices. *Biomacromolecules* **2008**, 9, 1214-1220.

Lawrence BD, Marchant JK, Pindrus MA, Omenetto FG, Kaplan DL. Silk film biomaterials for cornea tissue engineering. *Biomaterials* **2009**, 30, 1299-1308.

Li C, Vepari C, Jin HJ, Kim HJ, Kaplan DL. Electrospun silk-BMP-2 scaffolds for bone tissue engineering. *Biomaterials* **2006**, 27, 3115-24.

Li GNY and Hoffman-Kim D. Evaluation of neurite outgrowth anisotropy using a novel application of circular analysis. *Journal of Neuroscience Methods* **2008**, 174, 202-214.

Lovett M, Cannizzaro C, Daheron L, Messmer B, Vunjak-Novakovic G, Kaplan DL. Silk fibroin microtubes for blood vessel engineering. *Biomaterials* **2007**, 28, 5271-5279.

Lovett ML, Cannizzaro CM, Vunjak-Novakovic G, Kaplan DL. Gel spinning of silk tubes for tissue engineering. *Biomaterials* **2008**, 29, 4650-4657.

- Lundborg G, Gelberman RH, Longo FM, Powell HC, Varon S. *In vivo* regeneration of cut nerve encased in silicone tubes. *J. Neuropath. Exp. Neurol.* **1982**, 41, 412-422.
- Mackinnon SE and Dellon AL. Clinical nerve reconstruction with a bioabsorbable polyglycolic acid tube. *Plast. Reconstr. Surg.* **1990**, 85, 419-424.
- Mackinnon SE, Dellon AL, Hudson AR, Hunter DA. Nerve regeneration through a pseudosynovial sheath in a primate model. *Plast. Reconstr. Surg.* **1985**, 75, 833-841.
- Madduri S, Papaloizos M, Gander B. Trophically and topographically functionalized silk fibroin nerve conduits for guided peripheral nerve regeneration. *Biomaterials* **2010**, 31, 2323-2334.
- Murphy AR and Kaplan DL. Biomedical applications of chemically-modified silk fibroin. *J. Mater. Chem.* **2009**, 19, 6443-6450.
- Nakayama K, Takakuda K, Koyama Y, Itoh S, Wang W, Mukai T, Shirahama N. Enhancement of Peripheral Nerve Regeneration Using Bioabsorbable Polymer Tubes Packed With Fibrin Gel. *Artif. Org.* **2007**, 31, 500-508.
- Noble J, Munro CA, Prasad VSSV, Midha R. Analysis of upper and lower extremity peripheral nerve injuries in a population of patients with multiple injuries. *J. Trauma* **1998**, 45, 116-122.
- Numata K and Kaplan DL. Silk-based delivery systems of bioactive molecules. *Advanced Drug Delivery Reviews* **2010**, 62, 1497-1508.
- Oh SH, Kim JH, Jeon BH, Yoon JH, Seo TB, Namgung U, Lee IW, Lee JH. Peripheral nerve regeneration with an asymmetrically porous PLGA/Pluronic F127 nerve guide conduit. *Biomaterials* **2008**, 29, 1601-1609.
- Okamoto H, Hata KI, Kagami H, Okada K, Ito Y, Narita Y, Hirata H, Sekiya I, Otsuka T, Ueda M. Recovery process of sciatic nerve defect with novel bioabsorbable collagen tubes packed with collagen filaments in dogs. *J. Biomed. Mater. Res.* **2010**, 92A, 859-868.
- Pritchard EM, Szybala C, Boison D, Kaplan DL. Silk fibroin encapsulated powder reservoirs for sustained release of adenosine. *J. Controlled Release* **2010**, 144, 159-167.
- Pritchard EM, Valentin T, Boison D, Kaplan DL. Incorporation of proteinase inhibitors into silk-based delivery devices for enhanced control of degradation and drug release. *Biomaterials* **2011**, 32, 909-918.
- Purves D. *Neuroscience*, 4th ed.; Sinauer Associates: Massachusetts, 2007.

- Recknor JB, Sakaguchi DS, Mallapragada SK. Directed growth and selective differentiation of neural progenitor cells on micropatterned polymer substrates. *Biomaterials* **2006**, 27, 4098-4108.
- Risitano G, Cavallaro G, Merrino T, Coppolino S, Ruggeri F. Clinical results and thoughts on sensory nerve repair by autologous vein graft in emergency hand reconstruction. *Chirurgie de la Main* **2002**, 21, 194-197.
- Saltzman WM and Olbricht WL. Building drug delivery into tissue engineering. *Nature Reviews Drug Discovery* **2002**, 1, 177-186.
- Schlosshauer B, Dreesman L, Schaller H, Sinis N. Synthetic nerve guide implants in humans: A comprehensive study. *Neurosurgery* **2006**, 59, 740-748.
- Schmidt CE and Leach JB. Neural tissue engineering: Strategies for repair and regeneration. *Annu. Rev. Biomed. Eng.* **2003**, 5, 293-347.
- Schmidt CE, Shastri VR, Vacanti JP, Langer R. Stimulation of neurite outgrowth using an electrically conducting polymer. *Proc. Natl. Acad. Sci. USA* **1997**, 94, 8948-8953.
- Schubert D and Whitlock C. Alteration of cellular adhesion by nerve growth factor. *Proc. Natl. Acad. Sci. USA* **1977**, 74, 4055-58.
- Seckel BR. Enhancement of peripheral nerve regeneration. *Muscle & Nerve* **1990**, 13, 785-800.
- Sierpinski P, Garrett J, Ma J, Apel P, Klorig D, Smith T, Koman LA, Atala A, Van Dyke M. The use of keratin biomaterials derived from human hair for the promotion of rapid regeneration of peripheral nerves. *Biomaterials* **2008**, 29, 118-28.
- Sofia S, McCarthy MB, Gronowicz G, Kaplan DL. Functionalize silk-based biomaterials for bone formation. *J. Biomed. Mater. Res.* **2001**, 54, 139-148.
- Song HK, Toste B, Ahmann K, Hoffman-Kim D, Palmore GTR. Micropatterns of positive guidance cues anchored to polypyrrole doped with polyglutamic acid: a new platform for characterizing neurite extension in complex environments. *Biomaterials* **2006**, 27, 473-484.
- Stahl S and Goldberg JA. The use of vein grafts in upper extremity nerve surgery. *Eur. J. Plast. Surg.* **1999**, 22, 255-259.
- Stanfield CL. *Principles of Human Physiology*, 4th ed.; Pearson: Boston, 2005.
- Strauch B, Ferder M, Lovelle-Allen S, Moore K, Kim DJ, Llena J. Determining the maximal length of a vein conduit used as an interposition graft for nerve regeneration. *J. Reconstr. Microsurg.* **1996**, 12, 521-527.

Sunderland S. Rate of regeneration in human peripheral nerves. *Arch. Neurol. Psychiatry* **1947**, 58, 251-295.

Tang JB, Shi D, Zhou H. Vein conduits for repair of nerves with a prolonged gap or in unfavorable conditions: An analysis of three failed cases. *Microsurgery* **1995**, 16, 133-137.

Tannemaat MR, Korecka J, Ehlert EME, Mason MRJ, van Duinen SG, Boer GJ, Malessy MJA, Verhaagen J. Human neuroma contains increased levels of Semaphorin 3A, which surrounds nerve fibers and reduces neurite extension *in vitro*. *J. Neurosci.* **2007**, 27, 14260-14264.

Uebersax L, Mattotti M, Papaloizos M, Merkle HP, Gander B, Meinel L. Silk fibroin matrices for the controlled release of nerve growth factor (NGF). *Biomaterials* **2007**, 28, 4449-4460.

Vargas ME and Barres BA. Why is Wallerian degeneration in the CNS so slow? *Annu. Rev. Neurosci.* **2007**, 30, 153-179.

Walsh S and Midha R. Practical considerations concerning the use of stem cells for peripheral nerve repair. *Neurosurg. Focus* **2009**, 26, 1-8.

Wang HB, Mullins ME, Cregg JM, Hurtado A, Oudega M, Trombley MT, Gilbert RJ. Creation of highly aligned electrospun poly-L-lactic acid fibers for nerve regeneration applications. *J. Neural Eng.* **2009**, 6, 1-15.

Wang X, Hu W, Cao Y, Yao J, Wu J, Gu X. Dog sciatic nerve regeneration across a 30-mm defect bridged by a chitosan/PGA artificial nerve graft. *Brain* **2005**, 128, 1897-1910.

Wang X, Wenk E, Matsumoto A, Meinel L, Li C, Kaplan DL. Silk microspheres for encapsulation and controlled release. *Journal of Controlled Release* **2007**, 117, 360-370.

Wolford LM and Stevao ELL. Considerations in nerve repair. *BUMC Proceedings* **2003**, 16, 152-156.

Xie F, Li QF, Gu B, Liu K, Shen GX. In vitro and in vivo evaluation of a biodegradable chitosan-PLA composite peripheral nerve guide conduit material. *Microsurgery* **2008**, 28, 471-479.

Yang Y, Chen X, Ding F, Zhang P, Liu J, Gu X. Biocompatibility evaluation of silk fibroin with peripheral nerve tissues and cells in vitro. *Biomaterials* **2007**, 28, 1643-1652.

Yang Y, Ding F, Wu J, Hu W, Liu W, Liu J, Gu X. Development and evaluation of silk fibroin-based nerve grafts used for peripheral nerve regeneration. *Biomaterials* **2007**, 28, 5526-5535.

Yu TT, and Shoichet MS. Guided cell adhesion and outgrowth in peptide-modified channels for neural tissue engineering. *Biomaterials* **2005**, 26, 1507-1514.